UT GSBS Dissertations and Theses (Open Access)   Graduate School of Biomedical Sciences

12-2016

Determination of Thermal Dose Model Parameters Using Magnetic Resonance Imaging

Christopher James MacLellan

Follow this and additional works at: http://digitalcommons.library.tmc.edu/utgsbs_dissertations

Part of the Radiology Commons

Recommended Citation

DETERMINATION OF THERMAL DOSE MODEL PARAMETERS
USING MAGNETIC RESONANCE IMAGING
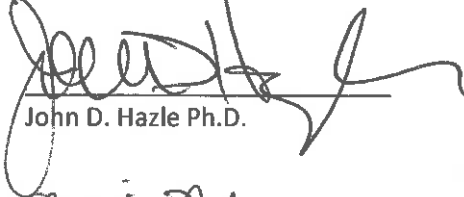
by

Christopher James MacLellan BS

APPROVED:

R. Jason Stafford, Ph.D.
Advisory Professor

James A. Bankson, Ph.D.

John D. Hazle Ph.D.

Marites Melancon **Ph.D.**

Arvind Rao Ph.D.

APPROVED:

Dean, The University of Texas
Graduate School of Biomedical Sciences at Houston

DETERMINATION OF THERMAL DOSE MODEL PARAMETERS

USING MAGNETIC RESONANCE IMAGING

A

DISSERTATION

Presented to the Faculty of
The University of Texas
Health Science Center at Houston
and
The University of Texas
MD Anderson Cancer Center
Graduate School of Biomedical Sciences
in Partial Fulfillment
of the Requirements
for the Degree of

DOCTOR OF PHILOSOPHY

by

Christopher James MacLellan, B.S.

Houston, Texas

December, 2016

Acknowledgements

First and foremost I would like to thank Jason Stafford for his guidance and patience over the past 6 years. Despite his increasing responsibilities within the department he has always taken the time to support me throughout my studies. I would also like to thank the members of my advisory committee for providing thoughtful feedback as I developed my doctoral research. In particular, I thank David Fuentes and Tess Melancon for their active role in my training over the years. I also thank Ken Hwang for his help with pulse sequence programming on the GE systems. I would also like to thank Anne Fisher and the Imaging Physics MIT team for their help working on the MRI in CABI. I'm also extremely grateful for my friends and colleagues in the Medical Physics graduate program, especially my officemates in 3SCR. Graduate school is not always easy and the support of my peers throughout the years made all the difference.

DETERMINATION OF THERMAL DOSE MODEL PARAMETERS USING MAGNETIC RESONANCE IMAGING

Christopher James MacLellan, B.S.

Advisory Professor: R. Jason Stafford Ph.D.

Magnetic Resonance Temperature Imaging (MRTI) is a powerful technique for noninvasively monitoring temperature during minimally invasive thermal therapy procedures. When coupled with thermal dose models, MRTI feedback provides the clinician with a real-time estimate of tissue damage by functioning as a surrogate for post-treatment verification imaging. This aids in maximizing the safety and efficacy of treatment by facilitating adaptive control of the damaged volume during therapy. The underlying thermal dose parameters are derived from laboratory experiments that do not necessarily reflect the surrogate imaging endpoints used for treatment verification. Thus, there is interest and opportunity in deriving model parameters from clinical procedures that are tailored to radiologic endpoints.

The objective of this work is to develop and investigate the feasibility of a methodology for extracting thermal dose model parameters from MR data acquired during ablation procedures. To this end, two approaches are investigated. One is to optimize model parameters using post-treatment imaging outcomes. Another is to use a multi-parametric pulse sequence designed for simultaneous monitoring of temperature and damage dependent MR parameters. These methodologies were developed and investigated in phantom and feasibility established using retrospective analysis of *in vivo* thermal therapy treatments. This technique represents an opportunity to exploit experimental data to obtain thermal dose parameters that are highly specific for clinically relevant endpoints.

Table of Contents

List of Figures

List of Tables

List of Abbreviations

ADC- Apparent Diffusion Coefficient

AIC- Akaike Information Criterion

ANOVA - Analysis of Variance

AR- Absolute Rate Model

ARMA- Autoregressive Moving Average

AUC- Area Under Curve

B_0- Static Magnetic Field

B_1- Applied Radio Frequency Field

CE- Contrast Enhanced

CEM- Cumulative Effective Minutes

CPD- Complex Phase Difference

CT- Critical Temperature Model

CV- Control Variable

DAM- Double Angle Method

DCE- Dynamic Contrast Enhanced

EOI- Effect of Interest

ESP- Echo Spacing

FC- Fractional Conversion

FOV- Field of View

FGRE- Fast Gradient-Recalled Echo

FETS- Fast Exchange Two State

HD- Hausdorff Distance

HIFU- Focused Ultrasound

IR- Inversion Recovery

MDA- Mean Distance to Agreement

MR- Magnetic Resonance

MRTI- Magnetic Resonance Temperature Imaging

MT- Magnetization Transfer

MTR- Magnetization Transfer Ratio

MWA- Microwave Ablation

NIfTI- Neuroimaging Informatics Technology Initiative

PRF- Proton Resonance Frequency

RBW- Receiver Bandwidth

RFA- Radiofrequency Ablation

SLR- Shinnar-LeRoux

SNR- Signal to Noise Ratio

T1- Longitudinal Relaxation Time

T1-W- T1-Weighted

T2-Transverse Relaxation Time

T2-W- T2-Weighted

TE- Echo Time

TE_{min}- Minimum Echo Time

TI- Inversion Time

US- Ultrasound

VFA- Variable Flip Angle

Chapter 1: Introduction

Minimally invasive, image-guided thermal ablation therapies are increasingly being incorporated into clinical practice as an alternative to traditional surgery. This trend is largely driven by synergy with advanced imaging modalities during treatment planning, monitoring, and assessment. In particular, real-time temperature monitoring using Magnetic Resonance Temperature Imaging (MRTI) can be a powerful tool for guiding these procedures when coupled to appropriate thermal dose models. MRTI acts as a surrogate to post-treatment imaging that provides a means for assessing procedure progress, safety, and efficacy in real-time. This is useful in that post-treatment verification imaging often takes time, or makes use of injected contrast agents, to assess the procedure efficacy.

On a fundamental level, thermal dose models predict the probability of observing an effect of interest (EOI) after a given thermal exposure. Clinically utilized thermal dose models typically assume that the onset of an EOI can be modeled as an Arrhenius process and rely almost exclusively on empirical parameters derived from laboratory experiments. This is direct consequence of the underlying Arrhenius kinetics, which generally demand that temperature be precisely monitored and controlled throughout the experiments. However, the gold standard for treatment assessment is based on radiologic EOIs that exploit irreversible changes in MR parameters. Traditionally, this encompasses post-treatment imaging of the thermal lesion using one or more contrast mechanisms, although intra-treatment changes in intrinsic MR parameters have also been associated with irreversible changes in tissue. This incongruity between the dose monitoring and assessment makes a method for extracting thermal dose model parameters directly from radiologic data of interest. Such a technique would provide predictions that are more closely aligned with clinical endpoints

and provide an opportunity to leverage ever increasing amounts of patient data for continual refinement.

Therefore, **the hypothesis of this research is that the MR imaging information acquired during thermal ablation procedures can be used to derive unique Arrhenius based thermal dose model parameters for MR observable effects of interest _in vivo_.** This hypothesis will be tested by completing the following specific aims:

Specific Aim 1: Design and validate a multi-parametric pulse sequence suitable for monitoring multiple temperature dependent MR parameters with high temporal and spatial resolution.

Arrhenius damage models are parameterized by two empirically derived constants and predict the onset of an EOI as a function of tissue temperature-time history. Deriving these constants requires monitoring tissue temperature and measuring the specified EOI. While it is possible to construct a MR-derived model of thermal dose solely using post-treatment imaging, several damage dependent intrinsic MR parameters that have been associated with irreversible damage may be able to provide complementary information when monitored simultaneously with temperature. The working hypothesis in this aim is that the abrupt changes in the linearity of the temperature dependence of relaxation rates T1 and T2* associated with irreversible tissue changes can be accurately measured during heating. In order to investigate this hypothesis, a multi-echo gradient-recalled echo pulse sequence will be modified so that flip angles can be alternated throughout the acquisition to facilitate simultaneous measurements of T1, T2*, and PRF during heating.

Specific Aim 2: Develop and characterize an experimental and computational methodology for estimating thermal dose model parameters for MR-observable EOIs and validate in phantom.

Traditionally, experiments for developing Arrhenius models of thermal dose have been restricted to the laboratory due to the transcendental nature of the governing equations and measurements. The working hypothesis in this aim is that the MR temperature information collected during thermal therapy delivery can be coupled with independent MR imaging information acquired during or after therapy to obtain Arrhenius model parameters that are predictive of the imaging EOIs. Using multi-parametric feedback (SA1), post-treatment imaging, and nonlinear regression algorithms, a technique will be developed for training Arrhenius models for intra- and post-treatment radiologic EOIs. This method will be validated to heating experiments in a protein coagulation phantom that can be well controlled and compared to literature values.

Specific Aim 3: Derive and validate MR based damage models from *in vivo* human data using the methodology outlined in SA2.

To demonstrate feasibility of deriving thermal dose model parameters from MR data, the methods developed in SA2 will be investigated in *in vivo* ablation procedures. The optimal dose model parameters will be investigated by retrospectively analyzing laser ablation (N=5) procedures in human brain and using contrast enhanced T1-weighted imaging as an EOI. These parameters will be critically compared to existing literature both in terms of values and predicted areas of damage.

The organization of the dissertation is thus. Chapter 2 begins with a broad overview of thermal therapies followed by an examination of the role of MR during treatment planning, monitoring and assessment. Chapter 3 takes an in depth look at the theoretical basis of thermal dose models and previous investigations into different models. Chapters 4, 5 and 6 address specific aims 1, 2, and 3, respectively.

Chapter 2: MR Guided Thermal Therapy

2.1 Introduction

Thermal therapies are clinical procedures where an external energy source is used to elevate the temperature of target tissue to achieve a therapeutic effect. The development of non-invasive imaging techniques has played a large role in the adoption of thermal therapies into the clinic and is critical in each of four stages common to all thermal therapy procedures: planning, targeting, monitoring, and asessment.[1] MR is particularly well suited to these tasks due to its ability to image in arbitrary planes, lack of ionizing radiation, and the ability to exploit a variety of contrast mechanisms that are uniquely suited for each stage of the procedure.

2.2 Thermal Therapies

Thermal therapies that employ heating can be broadly categorized into two general regimes: thermal ablation and hyperthermia. In the former tissue temperature is raised to relatively high temperatures for short periods to destroy tissue via acute thermal injury whereas hyperthermia uses relatively low temperatures to sensitize tissue to other treatments.

2.2.1 Thermal Ablation

Ablation procedures are characterized by high temperatures (>50 ^{0}C) maintained for short durations (seconds-minutes) where the primary goal is an immediate catastrophic and irreversible breakdown of structural proteins called coagulative necrosis.[2] These procedures have several advantages over conventional surgery and are predominantly used in the ablation of cancerous tumors. Procedures are designed to be noninvasive or minimally invasive, which better preserves surrounding tissues, and are associated with lower morbidity and complications. Consequently, much of the attractiveness of the procedures are because they are associated with shorter hospitalization times and reduced cost relative to open surgery. They also represent the only

treatment option in situations where surgery is contraindicated and are repeatable in case of recurrence.[3]

A variety of modalities exist for delivering thermal energy including radiofrequency ablation (RFA), microwave ablation (MWA), laser ablation, and high intensity focused ultrasound (HIFU).[4] The two most commonly used techniques, RFA and MWA, utilize percutaneously administered electrodes and antennas, respectively, to heat surrounding tissue using electromagnetic energy. Both methods have been used in a variety of malignancies and are commonly used in the liver, lungs, bone and kidneys.[3,5,6] MWA is associated with faster heating and larger ablation zone and is used for larger tumors (5-8cm) whereas RFA is used for smaller tumors (<3cm).[3,5] Despite the theoretical advantages provided by MWA, RFA remains in widespread clinical use because it is a more mature and established technology with greater familiarity among physicians. Generally, image guidance is provided by computed tomography or ultrasound for probe placement and the ablation zone is identified using post treatment imaging, usually via administration of exogenous contrast agent to assess the region of perfusion deficit.[7] Temperature is typically not monitored during these procedures using computed tomography or MRI due to dose considerations and electromagnetic interference, respectively.

Laser ablation is a third method for thermal ablation that uses a percutaneously administered laser fiber to ablate surrounding tissue. These procedures are less common than both RFA and MWA, mostly due to a reduced effective ablation zone (1-2cm).[2] One inherent advantage is that the laser does not interfere with MRI signal acquisition allowing temperature to be monitored in real-time using magnetic resonance temperature imaging (MRTI) techniques. The ability to monitor in real-time coupled with the relatively small ablation zone make laser ablation a precision technique that can maximize normal tissue sparing and be used in close proximity to critical

structures. For this reason laser ablation has been utilized in additional anatomic sites such as the brain, spine, prostate, and head and neck.[8–12]

A fourth clinically used method for thermal ablation is high-intensity focused ultrasound (HIFU). HIFU is a noninvasive procedure where an array of ultrasound transducers is focused onto a point of interest to raise the tissue to ablative temperatures. Each individual sonication achieves coagulative necrosis in a matter of seconds over a limited area (≈0.5cm) and many of these sonications are performed to cover an entire target area. HIFU is unique in that it typically relies on MRTI to confirm proper delivery of thermal energy. HIFU is one of the oldest methods of thermal ablation and has been investigated in a variety of sites[13] including breast, prostate, uterus[14], liver, and bone[15]. Traditionally, this procedure has been limited by high attenuation in bone but recent technological advances have led to specialized devices for transcranial ablation. [16–18]

In each of these procedures the primary method for evaluating the extent of thermal damage is diagnostic imaging. This often includes injection of exogenous contrast agents to evaluate perfusion in tissue. MR is particularly well suited for these types of evaluations as many contrast-mechanisms are available to evaluate different physiological effects. (section 2.6.3)

2.2.2 Hyperthermia

The second temperature regime for thermal therapies is hyperthermia which is characterized by moderate loco regional temperature (39-45^{0}C) increases in tissue temperature over long time scales (10^1-10^2 minutes). Unlike ablation, the primary goal of hyperthermia is to sensitize malignant tissue to another treatment modality such as radiation therapy, chemotherapy, or immunotherapy.[19] As such, hyperthermia is typically considered for oncologic applications. While hyperthermia has been the subject of research since the 1970s, it has experienced resurgence over the last decade due to advances in delivery and monitoring mechanisms and greater understanding of the underlying physiologic processes. Various techniques have been used to bring all or part of

the body to hyperthermic temperatures including conduction, electromagnetic energy and focused

ultrasound.

2.3 MR for Thermal Therapy Planning

Thermal therapy planning encompasses the identification of the therapeutic target and the

guidance of the external energy source to that target. Several contrast mechanisms can be exploited

to identify a target and the surrounding critical structures by adjusting MR sequence parameters.

Basic T1-weighted and T2-weighted pulse sequences often provide sufficient contrast but

exogenous T1 contrast agents may be administered to delineate tumor margins in some oncologic

cases.

2.4 MR for Thermal Therapy Targeting

Once the target is identified, additional imaging is used to direct the external energy source

to the target. Real-time anatomic imaging is used to guide the probe to the target for percutaneous

ablation techniques. Computed tomography and ultrasound (US) are the most commonly used for

this purpose, particularly in body procedures. MR plays a larger role in cases with small and/or

difficult to identify tumors or in in sensitive areas such as the prostate, brain, head, and neck that

require MRTI monitoring.[9,20] FUS procedures are unique in that they require MR or US to confirm

good acoustic coupling between the patient and the ultrasound transducers before treatment. [2122]

2.5 MR for Thermal Therapy Monitoring

MR is unique in that it is capable of noninvasively monitoring temperature during thermal

therapy procedures. This can be a critical component to ensuring the safety and efficacy of the

procedure, particularly when performed in close proximity to critical structures. CT is also

theoretically capable of monitoring temperature but requires repeated acquisitions at an increased

radiation dose.[23,24] However, due to the repeated RF pulses needed to acquire MR images, MRTI

techniques are restricted to laser and HIFU procedures unless special triggering equipment, filtering, and/or processing are used.[25] Just as in anatomic imaging, there are multiple contrast mechanisms that can be used to acquire MRTI data.

2.5.1 Proton Resonance Frequency

The most commonly used contrast mechanism for MRTI procedures is the proton resonance frequency (PRF). The complex MRI signal for a spoiled gradient echo acquisition at a fixed flip angle is given by:

$$S = S_0 e^{-TE\left(\frac{1}{T2^*} - 2\pi i \Delta f\right)} = S_0 e^{-\frac{TE}{T2^*}} e^{i\varphi} \qquad \text{2-1}$$

Where S is the complex valued signal, TE is the echo time, S_0 is the signal magnitude at TE=0 ms, T2* is the transverse relaxation time, Δf is the resonance frequency in the rotating frame of reference, and φ is the signal phase. The dependence of the proton resonance frequency of water protons with temperature has been shown to be linear and is given by:

$$\Delta T = \beta \Delta f \qquad \text{2-2}$$

Where β is the temperature sensitivity coefficient with a value of approximately -0.01 ppm/^{0}C.[26,27] The primary advantages of using the PRF shift for MRTI are that the temperature dependence is linear and largely tissue independent (with the notable exception of adipose tissue). The most common challenges result from sensitivity to other effects that can alter the resonance frequency. B_0 shifts caused by motion present a significant challenge and several techniques have been developed to address this in clinical scenarios.[28–30] Field drift caused by heating in gradient coils over long acquisition times contributes a bias to temperature measurements and can be corrected by subtracting the temperature increase in reference region provided the phase drift is sufficiently uniform across the image. Like many other MRTI techniques, the PRF technique can only give relative changes in temperature so a baseline must be measured or assumed.

There are two primary approaches for measuring temperature using changes in the PRF. The first and most common is the complex phase difference (CPD) method where a single gradient echo is acquired at each time point and the temperature is calculated from the difference between successive phase images via:

$$\Delta T = \frac{\tan^{-1}(S * S^*)}{\beta \gamma B_0 TE} \qquad \text{2-3}$$

where the phase difference is explicitly calculated in complex space to avoid phase wrapping errors.

The CPD method can be implemented on fast gradient echo or echo planar imaging sequences to maximize coverage in the slice direction and/or temporal resolution. SNR can be optimized by choosing TE=T2*, which balances the increased in phase difference with the simultaneous loss of signal magnitude as TE is increased. The primary drawbacks are that it relies on a single measurement to calculate the resonance frequency and there is an implicit assumption that the water is the only chemical species in each voxel. Additional chemical species in the voxel(s) will corrupt the measurements if the signal is not suppressed. For this reason, traditional fat/water separation techniques such IR-preparation, fat saturation, and Dixon, may be needed to obtain reliable results from PRF.[31]

Another approach to using the PRF shift to measure temperature is to perform chemical shift imaging techniques to directly measure the PRF.[32–34] Practically, this requires measuring multiple echo times at each time point at the cost of spatial and/or temporal resolution. If it can be safely assumed that water is the only chemical species present in the voxel the resonance frequency can be found by linear regression that is theoretically more precise than the single point measurement in the CPD method and also more likely to encompass the optimal echo time. Alternatively, spectral methods can be used to separate chemical species on a voxel basis and the

water resonance frequency can be extracted for purposes of temperature calculation. Using this technique, signal from multiple chemical species can be detected and the non-temperature sensitive lipid signal can theoretically be used as an internal frequency reference and/or to calculate absolute temperature. [35]

2.5.2 Longitudinal Relaxation Time (T1)

A second MR parameter that has been shown to be temperature dependent is the longitudinal relaxation time, T1. During T1 relaxation spins in an excited state return to thermal equilibrium after exchanging energy with the surrounding molecular lattice. In physiological samples, this phenomena is primarily caused by intermolecular rotational motion of water molecules creating a time varying magnetic field at the resonance frequency, ω,. This contribution to relaxation can be written:

$$\frac{1}{T_1} = k \left[\frac{2\tau_c}{1 + \omega^2\tau_c^2} + \frac{8\tau_c}{1 + 4\omega^2\tau_c^2} \right]$$
2-4

Where τ_c is the correlation time (the average time it takes for the molecule to rotate one radian), and C is a constant. The rotational speed of the water molecules is governed by the Boltzmann distribution so the temperature dependence of the τ_c can be written:

$$\tau_c = \tau_0 e^{E_c/kT}$$
2-5

Where k is the Boltzmann constant, T is the temperature (°K), τ_0 is the correlation time at $T = \infty$, and E_c is the activation energy of the rotation process. Correlation times are on the order of 10^{-12}s in pure water which allows the frequency dependent dispersion terms to be neglected $(i.e. \omega^2\tau_c^2 \ll 1)$ and the following approximation for the temperature dependence of T1:

$$T_1 \propto e^{-E_{eff}/kT}$$
2-6

Which implies that T1 has an approximately inverse relationship with temperature if the 1st order terms of the Taylor series expansion are used. [36,37]

$$T_1 \propto 1/T \qquad\qquad 2\text{-}7$$

The above derivation explicitly assumes that the signal comes from pure water with extremely short correlation times. In tissue, the presence of large macromolecules causes the surrounding water molecules to form a hydration layer where motion is restricted and correlation times are decreased. It is generally accepted that these different hydrogens populations undergo fast exchange with one another and that the observed T1 is a weighted average of these different populations. [36]

$$\frac{1}{T_1} = \sum_{i=1}^{N} f_i \frac{1}{T_{1i}}(\tau_i) \qquad\qquad 2\text{-}8$$

Where f_i is the fraction of hydrogens contained within each population, or more generally for a continuous distribution of correlation times $g(\tau_c)$:[37]

$$\frac{1}{T_1} = \int_0^\infty g(\tau)\frac{1}{T_1}(\tau)d\tau' \qquad\qquad 2\text{-}9$$

Fung and colleagues[38–40] showed that the temperature dependence of the hydration layers water can be accurately modeled by assuming that the correlation times follow a log-normal distribution and numerically solving equation 2-4. Their results suggests that temperature dependence of these hydration layer waters is negligible and equation 2-7 remains a reasonable appproximation.[41]

While an inverse relationship between T1 and T is expected from equation 2-7 it has been shown to be effectively linear over the relatively small range in absolute temperatures required for physiological samples. [42] This linear relationship is attractive for temperature monitoring and has been measured in the range of 1-2% in tissue. However, there are several drawbacks to measuring T1 for temperature monitoring. The temperature dependence is tissue dependent and has to be calibrated in each type of tissue being used. The temperature sensitivity also changes abruptly in response to physiologic changes in tissue caused by heating which makes using T1 as a primary

measure of temperature problematic.[43–45] Additionally, the time required to make T1 measurements is limiting in the context of temperature monitoring. Traditional inversion recovery (IR) methods require several minutes to acquire multiple inversion times. Accelerated methods for sampling the magnetization recovery exist but typically requires minutes to acquire an image compared with seconds for PRF techniques[46–48] An alternative approach is the estimate T1 using variable flip angle (VFA) technique. This technique is especially sensitive to slice profile effects inherent to 2D imaging so it is generally necessitates a 3D acquisition with acquisition times on the order of minutes. [49] For these reasons temperature monitoring using T1 has been used as a complement to PRF monitoring in a research settings or in hyperthermia applications where temporal resolution is less critical.[32,50,51]

2.5.3 Transverse Relaxation Times (T2/T2*)

The transverse relaxation time (T_2) can also be written in terms of the intermolecular rotation of water molecules[36,52]:

$$\frac{1}{T_2} = k \left[3\tau_c + \frac{5\tau_c}{1 + \omega^2 \tau_c^2} + \frac{2\tau_c}{1 + 4\omega^2 \tau_c^2} \right] \qquad \text{2-10}$$

Where the non-frequency dependent term represents static alterations in the magnetic field that cause rapid loss of phase coherence. Unlike T1 relaxation, which requires field alterations that match the resonance frequency, the T2 relaxation time is sensitive to lower frequency field variations. While the expression in equation 2-10 is adequate for predicting T2 in non-viscous liquids such as pure water, it fails to explain why T2 values are 5-10 times lower than T1 in tissue. This observation coupled with the lack of observed frequency dependence of T2 values suggests that other mechanisms contribute significantly T2 relaxation.[36,37,53] This is typically attributed to diffusion of water molecules through static field inhomogeneities in the hydration layer.[54,55] The contribution of these processes are highly dependent on the specimen being imaged and makes a theoretical relationship between T2 and temperature elusive.

Early experiments by Belton[56,57] showed non-monotic temperature dependence at temperatures below room temperature but T2 has been empirically found to increase nonlinearly with temperature in the physiological range.[58] The relative increase is generally smaller compared to the simultaneous increase in T1[41] and shows similar nonlinear behavior when the structure of tissue is altered by coagulation[59,60]. Aside from the nonlinear nature and reduced sensitivity to temperature, measurement of T2 for temperature monitoring is impractical due to the long acquisition times required to acquire T2 maps compared to T1 maps.

When a gradient echo acquisition technique is used a relaxation rate, T2* is measured:

$$\frac{1}{T_2^*} = \frac{1}{T_2} + \frac{1}{T_2'}$$

2-11

Where T_2' represents the dephasing caused by macroscopic magnetic field inhomgeneities from macroscopic susceptibility interfaces and the imperfect B_0 field that are traditionally refocused in spin echo type sequences. Few researchers have examined the temperature dependence of T2* but it is expected to follow the same dependence at T2 with a near constant contribution form field inhomogeneities. One notable exception may be found as susceptibility interfaces where the small but nonzero temperature dependence of magnetic susceptibility may contribute a temperature dependence of T_2' (see section Magnetic Susceptibility). One study by Taylor et al. qualitatively confirmed this behavior by observing increases in T2* with increasing temperature until samples reached temperature typically associated with coagulation. While T2* inherently suffers from most of the same limitations as T2 for temperature monitoring, it can be mapped with much faster multi-echo gradient echo sequences and is a potential complement to traditional PRF monitoring given its sensitivity to changes in tissue state.

2.5.4 Magnetization Transfer (MT)

Magnetization transfer (MT) is MR contrast mechanism that is sensitive to protons in the hydration layers of macromolecules and is closely related to the theory of T1/T2 relaxation described in sections 2.5.2 and 2.5.3 . Protons in the hydration layer see a range of local magnetic fields which results in inefficient excitation by on resonance pulses and extremely short T2s. In a MT experiment an off resonance pulse is applied after which the saturated protons undergo fast exchange with free water. When a traditional imaging sequence follows the MT pulse the observed signal decreases due the exchange of these saturated hydration layer protons with the free water pool. The traditional quantity of interest in these experiments is the magnetization transfer ratio (MTR)

$$MTR = 1 - \frac{M_{MT}}{M_0} \qquad\qquad 2\text{-}12$$

Wher M_{MT} is the signal after the magnetization transfer pulse and M_0 is the signal without the magnetization transfer pulse.[61]

The exchange mechanisms characteristic of MT are temperature dependent and have been investigated as a method for monitoring temperature. However, there are conflicting reports of whether MTR increases or decreases with temperature[59,62,63] The response appears to be highly tissue dependent and possibly sensitive to competing interactions involving macromolecules in the sample. Similar to T1 and T2, nonlinear changes in MT temperature dependence are associated with changes tissue state which limit its use for temperature monitoring but make it of interest for monitoring tissue damage. MT pulses can be implemented relatively easily into traditional gradient echo temperature monitoring techniques as a complement to traditional PRF monitoring. However, this comes with a loss of SNR and slightly increased acquisition time. Additionally, the choice of echo time(s) must be chosen judiciously to balance the competing need of high SNR for MT contrast and the temperature sensitivity of the PRF.[62]

2.5.5 Diffusion

Diffusion of water protons is another temperature dependent MR parameter that can be measured when diffusion sensitizing gradient are employed. If all other sequence parameters are held constant the addition of these gradients is given by

$$S \propto S_0 e^{-bD} \qquad \qquad 2\text{-}13$$

Where b is a characteristic parameter of the diffusion sensitizing gradients and D is the diffusion coefficient. The temperature dependence of the diffusion coefficient, D, is similar to T1 as it is also governed by the Boltzmann distribution:

$$D \propto e^{-E_D/kT} \qquad \qquad 2\text{-}14$$

Where E_D is the activation energy of the diffusion process. Diffusion has a relatively high temperature sensitivity of approximately 2% per degree and has been employed for temperature monitoring phantoms[64–66] and in vivo[67,68]. However, long imaging times and sensitivity to motion make practical implementation in vivo difficult. [26,69] Like T1 and T2, diffusion values also respond nonlinearly to changes in tissue state and is of interest for directly monitoring damage to tissue.[26]

2.5.6 Magnetic Susceptibility

The available longitudinal magnetization, M_0, for a given MR experiment is directly proportional to magnetic susceptibility, χ_0, of the material being imaged which has a temperature dependence governed by the Curie law:

$$S_0 \propto \chi_0 \propto \frac{1}{T} \qquad \qquad 2\text{-}15$$

The magnetic susceptibility cannot be easily isolated in an MR experiment so this temperature dependence practically manifest as a decrease in signal. The dependence is relatively small and on the order of 0.3%/°C.[26] This small temperature dependence combined with the long imaging times required to remove relaxation effects from the observed signal make it a poor choice

for direct temperature monitoring. However, it is important to consider this dependence in certain situations such as at susceptibility interfaces[70] and when interpreting changes in signal intensity with temperature rather than maps of other intrinsic MR parameters.

2.5.7 Thermal Dose

MRTI is an integral part of monitoring thermal therapies but knowledge of the temperature history alone does not elucidate the state of treated tissue. Thermal dose models are needed to fully understand the effect of heat on tissue. In the most general sense a thermal dose model is a mathematical relationship that converts a temperature history into a probability of having some effect on tissue. These models can vary widely in complexity and their applicability is highly dependent on the procedure in question. On one extreme, tissue that reaches temperatures of 100 degrees Celsius is certainly nonviable, and a simple threshold model based on the maximum temperature is sufficient. For hyperthermia applications where temperatures are relatively low and treatment times are long, the relationship between temperature history and biological effect cannot be understood through intuition alone. Given the diffusive nature of heat, temperature histories between these extremes are unavoidable, with the possible exception of the highest power short duration FUS and LA procedures. A detailed treatment of thermal dose models and clinically relevant biological effects is left to Chapter 3.

2.6 MR for Thermal Therapy Assessment

The gold standard method for assessing the biological effects of ablation procedures is examination of the thermal lesion using histology. However, histologic examination is impossible to incorporate into the routine clinical workflow. Consequently, post-treatment imaging is the primary surrogate for assessing damage after therapy and providing a baseline for follow-up imaging and are integral to monitoring disease progression. While T2-weighted (T2-W) imaging and contrast enhanced T1-weighted (CE-T1-W) are routinely used in the clinic to identify the extent of the thermal lesion there are many additional MR contrast mechanisms that have been investigated to investigate various biological responses to thermal injury in tissue.

2.6.1 Physiology of the Thermal Lesion

The thermal lesion that occurs after an ablation procedure consists of two zones characterized by the physiological state of tissue.[2,4] The central zone is the area immediately surrounding the probe or FUS focus that receives the highest thermal dose. This area is characterized by a catastrophic breakdown in cellular and tissue function. Immediately outside the central zone is the peripheral or transition zone that consists of a mixture of tissue that will become nonviable via delayed processes such as apoptosis and tissue that will recover from reversible thermal injury. This zone is of primary interest as it borders untreated tissue and contains the margin of clinically meaningful damage. The biological processes governing the fate of tissue in this region are numerous and interconnected. They include but are not limited to: mitochondrial damage, DNA damage, induction of apoptosis and inflammatory immune response. Blood vessels are also disrupted in this zone, causing accumulation of fluid and local swelling.[71,72] In hyperthermia treatments, the central zone is absent since the objective is to modulate the biologic processes in tissue. The entire treated region can be considered analogous to the peripheral zone in ablation, albeit with exclusively sub lethal biological effects.

2.6.2 Clinical Imaging of the Thermal Lesions

When MRI is employed for guidance of a clinical ablation procedure, the most commonly used MR techniques for visualizing thermal lesions are T2-weighted (T2-W) imaging and contrast-enhanced T1-weighted (CE-T1-W) imaging.[1,73] Lesions are characterized by a nonenhancing central region that can be either hypo- or hyperintense with respect to surrounding normal tissue depending on tissue type and the time elapsed since treatment. For high temperature ablations, vascular stasis and the region of irreversible tissue damage are closely linked. Therefore, lack of enhancement on contrast-enhanced imaging is the most consistent attribute of this region so contrast is indicated and is often visualized using subtraction imaging. This region is generally considered to be synonymous with the central zone described in section 2.6.1 and contains only nonviable tissue. A peripheral region of altered intensity and/or contrast enhancement often develops following ablation and is attributed to leakage of contrast agent into the interstitial space due to damage to the vasculature and accumulation of fluid and/or inflammation-induced hyperemia.[73–78] This region is consistently observed in the brain where it expands in the first 1-40 days after treatment before reducing to pretreatment size within 16 weeks where it will continue to enhance on long term follow up.[74,79,80]

While a lack of enhancement is MR imaging can identify the central zone, the viability of tissue in the peripheral enhancing region is more nuanced. Some studies in the brain that have attempted to correlate this region with histology suggest that the enhancing/hyperintense ring remains viable[81–83] whereas others have suggested the opposite[7,84–87]. Given the complexity of the biological response, considerable uncertainties associated with registering images to histology, and the fact that the size of the hyperintense/enhancing rim changes over time makes a definitive determination on the viability of tissue in this region a challenge.[88]

2.6.3 Multi-Parametric Imaging of the Thermal Lesion

Several advanced MR techniques have been investigated for imaging thermal lesion that are potentially sensitive to specific biological effects in the peripheral zone. These have not been incorporated into routine clinical practice primarily due to time constraints and lack of consensus regarding their clinical utility. T1, T2, MT and diffusion were discussed in section 2.5 in the context of their temperature dependence and each suffered from the limitation that their dependence became nonlinear at high temperatures. At these high temperatures there is a complex interaction of different physiological effects that cause changes in intrinsic MR parameters. These include disruption of cellular membranes that restrict diffusion, denaturation and coagulation of proteins and blood, and increased fluid in the peripheral zone. These processes can have opposite effects on intrinsic MR parameters that manifest as changes that are highly dependent on tissue type. Variable results have been observed in a variety of *ex vivo*[59,63,89,90] and *in vivo*[91–93]studies. Generally, a consistent decrease in T1 is observed across a variety of tissue types while changes in T2 and MT are varied. Inconsistent changes in the apparent diffusion coefficient (ADC) have also been observed. Jacobs [94] et al observed an initial decrease in ADC immediately following FUS ablation of uterine fibroids but observed an increase upon 6 month follow up. This underscores that thermal effects in tissue are not static and can be highly dependent on when follow up imaging is performed. Dynamic contrast enhanced (DCE) MRI has also been investigated to evaluate the viability of the thermal lesion. In this technique, the uptake of intravenously injected contrast agent is monitored using serially acquired T1-weighted images to assess perfusion in tissue. Studies in animals[92,95,96] and humans[96] have associated changes in semi-quantitative and quantitative DCE parameters with regions that were distinct from the non-enhancing volume on traditional CE-T1-W imaging.

While multi-parametric imaging of thermal lesions is still investigational and has not been standardized for clinical use, these techniques have the potential to elucidate the complexities of

the biologic response in the thermal lesion. In a series of recent papers[91,92], Hectors et al. correlated the post-treatment measurements of several of MR parameters with histology. They found that no single MR parameter was sufficient for predicting damage in tissue and that a more specific prediction of the nonviable region could be made by applying clustering techniques to multiple parameters. These results suggest that multi-parametric techniques may provide complementary information to current clinically utilized methods and further investigation in clinical models is warranted. These results not only suggest that multiple MR contrast mechanism should be used for evaluating the thermal lesion but also that multiple thermal dose models that reflect each of these contrast mechanism may be most appropriate for monitoring.

Chapter 3: Thermal Dose Models

3.1 Introduction

Like any intervention, thermal therapies are only of clinical utility if the balance between therapeutic efficacy and patient safety is understood. In section 2.5 MRTI was described as a tool for monitoring these procedures in real-time. However, to maximize the utility of MRTI the measured temperature histories must be converted by some model into values predictive of thermal damage. Intuitively, one knows that the primary variables are the temperature and the duration of exposure and that there is some degree of variation in different tissues. Therefore, in principle, a thermal dose model should be able to predict the onset of a thermal damage for an arbitrary temperature history for a particular tissue. Several different models of thermal dose have been developed that vary widely in complexity and applicability to different types of thermal therapies. However, three models dominate the literature: The absolute rate (AR), the cumulative effective minutes (CEM), and critical temperature (CT) model.

3.2 Effects of Interest (EOIs) and Isoeffects

The defining characteristic of a thermal dose model is the effect of interest (EOI) that it is designed to predict. Many different EOIs have been used for thermal dose models and are intimately related to the experimental techniques used to measure them. EOIs can be categorized as quantitative or categorical based the types of data (in a statistical sense) that define them. They can also be categorized as intra-treatment effects or post-treatment effects based on when they are measured. For example, cell survival is a quantitative and post-treatment EOI since it is represented by a quantitative quantity (e.g. 63% cell survival) that can only be measured after thermal exposure. It is often useful to discuss these effects in terms of a specific value of the EOI, or isoeffect. In the previous example cell survival is the EOI and 63% survival is an isoeffect. In the special case of

categorical EOIs this distinction becomes trivial if the data are binary (e.g. enhancing/non-enhancing on post-treatment imaging). The subtle distinction between the types of EOIs and isoeffects are concepts are critical when discussing the theoretical basis of each thermal dose model.

3.3 Absolute Rate (AR) Model

3.3.1 Theory

The Absolute Rate (AR) model of thermal dose approximates a given EOI as a first-order irreversible reaction. Such a reaction can be described conceptually as

$$N \xrightarrow{k} D \tag{3-1}$$

Where a sample the in a native state, N, is irreversibly converted into a denatured state, D, with conversion rate k. If this process is assumed to be first order it can be described using a differential equation:

$$\frac{dN}{dt} = -kN \tag{3-2}$$

With solution:

$$ln\left(\frac{N_0}{N}\right) = \int_0^\tau k \, dt \tag{3-3}$$

The conversion rate can be related back to fundamental thermodynamic quantities using the Eyring equation from transition state theory

$$k = \frac{k_B T}{h} e^{\frac{-\Delta G^*}{RT}} \tag{3-4}$$

Where k_B is the Boltzmann constant, T is the temperature (^{0}K), h is Planck's constant, R is the universal gas constant, and ΔG^* is the Gibbs' free energy of formation. ΔG^* can also be expressed using the thermodynamic relation:

$$\Delta G^* = \Delta H^* - T\Delta S^* \tag{3-5}$$

22

Where ΔH^* is the enthalpy of formation and ΔS^* is the entropy of formation. The activation energy for a first order reaction is given by:

$$E_a = RT + \Delta H^* \cong \Delta H^*$$

<div align="right">3-6</div>

Which a reasonable approximation for physiological processes which have $E_a \sim 10^5$ and $RT \sim 10^3$. Combining equations 3-3 through 3-6 an Arrhenius relationship is obtained[97,98]:

$$\Omega = \ln\left(\frac{N_0}{N}\right) = A \int_0^\tau k \, dt = A \int_0^\tau e^{\frac{-E_a}{RT(t)}} \, dt$$

<div align="right">3-7</div>

Where Ω is a unitless damage parameter and the pre-exponential term defined as:

$$A \equiv \frac{k_B T}{h} e^{\frac{\Delta S^*}{R}}$$

<div align="right">3-8</div>

Despite the explicit temperature dependence in equation 3-8, it is assumed to be insignificant compared to the temperature dependence in the exponential term and is often treated as a constant over the range of temperatures involved in thermal therapies.[99,100] This constant, dubbed the frequency factor, and the activation energy together make up what are called the Arrhenius parameters and define the damage process for a given EOI. While Ω has been used historically, its physical significance is not intuitive and its value increases exponentially to impractically large values. Often a more practical quantity of interest is the fractional conversion (FC):

$$FC(t) = 1 - e^{-\Omega(t)} = \frac{N(t)}{N_0}$$

<div align="right">3-9</div>

which is easily interpreted as the fraction of the sample that has been converted to the non-native state and is bounded from 0 to 1.

3.3.2 Experimental Measurements

Measurement of the Arrhenius parameters is complicated by the transcendental nature of equation 3-7 and cannot generally be solved analytically. Laboratory experiments are designed such that T is constant[101–105] (isothermal) or linearly increasing[106–109] so that the right hand side of

equation 3-7 can be solved analytically for A and E_a. This traditionally precludes the use of ablation

and hyperthermia data because of the inability to precisely control the temperature throughout the

experiment. The quantitative nature of Ω or FC make the AR model well suited for describing

quantitative EOIs provided they can be experimentally measured. In practice, quantitative

measurements in tissue are impractical or impossible for many relevant EOIs and many models are

derived from gross observations in the affected tissues that are categorical in nature. In these cases,

values of Ω or FC are typically arbitrarily assigned (e.g. Ω=1, $FC = 63$ %) for a given EOI for the

purposes of model fitting.[97,110] This is particularly challenging when using histopathological EOIs

which suffer from the additional uncertainties associated with relating the temperature history

location back to the area evaluated histopathologically.

A review of the kinetic parameters that define various biological processes can provide

additional insight into the effect of heat on tissue. Regardless of the type process being examined, a

plot of the activation energy versus of the log of the frequency factor approximately follows a

straight line. This empirical relationship has been measured independently by Rosenberg,[111] and

Wright,[112] and in this work we use the relationship measured by He and Bischof [98] (Figure 3-1):

$$\log(A) = 3.80 \times 10^{-4} E_a - 9.36 \qquad \text{3-10}$$

If this result is compare to theory by writing the frequency factor explicitly as a function of

the activation energy by combining equations 3-4 and 3-8 to obtain:

$$ln(A) = \frac{\Delta E}{RT} + ln\left(\frac{k_b T}{h}\right) - \frac{\Delta G^*}{RT} \qquad \text{3-11}$$

Comparing equation 3-10 and 3-11 shows that the slope is remarkably close to the range of

values of 1/RT in the ablation temperature range (3.9×10^{-4}-3.3×10^{-4} for 90^{0}C to 37^{0}C). A constant

intercept implies only a small change (100-110 kJ/mol) in the Gibb's free energy as a function of

temperature, which is characteristic of the thermal denaturation of proteins.[98] This relationship is

incredibly useful as a rule of thumb when trying to ascertain the validity of measured coefficients.[99]

In cases where non isothermal experiments are used to determine the Arrhenius coefficients this relationship can be used as a constraint on the nonlinear optimization problem to make it more tractable.[108] A second trend that observed in the values is tendency for both the activation energy and frequency factor to decrease in magnitude as temperature increases. This is seen in isothermal experiments by the addition of a break point in the coefficients or in dynamic experiments as lower activation energies for high end temperatures.
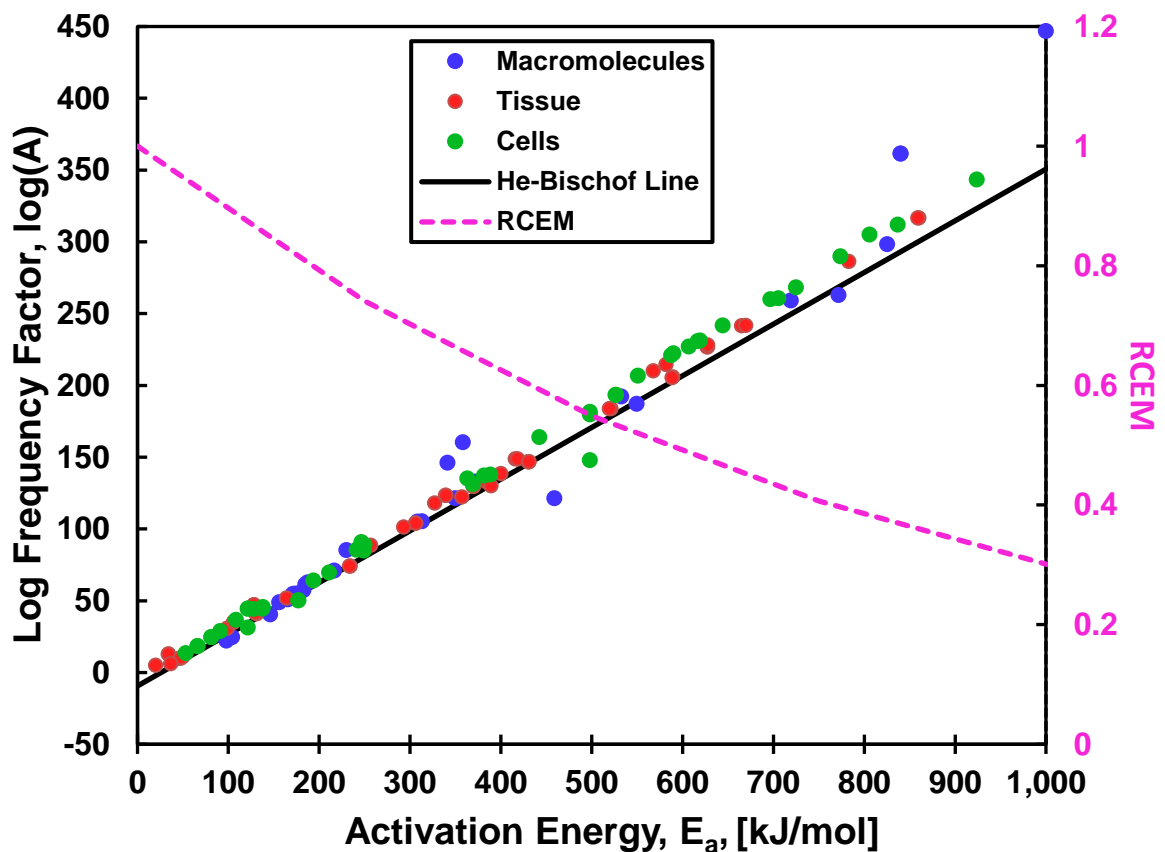
Figure 3-1: Selected Arrhenius parameters. Arrhenius parameters compiled by Wright[112] and He and Bischof[98] for macromolecules (blue), tissues (red), and cells (green).The empirically derived He-Bischof line (black; equation 3-10) shows the correlation between the experimentally measured values. The equivalent RCEM values (magenta; equation 3-13) are shown as a function of activation energy for reference.

3.4 Cumulative Effective Minutes (CEM) Model

The CEM model is a fundamentally different approach to modelling thermal injury that seeks to normalize the time required to reach an observed effect after a time history, $T(t)$, to an

equivalent exposure at a constant reference temperature, T_0. However, the CEM model still relies

on the same Arrhenius kinetics as the AR model. For isothermal exposures at two temperatures, T_A

and T_B, the times, t_A and t_B, required to reach an arbitrary dose is defined by the reciprocal of the

rate, k, in equation 3-7. The ratio of these times is given by:

$$\frac{t_A}{t_B} = \frac{e^{-\frac{E_a}{RT_B}}}{e^{-\frac{E_a}{RT_A}}} = \left(e^{\frac{-E_a}{RT_A T_B}} \right)^{(T_A - T_B)} \tag{3-12}$$

In the special case of $T_A = T_0$ and $T_B = T_0 + 1$ a constant, R_{CEM}, is defined by

$$R_{CEM} \equiv e^{\frac{-E_a}{R(T_0+1)T_0}} \tag{3-13}$$

If the exponential term in equation 3-14 is approximated by R_{CEM} (i.e. temperature

dependence is negligible) and an arbitrary temperature distribution and single reference

temperature (i.e. $T_A = T_0$ and $T_B = T_B(t)$) are considered the CEM model equation can be

derived:

$$\text{CEM} = \int_0^\tau R_{CEM}{}^{T_0 - T(t)} \, dt \tag{3-14}$$

Where CEM is the cumulative effective minutes and represents how long a similar

experiment would take if the temperature were held constant at the reference temperature.

The CEM model was originally developed for hyperthermia research at relatively low temperatures

(<47^{0}C) which somewhat justifies the assumptions needed to derive equation 3-14 from 3-10 but

becomes suspect when extended to higher temperatures observed during ablation procedures.

These simplifications also demand that the value of R_{CEM} be determined using an isothermal

experiments near the reference temperature. Early studies focused primarily on cell survival

measured *in vitro* for a variety of cells lines. However, as practical matter, the values chosen by

Sapareto and Dewey[102] are used almost exclusively in thermal therapy literature. These values

correspond to R_{CEM} of 0.5 and 0.25 for temperatures above and below $T_0 = 43°C$, respectively. This

model is referred to with the subscript "SD" (e.g. R_{CEM-SD}) to distinguish it from the more general

version in equation 3-13.

Despite being based on the same kinetics, the relative nature of the CEM model has

important practical implications. Unlike the AR model, which is inherently capable of predicting

quantitative EOIs, CEM values are meaningless without an associated isoeffect. Additionally, the

R_{CEM-SD} model implicitly assumes that the kinetics of all processes are the same which is not

supported by the R_{CEM} dependence on activation energy from equation 3-13 (Figure 3-1).

3.5 Critical Temperature (CT) Model

The CT model differs from both the AR and CEM model in that the entire temperature

history is assumed to contribute negligibly to the prediction of thermal damage. Instead, tissue is

classified on whether it achieved some critical temperature, T_c,:

$$D = H\big(max\big(T(t)\big) - T_c\big)$$

3-15

where H is the Heaviside step function and $D = 1$ and $D = 0$ correspond to denatured and

native tissue, respectively. The maximum temperature term in equation 3-15 makes the CT model

especially sensitive to the noise and temporal resolution of temperature measurements. It also

limits its application to categorical EOIs. Since the time dependence of the onset of thermal damage

is ignored, this approach can only be realistically applied to single high temperature/short duration

exposures and explains its prominence in FUS literature.

Like the CEM model, the CT model can be connected back to the AR model. Taking the

derivative of equation 3-7 and setting it equal to an isoeffect of interest, $\Omega = \Omega_C$, one can get a

second representation of the critical temperature (T_c'):

$$T_c' = \frac{E_A}{R\left(\ln\frac{A}{\Omega_C}\right)}$$

3-16

which represents the temperature that will result in the dose of interest if achieved instantaneously. While these quantities are roughly analogous, T_c' is theoretical in nature and implicitly assumes that the temperature history is a delta function whereas measurements of T_c are practically convolved with previous temperature exposure. As such, one should expect T_c' to be higher than T_c.

3.6 Application to Thermal Therapies

Each of the previously described dose models have been applied in thermal therapies. Traditionally, the focus of previous research has been to measure Arrhenius or CEM parameters in the laboratory and correlate the calculated doses with a categorical EOIs observed using imaging or histology. Few studies[87] have attempted to derive model parameters directly from histologic or radiologic endpoints due to the inability to control the temperature with high precision.

The Henriques[97] skin burn model ($\Omega = 1$) has been correlated with acute coagulative necrosis observed on H&E stained samples[113] and has been incorporated into a commercial laser ablation system. Sherar et al.[114] examined the correlation of three different models with post-treatment imaging and histology after MWA in rabbit brain. The Jacques[103] model correlated with the central region on post-treatment T2-W imaging while the Borrelli[104] and Brown[105] models correlated with the transition region using an isoeffect of $\Omega = 4.9$. However, this agreement was found to be insensitive to the chosen isoeffect, an observation that was corroborated by Yung[115] in canine brain. This is attributed to the exponential nature of equation 3-7 which causes rapid dose increases. While the corresponding uncertainty in dose threshold may be inconsequential for experiments with high dose gradients, it is expected to have a larger impact for procedures involving lower temperatures and longer exposures.

Dose thresholds have also been derived from histologic and radiologic EOIs using the CEM model. 240 minutes at 43°C has traditionally considered to be a conservative threshold for complete

coagulation.[116] However, many studies have shown a large range for the onset of coagulation and/or

necrosis for doses that are up to an order of magnitude smaller.[117–119] This can be explained by

variations in tissue type and the fact that equation 3-14 increases exponentially like equation 3-7.

The CEM model is implemented into one clinical laser ablation systems at with three different dose

thresholds with three dose levels (2,10,60 minutes) the correspond to low, intermediate, and high

thermal doses.[8]

High uncertainties in the thresholds observed using the CEM model has led at least one

author[119] to advocate using the critical temperature model. As previously mentioned in section 3.5,

these applications come almost exclusively from FUS literature since the short duration high

temperature exposures are most appropriate for the CT model. Within a single experiment, the

uncertainty in T_c is much smaller than the AR or CEM model. However, T_c values reported across

different studies vary from as low as 48°C-60°C based on modality used and length of

exposure.[27,115,119,120]

There are several limitations in the way that thermal dose models are applied to ablation

procedures. Both the AR and CEM models rely on model parameters that are derived from

experiments that only approximate biological effects in tissue. The implicit assumption that the

kinetic parameters are similar can be mitigated by empirically determining thresholds for particular

EOIs. However as this method is associated with high uncertainty and can only be considered valid

for the types of experiments that were used to derive the thresholds. Similarly, the CT model

necessarily relies on this empirical analysis. Thus, there is a need for determining model parameters

that are EOIs specific, especially as the number of clinically relevant EOIs expands.

Chapter 4: A Multi-Parametric Pulse Sequence for Thermal Therapy Monitoring

4.1 Introduction

Clinically utilized imaging EOIs are currently almost exclusively based on post-treatment imaging. These are usually longer acquisitions which take considerable time to acquire. The current standard approach for thermal ablation is to identify the region of damaged tissue by administration of contrast agent in order to assess the regions which have lost perfusion. In section 2.5 the temperature dependence of several intrinsic MR parameters was reviewed. Consistent with prior literature, it was demonstrated that these parameters changed linearly with temperature. However, as tissue is irreversibly damaged, and substantial changes in the chemical environment alter the rate at which these parameters change with temperature. These changes in linearity have been widely considered to be a liability in the context of providing an independent means of temperature monitoring during high temperature thermal ablation therapies. However, when this information is instead used in conjunction with temperature monitoring, such as from the PRF shift, there is potential to be used as direct measurement of tissue damage during treatment. Multi-parametric pulse sequences that measure multiple temperature sensitive parameters simultaneously are of interest for direct damage monitoring and for training thermal dose models because they provide pixel-wise information on tissue temperature and state throughout the entire procedure. In this chapter, a multi-parametric MR sequence is designed for this purpose. An existing multi-echo pulse sequence is modified so that the flip angle can be altered in dynamic fashion for real-time estimates of the PRF, R2*, and T1 during thermal therapy procedures. The modified sequence is validated against the product pulse sequence and the ability to quantify each of the parameters is investigated.

4.2 Methods

4.2.1 Pulse Sequence Design and Validation

The multi-parametric pulse sequence was designed for a clinical 3T MRI scanner (Discovery

750; GE Healthcare Technologies; Waukesha, WI) using the EPIC pulse sequence design

environment. Modifications were made to the product fast gradient-recalled echo (FGRE) source

code, which serves as the basis for a majority of the product 2D gradient echo sequences. This

custom sequence was renamed 'mfamfgre2d' (multi-flip angle, multi-echo FGRE 2D) and the pulse

sequence diagram for a single phase utilizing unipolar readout is shown in Figure 4-1.
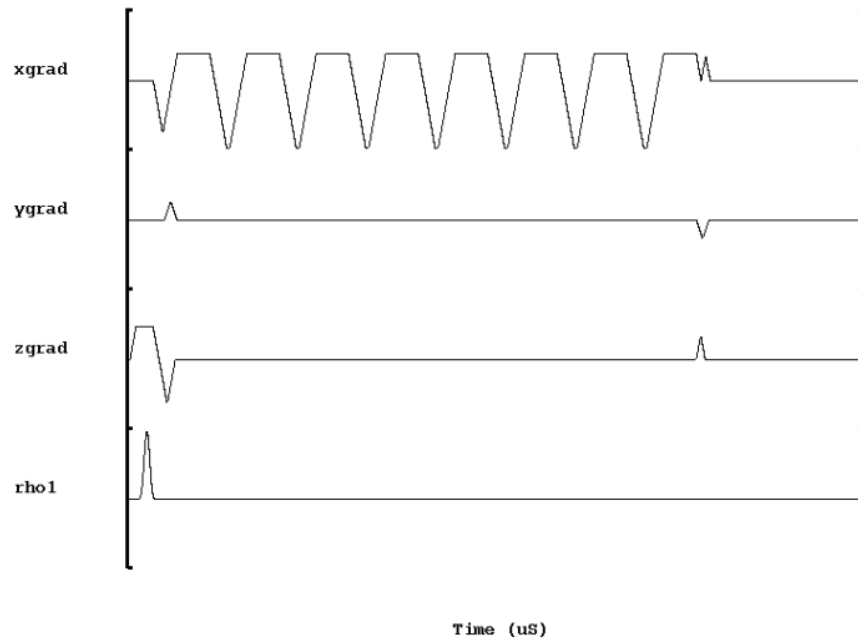
Figure 4-1: Mfamfgre2d pulse sequence diagram. RF pulse amplitude and gradient waveforms for slice (zgrad), phase (ygrad), and unipolar frequency (xgrad) encode gradients.

Although multi-phase (i.e. time points) and multi-echo options are available within the product FGRE sequence, the source code had to be modified to make both options available simultaneously. The flip angle was controlled at each acquisition phase by scaling the RF pulse amplitude using the control variable (CV) 'ia_rf1'. This CV represents the amplitude of the RF pulse relative to the value determined during automated tuning of the scanner prior to acquisition (e.g., 'prescan') and has a maximum value of 2^{15}-1=32,676. The value of this CV can be written as a function of the desired flip angle, α, and the nominal flip angle, α_{nom} if the small flip angle approximation [121]holds:

$$ia\_rf1 = \ 32{,}767 * \frac{\alpha}{\alpha_{nom}} \qquad \text{4-1}$$

Use of the small flip angle approximation limits the application of this sequence to flip angles of approximately <30°. However, in this sequence the RF pulse is optimized using a Shinnar-Le Roux algorithm[122] and so the shape of the RF pulse is automatically changed as the flip angle changes for SAR and timing purposes. One of the thresholds for transition between different RF shapes occurs at 30° which provides a practical reason for restricting the available flip angles and justifies the small flip angle assumption. While higher flip angles may be used, the change in the shape of the pulse could reduce the accuracy of the calculations.

Two additional CVs were added to allow the operator to control the behavior of the sequence at the scanner console without recompiling the source code. The first, 'mfa_mode', defines how the flip angle changes with each phase. Three options are available: constant flip angle (mfa_mode=0), alternating flip angle (mfa_mode=1), and a continuously decreasing flip angle. In the case of alternating flip angle, an additional CV, 'mfa_low_flip', controls the value of the second flip angle. The dependence of the flip angle on the mfa_mode variable, total number of acquisition phases, N_{phases}, and current acquisition phase, n_{phase}, is given in Table 1.

Multi-Flip Angle Scheme	mfa_mode	Flip Angle
Constant	0	$\alpha = \alpha_{nom}$
Alternating	1	$\alpha = \begin{cases} \alpha_{nom}\,(n_{phase} = odd) \\ \alpha_{nom}/mfa\_low\_flip\,(n_{phase} = even) \end{cases}$
Continuously Decreasing	2	$\alpha = \alpha_{nom}\left(1 - \dfrac{n_{phase} - 1}{N_{phases}}\right)$

Table 1: Flip angle control using the mfa_mode control variable

A phantom experiment was designed to validate the performance of the modified FGRE source code did not have unintended consequences on the pulse sequence. A phantom was designed containing 8 50 mL centrifuge tubes with different concentrations (0.06-0.42 mM) of Gadolinium based contrast agent (Omniscan, GE Healthcare Technologies, Waukesha, Wisconsin) in deionized water. The phantom was placed in a transmit-receive quadrature birdcage head coil and images were acquired at 5 flip angles using the mfamfgre2d sequence. (FOV=25.6 x 25.6 cm, TR= 50 ms, 8 echoes, TE_{min}=1.4 ms, ESP=1.7 ms, RBW=390 Hz/pixel, slice thickness=5mm, α=10,15,20,25,30, N_{slices}=1). Two nearly identical FGRE scans were acquired sequence by manually scaling ia_rf1 between acquisitions. Only the first echoes were used for analysis due to a slight (.1 ms) discrepancy in echo spacing. A rectangular ROI was drawn just inside the phantom edges to isolate voxels with significant signal and assure Gaussian distributed noise. (Figure 4-2). Every voxel within this ROI was compared using Bland-Altman analysis for the two identical FGRE sequences to identify the baseline differences caused by noise. A second Bland-Altman analysis was performed to compare the mfamfgre2d sequence and one of the product FGRE sequences in order to detect any systematic differences between the sequences.
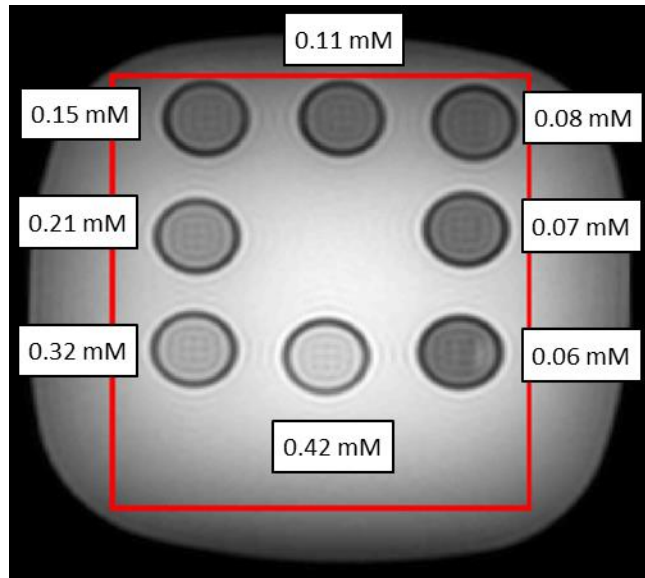
Figure 4-2: Phantom setup and ROI used for comparison of mfamfgre2d and FGRE sequences. The ROI was chosen to contain areas with signal due to the non-Gaussian noise properties at low SNR. Gadolinium concentrations increase counter-clockwise from bottom right corner. Gadolinium concentrations/T1s: 0.06 mM/1214 ms, 0.07mM/1195ms, 0.08mM/1143ms, 0.11mM/1011ms, 0.15mM/877ms, 0.21mM/731ms, 0.32mM/560ms, 0.42mM/461ms.

4.2.2 Object Oriented Multi-Parametric Post-Processing

An object oriented framework was implemented in the MATLAB (Mathworks, Natick, MA) environment to facilitate multi-parametric processing of the mfamfgre2d sequence. The primary design goals were to create self-contained object that reduces the memory use and to streamline routine processing tasks to make them as fast and flexible as possible. The constructor method loads DICOM images into the object as native 16-bit integers, which reduces the memory required (4x) compared with the MATLAB default of double precision. PRF, R2*, signal magnitude, and temperature were all calculated using the autoregressive moving average (ARMA) approach developed and investigated by Taylor, *et al*[34] that models the signal as damped exponentials in complex space. Methods developed were for calculating ARMA coefficients with an ROI in parallel, simultaneously reducing the required memory and processing time for the most computationally expensive step. Once the ARMA coefficients are known, the calculation of parameters maps is trivial from a computational perspective so each map was implemented as a dependent method to further

reduce the required memory. Additional properties are available to define the options for processing. For example, when calculating temperature, the temperature sensitivity coefficient and drift correction ROI are determined from corresponding properties within the object and allows fast and robust changes to processing. This object oriented framework greatly expedites the multi-parametric processing, especially as the number of time-points, echoes, and model order increases.

4.2.3 PRF/T2* Dependence on Flip Angle

Multi-flip angle capability was incorporated into the mfamfgre2d sequence to enable T1 quantification. However, it is important to ensure that this addition does not adversely impact quantification of the other two parameters of interest: PRF and T2*. A phantom containing 6 centrifuge tubes with different concentrations (0.04-0.62 mM) of Gadolinium based contrast agent (Omniscan, GE Healthcare, Waukesha, Wisconsin) in deionized water. The phantom was placed in the T/R quadrature head coil and images were acquired at 12 flip angles using the mfamfgre2d sequence. (FOV=25.6 x 25.6 cm, TR= 30 ms, 8 echoes, TE_{min}=1.4 ms, ESP=1.7 ms, RBW=390 Hz/pixel, slice thickness=5mm, α=2.5°-30° N_{slices}=1). This sequence was repeated 5 times to get assess the uncertainty in the signal measurements. Average values of PRF and T2* were measured in a 5x5 pixel ROIs for each repetition and Gadolinium concentration using in the center of each centrifuge tube. (

Figure 4-3) A one way analysis of variance (ANOVA; α=0.05) was performed for each concentration to assess whether the any of the mean parameter were significantly different at any of the flip angles. In cases where a difference was observed, a Tukey-Kramer (α=0.05) multiple comparison test was used to identify which flip angles were significantly different from one another.
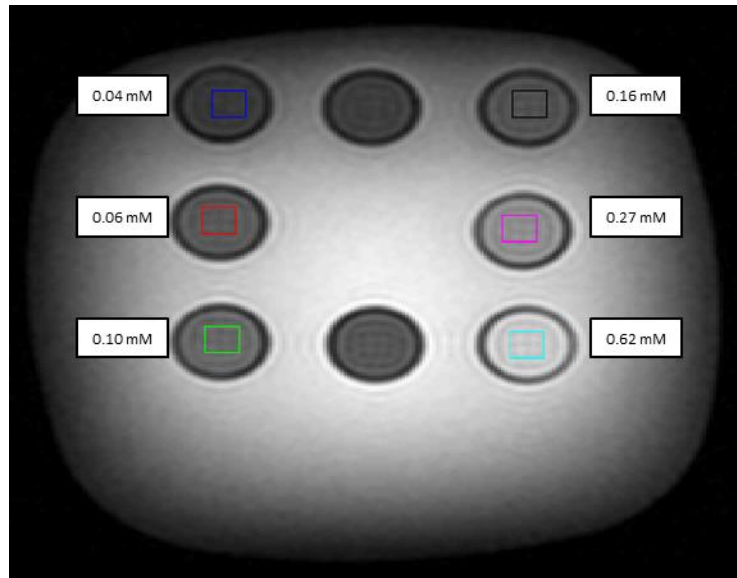
Figure 4-3: Setup and ROIs for assessing the dependence of PRF and T2* on flip angle. Each centrifuge tube analyzed contains Gadolinium based contrast agent. Gadolinium concentrations/T1s: 0.04 mM/1303 ms (blue), 0.06 mM/1214 ms (red), 0.10mM/1085 ms (green), 0.16mM/881 ms (black), 0.27mM/633 ms (magenta), 0.62mM/340 ms (cyan).

4.2.4 Temperature Sensitivity Coefficient

A critical component of temperature imaging is validation of the temperature sensitivity coefficient, β, that relates changes in the PRF to temperature (equation 2-2). The temperature sensitivity coefficient was measured in two separate phantom experiments by comparing the change in PRF with an independent temperature measurement during laser heating. Each phantom was composed of 50% egg white (Crystal Farms, Minnetonka, MN) and 50% deionized water by volume mixed with 1.5% agarose (weight/volume) (A0169, Sigma-Aldrich, St. Louis MO) and Gadolinium based contrast agent (0.06mM/0.21mM; Omniscan, GE Healthcare, Waukesha, WI). A water-cooled diffusing tip laser fiber (VCLAS-400-12-T10-11, Medtronic Navigation; Louisville, Colorado) attached to a 980nm diode laser (Photex15, Biotex, Houston, Texas) was inserted into the phantom. A fluoroptic temperature probe (m3300/STB, Lumasense, Santa Clara CA) was inserted within a few cm of the diffusing fiber tip. The phantom was exposed a 10 W for 8-9 minutes while monitored using the mfamfgre2d sequence. (field of view (FOV)=25.6 x 25.6/19.2x19.2 cm, TR= 35

ms, 8 echoes, minimum echo time (TE$_{min}$)=2.5/2.1 ms, echo spacing (ESP)=2.5/2.1 ms, receiver

bandwidth (RBW)=195/325 Hz/pixel, slice thickness=3mm, number of slices =1, α=30,

mfa_mode=1/0, mfa_low_flip=2/2, time between phases=4.8s). The temperature values measured

using the fluoroptic probe were interpolated to match the MRTI temporal resolution. The

temperature sensitivity coefficient and the 95% confidence intervals were calculated using linear

regression ("regress", MATLAB, Mathworks, Natick, MA) on the PRF values measured using MRTI in

a single pixel at the probe tip and the interpolated fluoroptic probe measurements.
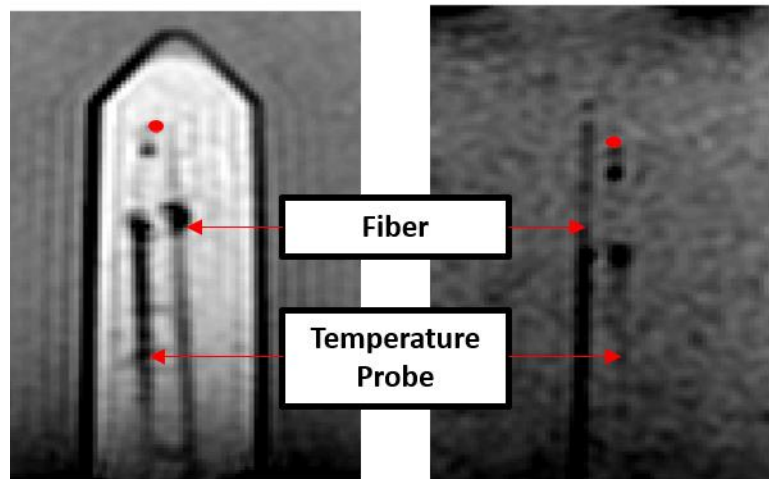
Figure 4-4: Setup and pixels of interest for two temperature sensitivity coefficient measurements in phantom. The position of the laser fiber and temperature probe are indicated by regions of low signal on magnitude images. The pixels used for the temperature sensitivity measurements (red) were identified by comparing images with multiple echo times and using knowledge of how far the temperature probe extended beyond the introducing catheter.

4.2.5 T1 Quantification

Multiple-flip angle capability was incorporated into the mfamfgre2d sequence for the

purposes of evaluating the quantification of the T1 relaxation time during the MRTI acquisition.

Theoretically, the steady state signal, S, of a spoiled-gradient echo sequence as a function of flip

angle, α, is given by:

$$S = S_0 \frac{(1 - E_1) \sin(\alpha)}{1 - E_1 \cos(\alpha)} \qquad \text{4-2}$$

where S_0 is the equilibrium magnetization and $E_1 = e^{-TR/T_1}$. In a multi-flip angle acquisition T_1 can be found using nonlinear regression techniques or by linearizing equation 4-2:

$$\frac{S}{\sin(\alpha)} = E_1 \frac{S}{\tan \alpha} + S_0(1 - E_1) \qquad \text{4-3}$$

The number and choice of flip angles for dynamic T_1 mapping must balance the tradeoff between temporal resolution and the accuracy and precision of the measurement. Several studies have shown that that high precision can be maintained with only two flip angles provided that optimal flip angles are chosen.[48] However, it should be noted that T_1 accuracy can be biased at low SNR due to Rician noise properties of the MR signal[123]. The optimal flip angle pair is given by:[124,125]

$$\alpha_{opt} = \cos^{-1}\left(\frac{E_1 \pm \sqrt{2}(E_1^2 - 1)}{2 - E_1^2}\right) \qquad \text{4-4}$$

Or alternatively:

$$S(\alpha_{opt}) = 0.71 \times S(\alpha_E) \qquad \text{4-5}$$

Where $S(\alpha_{opt})$ is the signal at the optimal flip and $S(\alpha_E)$ is the signal at the Ernst angle $(\alpha_E = \cos^{-1}(e^{-TR/T_1}))$. The values of the optimal flip angles are plotted in Figure 4-5 for physiologic T1s and range of TRs that are compatible with ablation monitoring.
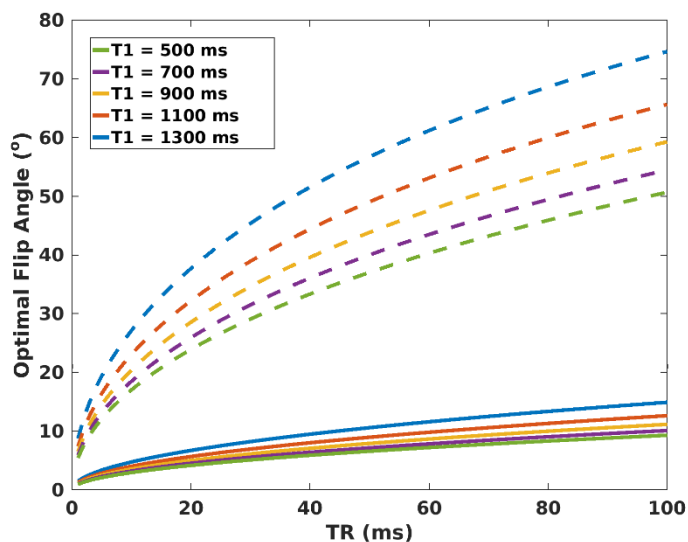
Figure 4-5: Optimal flip angle pairs for T1/TR combinations relevant for MRTI monitoring. For a given T1, there exists a pair of flip angles that optimize the precision of dual flip angle T1 measurements. One flip angle is higher (dotted) than the Ernst angle (not shown for clarity) and while the other is lower (solid) than the Ernst angle. T1 values were selected to represent physiologic values in tissue. Limits on TR were chosen to maintain temporal resolution consistent with ablation procedures (128 phase encode lines x 100 ms = 12.8s per image).

The above discussion of mapping T1 using optimal flip angles ignores the unavoidable contributions of B1 inhomogeneity caused by spatially varying conductivity and permittivity in the sample. B1 inhomgeneities cause the actual flip angle to deviate from the nominal flip angle in a spatially varying manner. Several methods[126–130] exist for mapping the B1 field so that equations 4-2 and 4-3 can be fit using the true flip angle at each pixel. In this work we use the Double Angle Method (DAM)[131] for primarily practical purposes as it does not require modification of pulse sequence source code. In the DAM method two images are acquired at angles α_{nom} and $2\alpha_{nom}$ with a long TR (>$5T_1$). After substituting into equation 4-2 and using the double angle formula the ratio of the two images can be written:

$$\alpha = \cos^{-1}\left(\frac{S(2\alpha_{nom})}{2S(\alpha_{nom})}\right) \qquad \text{4-6}$$

For the case of the mfamfgre2d sequence, slice profile effects significantly alter the measured signal as a function of flip angle. This is caused by a distribution of flip angles in the slice select direction. To account for these effects the mfamfgre2d time domain Shinnar-LeRoux (SLR) RF

pulse was plotted over a variety of flip angles using the WTools (GE Healthcare, Waukesha, WI) simulation environment and exported to MATLAB (MathWorks, Natick, MA) where it was Fourier transformed and scaled by the slice select gradient magnitude to convert to physical distance. Assuming that the slice profile is given by the Fourier Transform of the RF pulse is a reasonable approximation in the small flip angle regime. A plot of the slice profile as a function of slice thickness is shown in Figure 4-6. These slice profiles were used to numerically solve for the theoretical signal response, $S'(\alpha)$ as a function of the nominal flip angle by integrating equation 4-2 over α.[132]
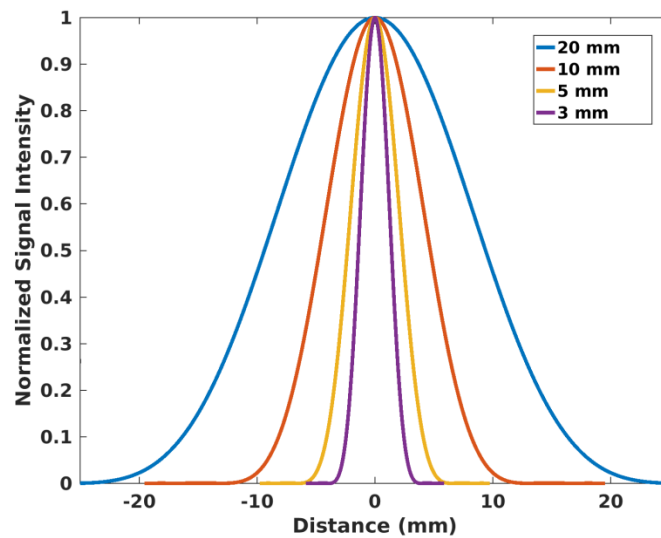
Figure 4-6: Mfamfgre2d slice profiles. Slice profiles were calculated by simulating the RF pulse in the WTools environment, performing a Fourier transform, and scaling by the magnitude of the slice encode gradient. These profiles assume the simulated RF pulse accurately reflects the true pulse experience by an object being imaged and that the small flip angle approximation holds

Phantom experiments were designed to evaluate the ability to quantify T1 using the mfamfgre2d pulse sequence. A phantom containing 8 centrifuge tubes with different concentrations (0.001-1.215 mM) of Gadolinium based contrast agent diluted in deionized water (Omniscan, GE Healthcare, Waukesha, Wisconsin). A ninth centrifuge tube was filled with 1:1 deionized water:lard (Armour, Grand Prairie, TX) mixture mixed with 1.5% agarose (weight/volume) (A0169, Sigma-Aldrich, St. Louis MO) and 4 lecithin dietary supplements (4.8 mg; CVS Pharmacy, Woonsocket, RI) as an emulsifier. The phantom was placed in the 32 channel head coil (GE Healthcare, Waukesha,

Wisconsin) and images were acquired at 12 evenly spaced flip angles using the mfamfgre2d

sequence. (FOV=19.6 x 19.6 cm, 128x128 acquisition matrix TR= 35 ms, 8 echoes, TE_{min}=1.6, ESP=2

ms, RBW=326 Hz/pixel kHz, slice thickness=5mm, α=2.5°-30°). The B1 field was mapped using a 12

flip angle mfamfgre2d (FOV=19.6 x 19.6 cm, 64x64 acquisition matrix, TR= 6,000 ms, 8 echoes,

TEmin=1.6, ESP=1.3 ms, RBW=326 Hz/pixel kHz, slice thickness=5mm, α=2.5°-30°). All T1 related

measurements used the first echo only. Gold standard T1 measurements for comparison were made

using an multi-inversion time fast spin echo (FSE) (FOV=19.6 x 19.6 cm, 256x256 acquisition matrix,

TR= 4000 ms, ETL=4, TE=8.3, RBW=244 Hz/pixel kHz, slice thickness=5mm,

TIs=50,75,100,150,250,500,750,1000,1500, 2000, 2500 ms) and fit using the IR signal equation:

$$S = S_0\left(1 + e^{TR/T_1} - 2e^{-TI/T_1}\right) \qquad\qquad 4\text{-}7$$

For each sequence and concentration the signal was averaged over a 9x9 ROI for analysis

(Figure 4-7).
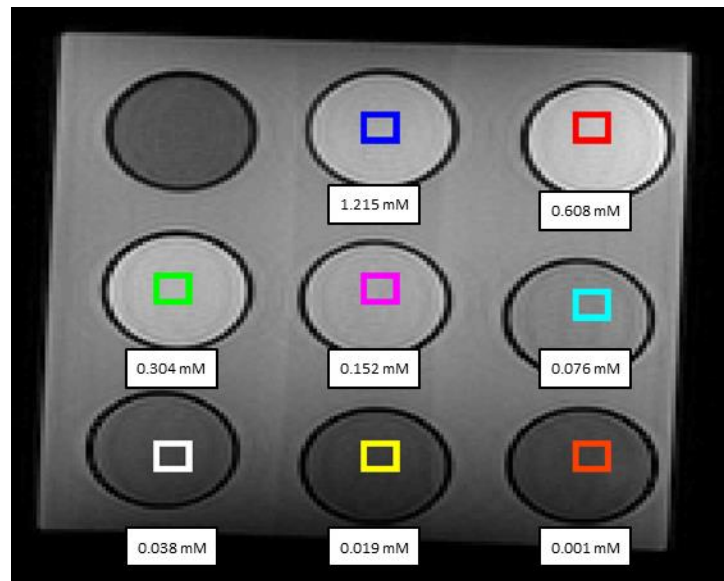
Figure 4-7: T1 quantification phantom and ROIs. Concentrations/T1s:1.2150 mM (blue), 0.6075 mM (red), 0.3038 mM (green), 0.1519 mM (magenta), 0.0759 mM (cyan), 0.0380 mM (white), 0.0190 mM (yellow), 0.0095 (orange)

The DAM method for B1 mapping also suffers from slice profile effects so the two sources of error cannot be corrected independently. A modified version of the technique described by Hsu[133] was used to correct for each effect simultaneously. Using this relationship a 5 step procedure was used to estimate T1 from the measured signal, $\widetilde{S_{T1}}$ and the measured DAM signal, $\widetilde{S_{DAM}}$: [133]

1. Derive an expression for the flip angle at the center of the slice profile, α_{cent}, as a function of the observed flip angle, α_{obs}, by simulating the DAM acquisition using $S'(\alpha_{cent})$ and calculating α_{obs} using equation 4-6.

2. Calculate α_{cent} for each DAM pair in $\widetilde{S_{DAM}}$ using equation 4-6 and $\alpha_{cent}(\alpha_{obs})$.

3. Estimate T_1 by fitting α_{cent} vs. $\widetilde{S_{T1}}$ using equation 4-2

4. Using the T_1 calculated in 3, calculate the theoretical ratio, k, between the observed signal $S'(\alpha_{cent})/S(\alpha_{cent})$

5. Divide $\widetilde{S_{T1}}$ by k to get S_{T1}', the signal one would observe in the absence of slice profile effects.

6. Iterate through steps 3-5 while replacing $\widetilde{S_{T1}}$ with S_{T1}' in step 3 but not step 4 (5 iterations)

The T1 values recovered using this iterative approach are compared to two other approaches for reference: a direct fit of $\widetilde{S_{T1}}$ using 4-2 (ignore B1 effects and slice profile effects) and a direct fit of $\widetilde{S_{T1}}$ using $S'(\alpha_{cent})$ (ignore B1 effects).

4.3 Results

4.3.1 Pulse Sequence Design and Validation

The pulse sequence modifications were successfully implemented and run on the GE MR750 scanner for 4 different software versions (DV23, DV24, DV25, DV2R2). The Bland-Altman comparison

between the signal magnitudes of the two FGRE scans is shown in Figure 4-8. The difference

between the two scans appears to be independent of the mean signal value and there is a

statistically significant (p<.01) mean difference of 0.3 AU with a 95% confidence interval from -29 to

28 AU. The same comparison is made between the FGRE sequence and mfamfgre2d sequence in

Figure 4-9. The mean difference is 0.054 AU and the 95% confidence interval ranges from -32 to 32

AU. In this case there is a slight but visible increase in the difference over a range approximately 750

to 1250 AU. Although these mean differences are statistically significant in both cases they are

inconsequential compared to the median signal value (≈1100 AU) and when the integer nature of

the signal magnitude is considered. There is a 7 AU increase in the 95% confidence interval when the

FGRE and which is also small compared to the median signal value. This is most likely caused by the

increase in the differences from 750-1250 AU, which is likely local in nature given its mean signal

dependence. This could be caused by minor alterations in the phantom that occurred between the

two scans (e.g. air bubble, motion) and is consistent with the timing of when the scans were

acquired (≈15 minutes between mfamfgre2d and FGRE vs. 3 minutes between FGRE and FGRE).
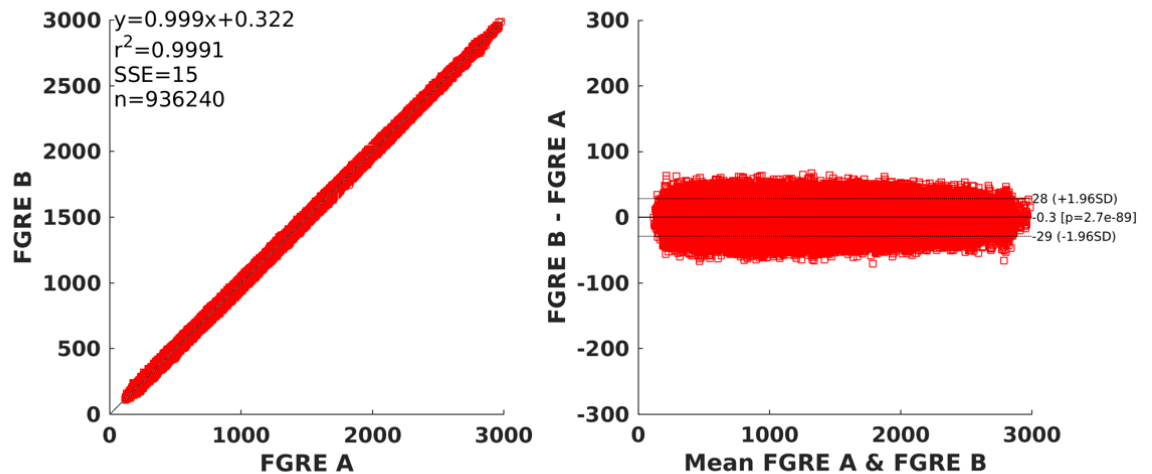
Figure 4-8: Bland-Altman comparison of signal values obtained using two identical FGRE sequences.
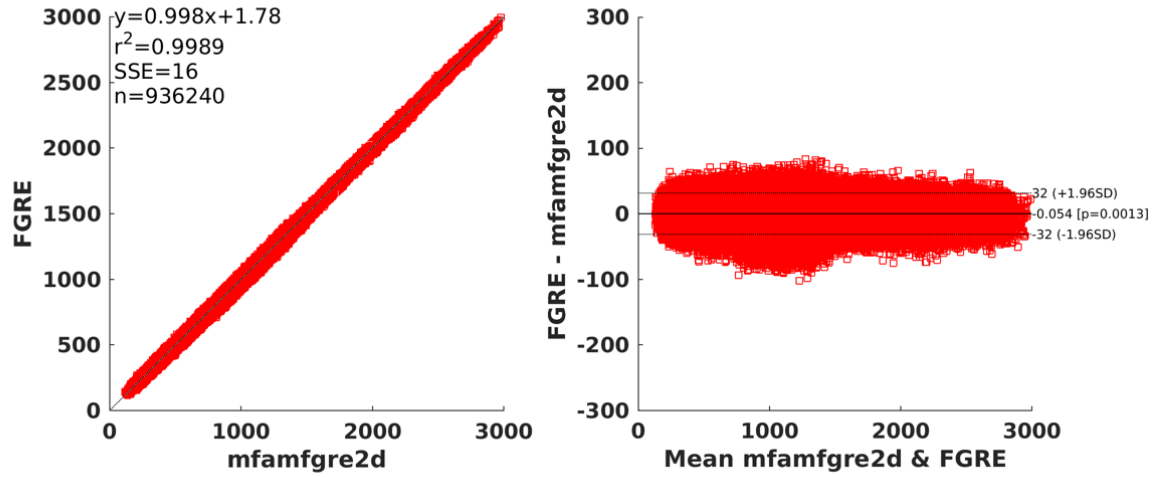
Figure 4-9: Bland-Altman comparison of signal values obtained using mfamfgre2d and FGRE sequences.

4.3.2 PRF/T2* Dependence

Representative examples of the PRF and T2* dependence on flip angle are shown in Figure 4-8 and Figure 4-9 and the p-values from the 1 way ANOVA are tabulated in Table 2. For PRF, no significant change with flip angle is observed with the exception of the 0.04 mM concentration. For T2*, a significant change with flip angle was detected at all concentrations except 0.06 mM and 0.62 mM. In each of these cases the Tukey-Kramer multi-comparison test reveals that the significant difference is only found at the lowest two flip angles (2.5°/5°) which suggests that the differences are SNR dependent rather than caused by alterations to the pulse sequence. Coincidentally, the only significant difference observed in the PRF measurements was found at the highest T1 and close to the edge of the coil, further supporting the difference is an SNR effect rather than a pulse sequence effect.
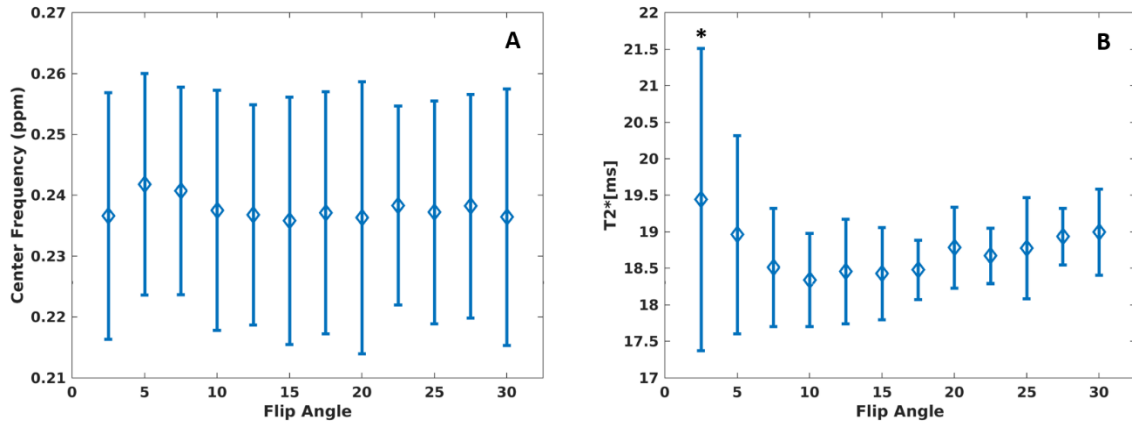
Figure 4-10: Representative comparison of PRF±2σ (A) and T2±2σ (B) as a function of flip angle. Flip angles with significantly different means are denoted by and asterisk (Concentration 0.06 mM; T1=1214 ms).*

T1 (ms)	1303	1214	1085	881	633	340
Concentration (mM)	0.04	0.06	0.10	0.16	0.27	0.62
PRF	**<0.01***	1.00	1.00	0.99	0.99	1.00
T2*	**<0.01***	**0.01***	0.02	**<0.01***	**<0.01***	0.90

Table 2: P-Values from ANOVA comparison of T2* and PRF values for each Gadolinium concentration. (p<0.01 bolded and with asterisk)

4.3.3 Temperature Sensitivity

The measured value of the temperature sensitivity coefficient and 95% confidence intervals were -0.0103(-0.0105-0.0101) and -0.0110(-0.0113-0.0106) which are consistent with the expected value -0.01 ppm/°C and the previous results measured by Taylor for the same sequence and post-processing technique. (Figure 4-11)[134]
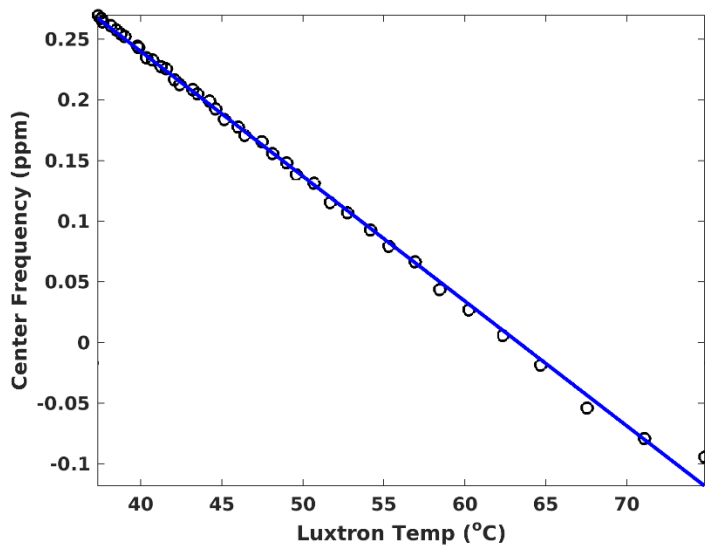
Figure 4-11: Example of temperature sensitivity coefficient measurement. A linear regression is performed between the temperature measurement made using a fluoroptic probe and the PRF values measured using MRTI.

4.3.4 T1 Quantification

The theoretical relationship $\alpha_{cent}(\alpha_{obs})$ for the mfamfgre2d sequence is plotted as function of the observed flip angle in Figure 4-10. The center flip angle is always greater than the observed flip angle and the deviation increases with the observed flip angle. This trend is closest to the results of Hsu[133] for a Hamming windowed 4-lobe sinc pulse. However, the magnitude of the difference is increased. This is not entirely unexpected because the mfamfgre2d pulse is approximately Gaussian and deviates from the ideal slice profile more than a truncated sinc pulse.
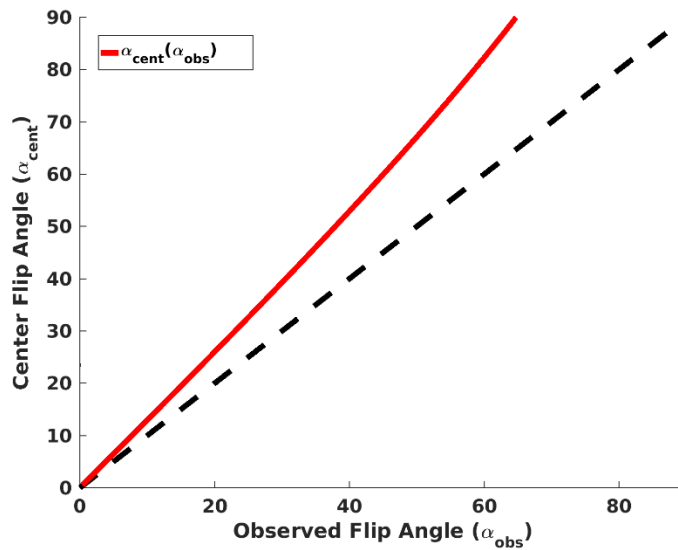
Figure 4-12: Center flip angle as a function of the observed flip angle measured using the DAM method. The relationship between the center flip angle and observed flip angle (red) is calculated by simulating the DAM experiment using $S'(\alpha)$. The line of unity (black dotted) is plotted for reference. This relationship can theoretically correct the observed flip angles using the DAM method for slice profile effects.

The results in Figure 4-10 were applied to the DAM acquisition to obtain the α_{cent} for each

flip angle pair and Gadolinium concentration and is expressed as a ratio $\alpha_{cent}/\alpha_{nom}$ (Figure 4-13)
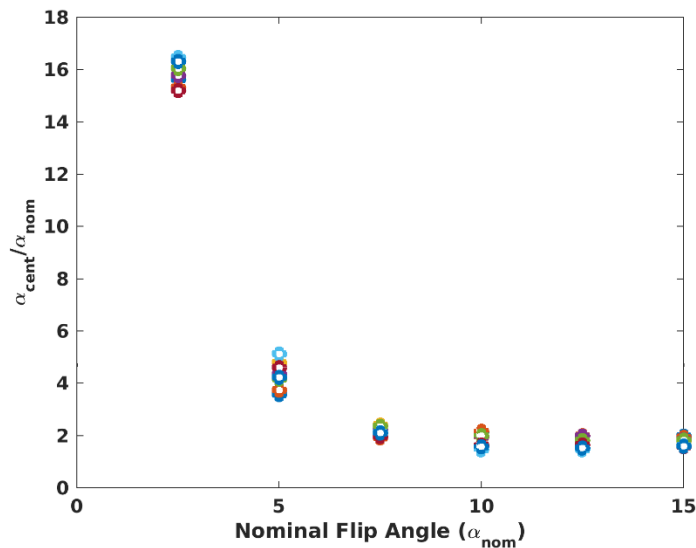
Figure 4-13: Center flip angle as a function of nominal flip angle for each Gadolinium concentration. Concentrations/T1s: 1.2150 mM (blue), 0.6075 mM (red), 0.3038 mM (orange), 0.1519 mM (purple), 0.0759 mM (green), 0.0380 mM (cyan), 0.0190 mM (maroon), 0.0095 (blue)

47

The measured center flip angle increases drastically at low flip angles to unrealistically high values. This is consistent with the contribution of the inherent bias in MR signal increasing at low flip angles. For this reason the center flip angles were scaled by the measured at 15° as this is the most reliable measurement. The flip angle ratios were 2.00, 1.94, 1.8, 1.85 1.82, 1.61 1.58, 1.60 for concentrations of 1.2150, 0.6075, 0.3038, 0.1519, 0.0759, 0.0380, 0.0190, 0.0095, respectively. When these flip angles the used to correct the signal the corrected values are far lower than the values measured using inversion recovery and had a minimum difference of approximately 100ms. (Figure 4-14) If no correction is made, a similar underestimation of T1 is observed (Figure 4-15)
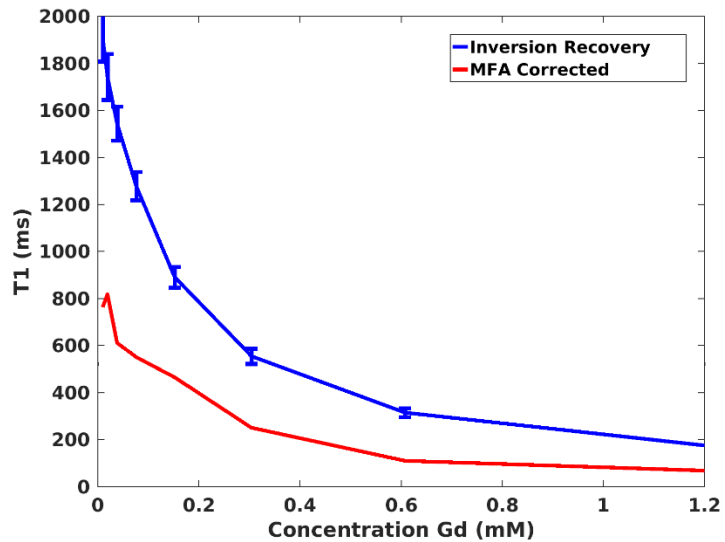
Figure 4-14: T1 measurement using iterative method for simultaneous B1 and slice profile correction.T1 values measured using inversion recovery (±95% confidence interval) compared to multi-flip angle method.
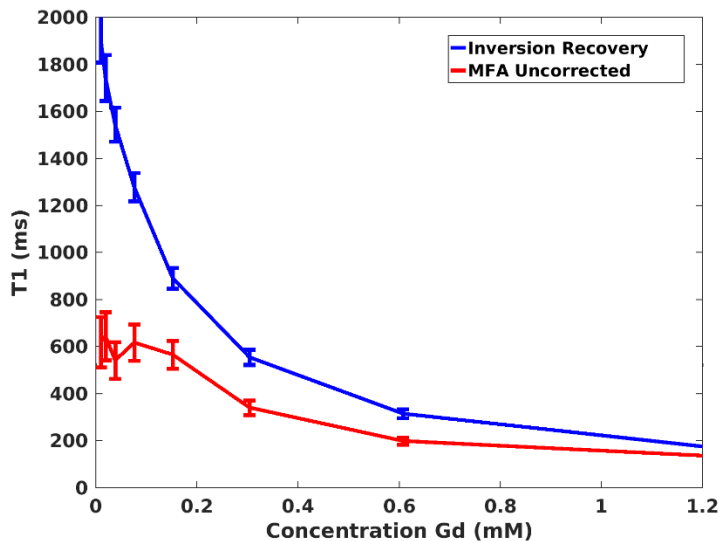
Figure 4-15: T1 measurement without B1 or flip angle correction. T1 values measured using inversion recovery (±95% confidence interval; blue) compared to multi-flip angle method (±95% confidence interval; red).

4.4 Discussion

In this chapter a multi-parametric pulse sequence for thermal therapy monitoring was successfully implemented on a clinical 3T MRI. This sequence is effectively equivalent to the product pulse sequence when the directly compared using the same scan parameters. A scheme for altering the flip angle via scaling the amplitude of the RF pulse was added for dynamic measurement of T1. This addition has no discernable impact on the quantification of T2* or PRF outside of SNR effects observed at low flip angles. Measurements of the temperature sensitivity coefficient are also consistent with expected values.

Quantification of T1 is complicated by several constraints. MFA measurements are effectively restricted to flip angles under 30° due to the practical limitations in the pulse sequence design. The impact of this can be understood by examining Figure 4-5. The Ernst angle is always in between the optimal flip angle pair and remains under 35° over the entire T1/TR range in the figure. The high flip angle rapidly exceeds the 30° limit of the mfamfgre2d sequence. However, Schabel et al.[125] have shown that the precision is relatively insensitive to the value of the higher flip angle

49

compared to low flip angle for TRs in this range. Thus, in the case where 4-2 holds, the limited range

of flip angles is suboptimal but it can be worked around through careful selection of sequence

parameters.

Two factors that have a larger impact on T1 quantification in the mfamfgre2d sequence are

the effects of B1 inhomogeneity and the slice profile. An iterative method that accounts for both

effects simultaneously was tested against gold standard inversion recovery method. The corrected

T1 values remained substantially lower than the true values and showed no discernible

improvement over the uncorrected values (Figure 4-15). It is difficult to isolate where this correction

fails as both effects are convolved with one another. However, Figure 4-13 provides some insight

into the appropriateness of the correction for B1 inhomogeneity. The measurement is clearly biased

at small flip angles but the B1 inhomogeneity at the highest flip angle is still approximately double

the nominal value. Although localized deviations of this magnitude have been measured using the

DAM[135], they are not expected to cover a region that contains the centrifuge tubes . Even if this

measurement is assumed to be accurate it implies that the flip angle far exceeds the 30° limit and

the small flip angle approximation is violated.

Several options exist for rectifying the inability to obtain accurate T1 values. Perhaps the

most straightforward approach is to make similar alterations to 3D spoiled gradient echo sequence.

This would eliminate slice profile effects and allow B1 effects to be isolated. Far shorter TRs would

result in in lower optimal flip angles and certainly justify the small flip angle approximation and the

same amplitude scaling scheme. The primary draw back to using a 3D sequence is the additional

time required to phase encode in the z-direction to prevent aliasing. While this could be mitigated

by using some combination of parallel imaging, view sharing, and saturation bands, the impact on

temporal resolution would need to be carefully considered on a case by case basis. Implementing a

B1 mapping method that is less sensitive to slice profile effects, such as the Bloch-Siegert[130]

technique, would also aid in deconvolving the two sources of uncertainty with reduced scan time. Greater control over the RF pulse shape would also be advantageous as it would allow systematic examination of impact of the slice profile, including pulses that are far closer to the ideal rectangular slice profile. Techniques that use look-up tables are also available[136] but require acquisition of large amounts of data before experiments and rely on the assumption that the B1 field does not change significantly when different objects are scanned.

These results are best viewed in comparison to other studies in the literature examining hyrbrid PRF/T1 technique for temperature monitoring. Hey et al.[50] used a similar approach with a 2D acquisition. The primary difference was the use of high specific bandwidth sinc-Gaussian pulse[137] to obtain a more rectangular profile. The increase in SAR was offset somewhat an EPI readout which is not compatible with the multi echo acquisition. Todd et al.[32,138] used an almost identical sequence where all flip angles were scaled using a calibration factor calculated from inversion recovery experiments. However, their approach was intended primarily to supplement the PRF method in breast adipose tissue. It was successful in this respect but still suffered similar underestimation was in pork muscle due to its longer T1 (≈900 ms). This is consistent with the results presented here of decreasing error with T1.

Chapter 5: Development of a Methodology for Fitting Thermal Dose Models Using Magnetic Resonance Imaging

5.1 Introduction

One of the primary barriers to fitting thermal dose models to clinical ablation data is the underlying mathematics associated with applying the model in the face of a dynamically changing temperature. Equations 3-7 and 3-12 are transcendental and impossible to solve analytically for the case of an arbitrary temperature history. Consequently, thermal dose models have traditionally been derived from laboratory experiments where the temperature is precisely controlled and the integrals can be solved analytically. This requirement is practically impossible to adapt to clinical procedures where spatial and temporal temperature gradients are unavoidable. An additional drawback of dose models based on Arrhenius kinetics is that they predict continuous dose values which are poorly suited for the categorical EOIs that are often observed in the clinic. In this chapter a novel methodology for solving the AR model parameters is proposed and validated. The proposed technique relies on solely MRI to acquire the necessary information on both the temperature and state of tissue. A logistic model is coupled to the AR model to better account for categorical EOI and nonlinear optimization techniques are used to overcome the transcendental nature of the governing equations. The overall methodology is first described in a general sense and subsequently validated in an egg white phantom using intra-treatment and post-treatment changes observed on MRI as EOIs. Egg white was chosen because it is readily available and is known to be predominantly made up of proteins whose kinetics closely match the underlying assumptions of the Arrhenius model. Both models are compared to the Arrhenius parameters in the literature and the region of protein coagulation observed on a post-treatment T1 which acts as surrogate for visible coagulation.

5.2 Methods

5.2.1 Model Definition

The AR model is explicitly chosen for model fitting because it relies on the fewest simplifying assumptions and CEM and CT model parameters can be approximated by the Arrhenius parameters, E_a and A. As mentioned in section 3.3.2 the quantitative nature of the AR model is ideal if the corresponding EOI is quantitative but is problematic for categorical EOIs which need to be arbitrarily assigned a particular value of Ω or FC. Many radiologic isoeffects are categorical so this deficiency needs to be considered in any dose fitting methodology. This is addressed by coupling the traditional Arrhenius model to a second model that predicts the EOI as a function of FC. In this work we consider binary categorical EOIs so a binary logistic model is used. In this case, temperature histories are assigned a binary classification ($y \in \{0,1\}$) that reflects the EOI.

$$\hat{y}(\text{FC}; k_{50}, \text{FC}_{50}) = \frac{1}{1 + \exp(-k_{50}(\text{FC} - \text{FC}_{50}))} \qquad \text{5-1}$$

This coupled model can be interpreted as predicting the probability of observing an binary EOI as a function of thermal dose. Instead of assigning an EOI to an arbitrary thermal dose value an optimal dose threshold can be found that best classifies pixels or represents a probability of interest. Theoretically, this approach can be generalized to arbitrary models depending on the effect of interest (e.g. clustering, multinomial logistic regression etc.)

5.2.2 Arrhenius Parameter Optimization

Optimizing the multi-level model in the previous section is not trivial due to the transcendental nature of the Arrhenius equation. The optimal Arrhenius parameters were defined to be the pair of E_a and A values that maximize the joint log likelihood, $log(\mathcal{L}(E_a, A|y))$, of the logistic model in equation 5-1:

$$log\big(\mathcal{L}(E_a, log(A), |y)\big) = \sum_{i=1}^{N_{pixels}} y_i log(\hat{y}_i) + (1 - y_i)log(1 - \hat{y}_i) \qquad \text{5-2}$$

The Arrhenius parameters are known to be correlated (see section 3.3.2) over a wide range of biological processes which further complicates the fitting of dose models. Regardless of whether this correlation is a consequence of a thermodynamic compensation law or an artefact of the fitting process[139–143], it restricts the possible parameter pairs in the $E_a/log(A)$ parameter space to a line within some experimental tolerance. A reparametrized expression for the reaction rate, k, was used during the optimizations:

$$k = \exp\left(log(A_{Ref}) - \frac{E_A}{R}\left(\frac{1}{T} - \frac{1}{T_{Ref}}\right) \right) \qquad \text{5-3}$$

where

$$log(A_{Ref}) \equiv log(A) - \frac{E_A}{RT_{Ref}} \qquad \text{5-4}$$

and T_{Ref} was chosen to be equal to 316.5°K to remove the correlation in equation 3-10. This new $E_a/log(A_{Ref})$ parameter space effectively focuses the parameter search on values near the line in equation3-10 while facilitating the convergence of the optimization algorithm and aiding in visualizing the solution[144,145]. This method of optimization is analogous to the method of Qin et al. [108] with a different objective function and no explicit constraints on the parameter values. The optimizations were solved using a Quasi-Newton BFGS algorithm (fminunc, MATALB, Mathworks, Natick, MA) with the Arrhenius parameters reported by Henriques[97] as the initial guess. The approximate Hessian at the solution was inverted to estimate the covariance matrix and generate confidence ellipses for the parameter values. The solutions and covariance matrices were then transformed into the traditional $E_a/log(A)$ parameter space for comparison with parameters found in the literature.

5.2.3 Egg White Phantom Preparation and Laser Exposure

Egg white phantoms were created using a mixture of 50% egg white (Crystal Farms,

Minnetonka, MN) and 50% deionized water by volume mixed with 1.5% agarose (weight/volume)

(A0169, Sigma-Aldrich, St. Louis MO) and Gadolinium based contrast agent (0.06mM-0.21mM;

Omniscan, GE Healthcare, Waukesha, WI). Thermal lesions (N=17) were created using a water-

cooled diffusing tip laser fiber (VCLAS-400-12-T10-11, Medtronic Navigation; Louisville, Colorado)

attached to a 980nm diode laser (Photex15, Biotex, Houston, Texas). The applied power and time

was varied from 7-15W for 3-13 minutes with the intention of maximizing lesion size, preventing

melting of the agarose, and sampling a variety of temperature histories. The temperature was

independently measured within a few cm of the diffusing fiber tip using a fluoroptic temperature

probe (m3300/STB, Lumasense, Santa Clara CA).

Multi-parametric monitoring was performed using the mfamfgre2d sequence (FOV=19.2 x

19.2 - 19.6 x 19.6 cm, 128x128 acquisition matrix, TR= 35-100 ms, 8 echoes, TE_{min}=1.8-2.1 ms,

ESP=2.1-1.8 ms, RBW=195-326 Hz/pixel, slice thickness=3mm, α=25-30°C, mfa_mode=0/1,

mfa_low_flip=2, number of slices=1-3, time between images=4.8-12.4s) on a clinical 3T MRI scanner

(Discovery 750; GE Healthcare Technologies; Waukesha, WI). All slices placed along the long axis of

the laser fiber (coronal). Temperature was calculated using the PRF estimates provided by the ARMA

model and a temperature sensitivity coefficient of -0.01ppm/°C while the apparent temperature

increase caused by drift in the main magnetic field was accounted for by placing an ROI far away

from heating or in an attached centrifuge tube filled with vegetable oil.

After each laser exposure a T1 map was acquired using a multi inversion time fast spin echo.

((FOV=19.2 x 19.2 - 19.6 x 19.6 cm, 256x256 acquisition matrix, TR= 4000 ms, Echo train length=4,

TE=8.3, RBW=244 Hz/pixel kHz, slice thickness=5mm, inversion times(TIs)=100-1200 ms)). A semi-

automatic segmentation procedure was performed to determine the extent of the coagulated area

on post-treatment imaging. Heavily filtered (wiener filter; 10x10 kernel) T1 maps were subtracted from lightly filtered images (wiener filter; 3x3 kernel) to represent the increase in T1 compared to background. These maps were thresholded at 10% of the maximum value and used as a starting point for manual segmentation of the coagulated area. Manual segmentation was necessary primarily to account for artifacts caused by the presence of the laser fiber. After the experiments the phantoms were sliced along the axis of the laser fiber to best approximate the MR slice position and the size of the coagulated area was measured in two dimensions using a ruler.

The exposures are divided into three groups based on differences in scan parameters and how they were used during post-processing. The alternating flip angle scheme was used for the first three exposures (group A) but was abandoned in in favor of increased SNR and temporal resolution when it was observed that the T1-W signal was a sufficient surrogate for identifying an intra-treatment EOI. The group A exposures and the subsequent 8 exposures (group B) were determined to have experienced significant melting over the course of heating. This manifests as a large scale susceptibility artifact that corrupts temperature imaging in the region of interest. For this reason the thermal exposure cannot be directly compared to post-treatment imaging. However, the intra-treatment EOIs were observed at approximately 60°C so these temperature histories were reserved for training the intra-treatment models. The final group (group C) was intended to serve as a validation cohort for the intra-treatment model trained on groups A and B. T1-Weighting was less critical in this group so the number of slices was increased at the expense of longer TR. The specific variations between scan parameters and power for each exposure is tabulated in Appendix 1 for reference.

5.2.4 Intra-Treatment Arrhenius Models

Arrhenius models were investigated for intra-treatment EOIs based the T1-W signal and T2* measured during each exposure. Both parameters exhibited temperature dependence that changed

abruptly at one or more breakpoints (i.e. the second derivative became nonzero). In both cases, the

models were trained on breakpoints closest to 60°C that are consistent with those observed in *ex*

vivo studies.[44,14643]. For each exposure, all pixels whose temperature exceeded 65°C were isolated

for analysis. The signals were observed to be approximately linear on either side of the breakpoint

and a temperatures were only considered in the range from 40°C-80°C to minimize the contribution

of other nonlinearities not associated with the EOI. The T1-W signal was normalized to its

preheating value and a constrained piecewise linear fit was used to identify this breakpoint on a

pixel by pixel basis (fmincon, MATLAB, MathWorks, Natick MA).

This 4 parameter fit is given by:

$$\underset{C_1,C_2,C_3,BP}{arg\ min}\ \|C_1 + C_2T + C_3(T - BP)sgn(BP) - S(T)\|_2$$
$$s.t.\ C_1 \in [0,2]$$
$$s.t.\ C_2 \in [-\infty, 0]$$
$$s.t.\ C_3 \in [-\infty, 0]$$
$$s.t.\ BP \in \left[\min(T), \max(T)\right]$$

5-5

where C_{1-3} are constants, BP is the breakpoint, T is the temperature, and $S(T)$ is the

relative change in the T1-W signal magnitude. A representative example of this fit is shown in figure

5-4.
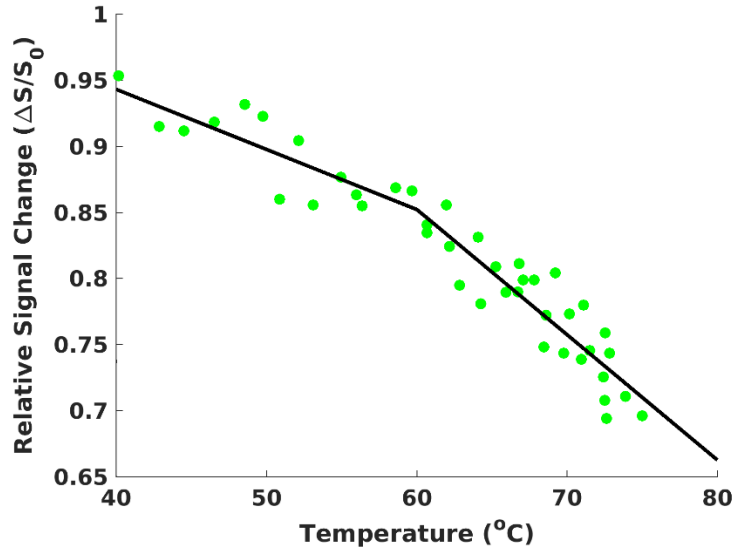
Figure 5-1: Representative example of piecewise linear fit used to for the intra-treatment Arrhenius model. The breakpoint where the temperature dependence of the normalized T1-W signal changes abruptly is used to classify temperature histories according to equation 5-8.

A similar approach was used for finding the breakpoints in T2*. However, visual inspection of the data showed the behavior of the T2* temperature dependence was not as consistent as the T1-W signal. For example, the magnitude of the slope of the temperature dependence varied from positive to negative between pixels which required modification of the optimization constraints:

$$\underset{C_1, C_2, C_3, BP}{arg\ min}\ \|C_1 + C_2 T + C_3 (T - BP)sgn(BP) - T2^*(T)\|_2$$

$$s.t.\ C_1 \in [0,2]$$
$$s.t.\ C_2 \in [-\infty, 0] \qquad \text{5-6}$$
$$s.t.\ C_3 \in [-\infty, 0]$$
$$s.t.\ BP \in \left[\min(T), \max(T)\right]$$

Where $T2^*(T)$ is the measured T2* as a function of temperature. Breakpoints were also not consistently observed in every pixel. To exclude these data from analysis in an automated manner the Akaike information criterion (AIC)[147] was calculated for each piecewise linear fit. For a least squares model the AIC is defined as:

$$AIC = 2k + N log(RSS) \qquad \text{5-7}$$

58

Where k is the number of model parameters, N is the number of data points, and RSS is the residual sum of squares. This AIC is a measure of the quality of a model that penalizes for the number of model parameters to prevent overfitting. Data were excluded if the AIC values from the piecewise linear fit were larger than the values calculated for a traditional linear least squares fit. Examples of a temperature history that were included and excluded not excluded using the AIC criteria are shown in Figure 5-2. This rejection criteria was also applied to the intra-treatment model based on T1-w signal.

Once the breakpoints were determined they were used to make two binary classifications:

$$T(BP - 2.5°\text{C}) \rightarrow y = 0$$
$$T(BP + 2.5°\text{C}) \rightarrow y = 1$$

5-8

Where the 2.5°C is added to account for uncertainty in the breakpoint and the temperature imaging. This is particularly important at low heating rates where the precise time the breakpoint was reached is not known with high precision. After applying AIC rejection criteria both models were fit using the optimization scheme outlined in section 5.2.1.
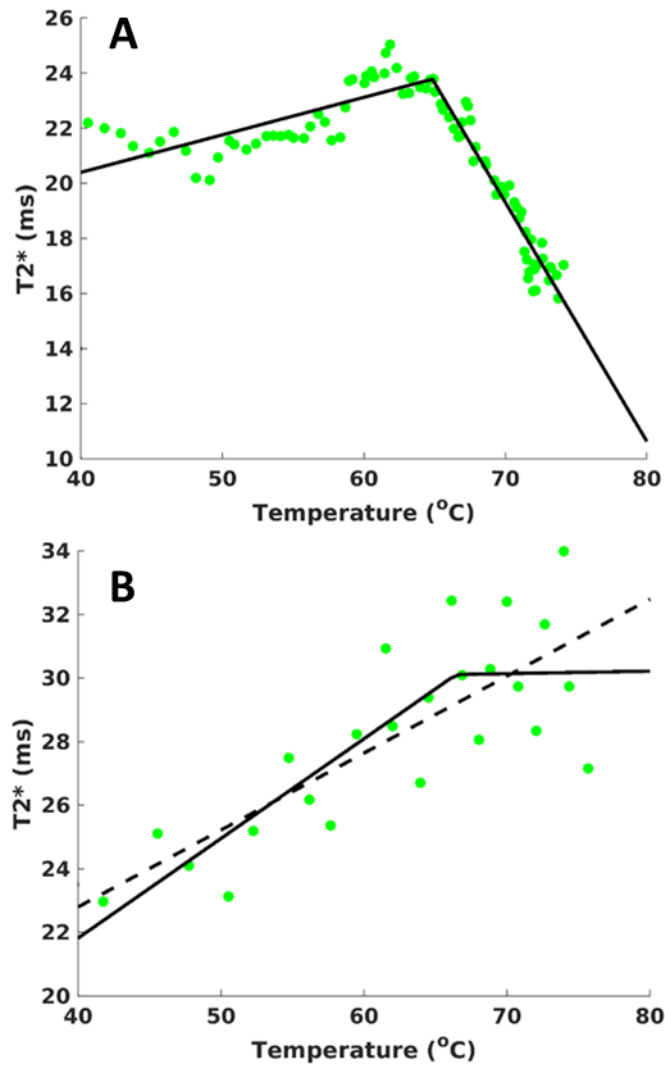
Figure 5-2: Example of breakpoint determination for the T2* intra-treatment Arrhenius model. The existence of a breakpoint was determined by comparing AIC values between the piecewise linear fit (solid) and a traditional linear fit (dotted). A break point was observed in A but not B.

5.2.5 Post-Treatment Arrhenius Model

A third model was trained using post-treatment increases in T1 as a post-treatment

isoeffect. Temperature histories associated with increases in T1 using the method described in in

section 5.2.3 were assigned values of $y = 1$. This region was dilated using a 5x5 kernel (≈5mm). Any

unassigned pixels within this larger region were assigned values of $y = 0$. A representative example

of these ROIS is shown in Figure 5-3. This model was only trained using exposures in group C only

due to the previously measured susceptibility artifacts. (Total number of pixels = 3,956)
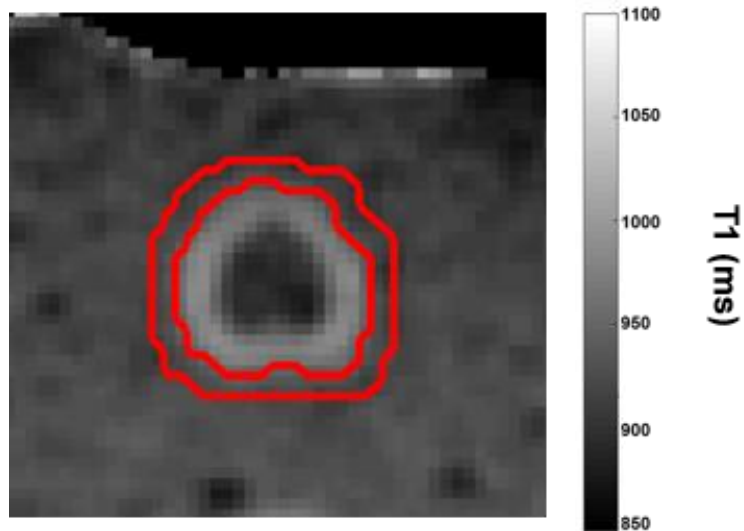
Figure 5-3: ROIs used for post-treatment model. The inner region represents the region of T1 increase (y=1) while the surrounding region represents pixels that were exposed to elevated temperatures without any T1 increase (y=0).

5.2.6 Model Comparisons

The Arrhenius parameters were directly compared to values found in the literature for

protein denaturation measured using dynamic scanning calorimetry (DSC) and turbidity measured

using spectrophotometer. References were restricted to those examine whole egg white[148,149] rather

than isolated constituent proteins, such as ovalbumin[150,151]. Unfortunately, independent

measurements of the frequency factor are not available and they had to be estimated using 3-10.

Effect of Interest (EOI)	Log Frequency Factor, $\log(A)$	Activation Energy, E_A [kJ/mol]	Note
Denaturation[148,149]	157	439	pH 7.6[149]
	136	383	pH 8.8[149]
	135	380	pH 7.6[148]
Turbidity[148,149]	87	254	pH 7.6[149]
	85	248	pH 7.6[148]
*Estimated using equation 3-10			

Table 3: Selected literature values for egg white

The model predicted regions, A_{model}, were calculated for each ablation and compared to the segmented regions, A_{seg}, found on post-treatment T1 mapping to get a practical measure of the goodness of fit using three methods of comparison. The first is the Dice Similarity Coefficient (DSC):

$$DSC = \frac{2|A_{model} \cap A_{seg.}|}{|A_{model}| + |A_{seg.}|}$$

5-9

The DSC is a measure of the spatial overlap of two regions where a value of 1 corresponds to complete overlap and a value of 0 corresponds to no overlap. While the DSC is commonly used in radiology research, its value is biased by the center of the lesion which is virtually guaranteed to match assuming the areas are properly registered. For this reason, two additional quantities of interest based on the distances between the model and segmentation boundaries were used. In general, for two boundaries defined as sets of Cartesian coordinates, $A = \{a_1 \dots a_n\}$ and $B = \{b_1 \dots b_m\}$, the quantity $d(A, B)$:

$$d(A, B) = \min_{b \in B}\{\|a - b\|_2\}$$

5-10

represents the minimum Euclidean distance from between every point on boundary A and any point on boundary B. Note that $d(A, B)$ is not communitive ($d(A, B) \neq d(B, A)$). Model and segmentation boundaries were compared using the Hausdorff Distance (HD):

$$HD(A, B) = \max\left\{\max_{a \in A} d(A, B), \max_{b \in B}\{d(B, A)\}\right\} \qquad \text{5-11}$$

Which is the maximum value of d found in $d(A, B)$ and $d(B, A)$. This is a common measure of agreement between two sets because it is a metric in the formal sense and can be interpreted as the worst case disagreement between the two contours. However, as a maximum value it is inherently sensitive to noise and outliers. For this reason the average difference between the boundaries or mean distance to agreement (MDA):

$$MDA(A, B) = \frac{\sum_{i=1}^{n} d(A, B) + \sum_{i=1}^{m} d(B, A)}{m + n} \qquad \text{5-12}$$

was also used to compare the radiologic feature models to the inner and outer boundary segmentations. Taken together these three methods give a more complete picture of model performance. The value of each of these metrics was averaged over the 3 slices for each exposure in group C and are given in Table 6 and Table 7.

5.3 Results

Each exposure resulted in a coagulated regions that could be identified visually and on T1-weighted imaging. The upper limit on lesion size while preventing melting in the agarose gel was approximately 1.1 cm. Excellent agreement was observed between the lesions measured visually and the regions segmented on post-treatment imaging in group C. The maximum difference was 1 mm which is small considering the uncertainties associated with precisely cutting the phantom, partial voluming, and the pixel size of 0.75mm. Thus, the post-treatment changes in T1 were considered surrogates for visible coagulation when evaluating the fitted models.

The post-treatment and intra-treatment T1 models converged to unique solutions that are plotted in the $log(A_{Ref})/E_A$ parameter space in Figure 5-4a-b. Both solutions are plotted together in the traditional $log(A)/E_A$ reference space in Figure 5-4c. The advantage of the reparameterization in equations 5-3 with respect to visualizing the solutions are obvious by comparing these two figures. The activation energies associated with the 95% confidence intervals ranged from 342-470 kJ/mol and 257-344 kJ/mol for the intra-treatment and post-treatment models, respectively. Although the solutions are close to one another and the objective function surfaces are similar, their confidence ellipses do not overlap. However, they do cover the range of activation energies found in the literature. The complete set of parameters that define these confidence intervals along with R_{CEM} and T_C' calculated using equations 3-13 and 3-16 are found in Table 4. The intra-treatment model using T2* as an EOI did not converge to a unique solution within the range of physically realistic values (Figure 5-2). Significantly more pixels were rejected for this EOI (29%) compared to the T1-W intra-treatment EOI (6%).
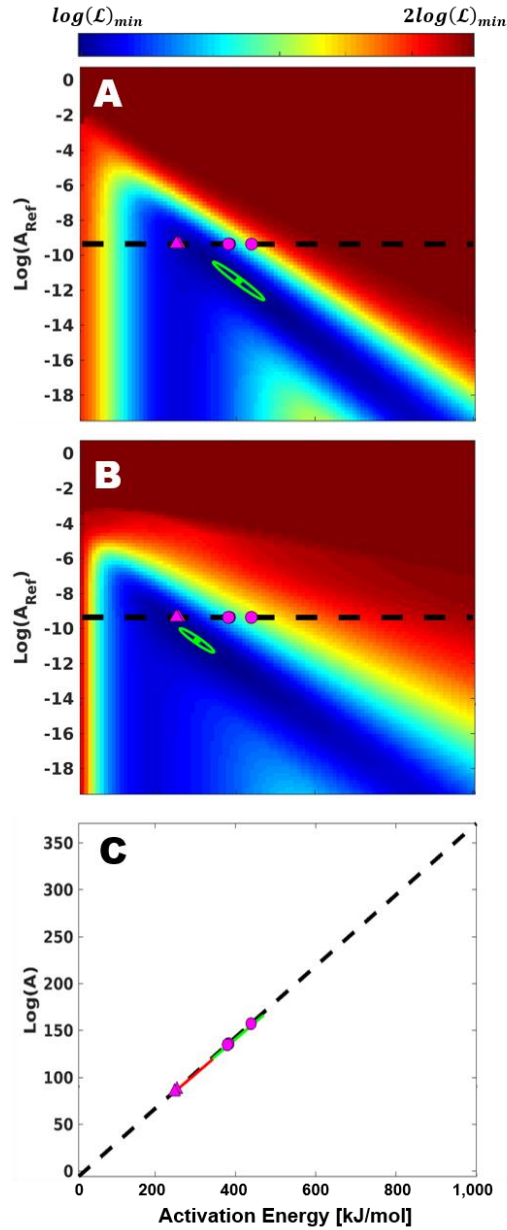
Figure 5-4: Optimal Arrhenius parameters for the intra- and post-treatment models (T1-W signal and ΔT1). The optimal Arrhenius parameters (green circle) and 95% confidence regions (green) are shown with the negative log likelihood in the background in the $log(A_{Ref})/E_A$ parameter space for the intra treatment (A) and post-treatment dose (B) models. The same data is shown in the $log(A)/E_A$ parameter space (C) where the intra-treatment model is plotted in green and the intra-treatment model is plotted in red. Selected Arrhenius parameters from the literature (magenta) for egg white are plotted using denaturation (●) and turbidity (▲) as EOIs.

	Intra-treatment (T1-w)	Post-treatment (T1)
Activation Energy, E_A [kJ/mol]	405	301
Log Frequency Factor, $\log(A)$ [s^{-1}]	142	103
Minor axis length	0.225	0.197
Major axis length	68.1	45.9
Slope [kJ^{-1}]	0.364	0.365
Intercept	-4.71	-6.15
R_{CEM}	0.62	0.70
$T_C{'}$ [°C]	68	74

Table 4: Optimal Model Parameters and 95% Confidence Ellipse for intra-treatment and post-treatment models.
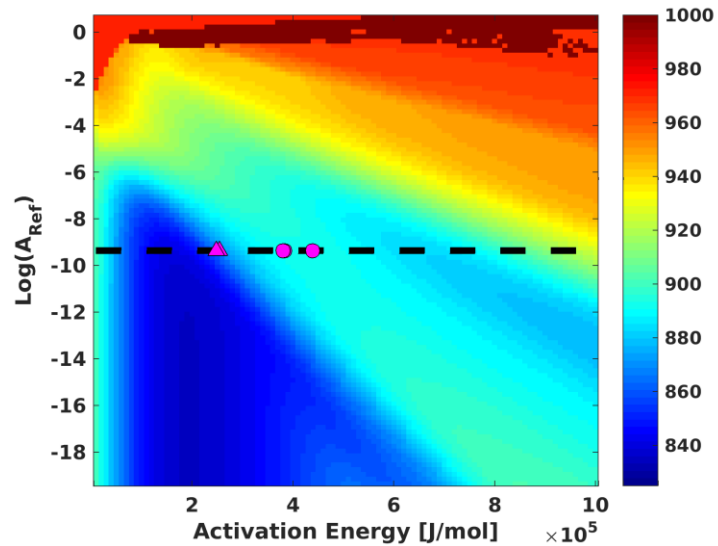
Figure 5-5: Objective function surface for intra-treatment T2* model. The optimization does not converge to a solution. Selected Arrhenius parameters from the literature (magenta) for egg white are plotted using denaturation (●) and turbidity (▲) as EOIs.

The optimal dose thresholds were found to be $FC = 0.53$ and $FC = 0.40$ for the intra-

treatment and post-treatment model, respectively (Table 5). Plots of these optimal dose thresholds

are shown in Figure 5-6 along with the false positive and true negative rates for reference. The area

under curve (AUC) and accuracy were 0.92/88% and 0.93/86% and for the intra-treatment and post-

treatment model, respectively. The model predicted regions were compared with the segmented

regions for each exposure in group C and a representative example of the contours is shown in

Figure 5-7. Qualitative comparison shows good agreement between the model predicted and

segmented regions and very little difference between the two dose models. This is confirmed using

the three metrics with DSC/HD/MDA of 0.82/2.84 mm/0.98 mm and 0.83/2.72 mm/0.92 mm for the

intra-treatment and post-treatment isoeffects, respectively. (Table 6 and Table 7)

	Intra-Treatment	Post-Treatment
k	6.35	7.1
FC_{50}	0.53	0.40
AR Model Thresholds ($\hat{y}/FC/\Omega$)	0.53/0.54/0.78	0.45/0.40/0.51

Table 5: Optimal dose thresholds for intra-treatment and post-treatment isoeffect
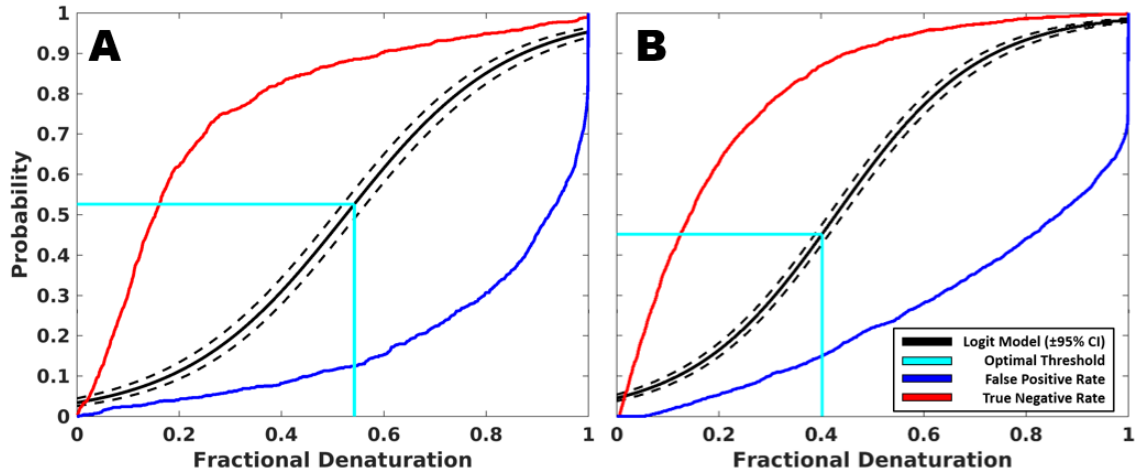
Figure 5-6: Logistic model results for intra- and post-treatment models. The logistic model prediction (black solid) ± 95% confidence intervals (black dotted) for the intra-(A) and post-treatment(B) dose models with false positive rate (blue) and true negative rate (red). The thresholds that optimize the accuracy are shown cyan.
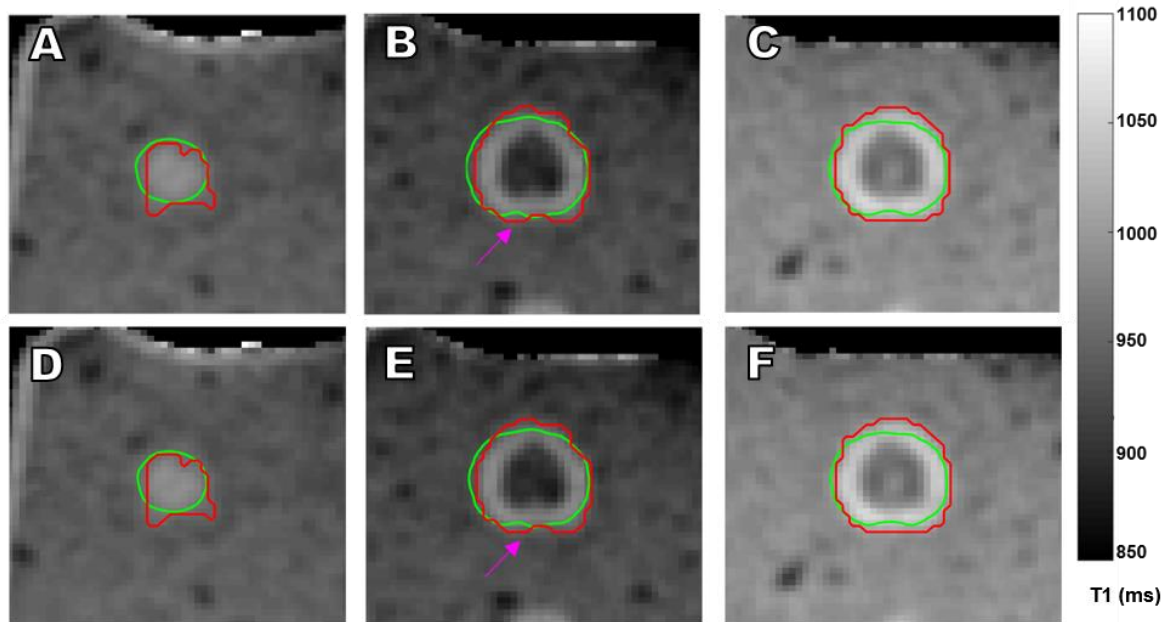
Figure 5-7: Comparison between segmented regions and predicted dose for intra-treatment and post-treatment models. The segmented regions (red) and the predicted dose (green) are shown for all three slices the intra-treatment (A-C) and post-treatment models (D-F). Magenta arrows identify subtle differences between the predicted dose contours from each model.

Exposure #	DSC	HD (mm)	MDA (mm)
1	0.86	2.71	0.98
2	0.77	2.17	0.87
3	0.88	2.69	0.79
4	0.78	2.54	1.04
5	0.82	2.78	0.91
6	0.86	3.35	0.87
Mean	0.83	2.71	0.91

Table 6: DSC, HD, and MDA between the segmented regions and predicted dose for the intra-treatment model.

Exposure #	DSC	HD (mm)	MDA (mm)
1	0.86	2.69	0.97
2	0.77	2.16	0.88
3	0.89	2.72	0.77
4	0.77	2.84	1.16
5	0.85	2.54	0.81
6	0.86	3.41	0.91
Mean	0.83	2.72	0.92

Table 7: DSC, HD, and MDA between the segmented regions and predicted dose for the post-treatment model.

5.4 Discussion

In this aim a novel methodology for fitting thermal dose models using MR data was proposed and validated in phantoms. A logistic model was coupled to the traditional Arrhenius equation to better account for the categorical EOIs commonly experienced in radiology. This multi-level model was reparametrized to facilitate the use of nonlinear optimization algorithms for finding the Arrhenius parameters. The proposed technique theoretically confers several advantages over traditional approaches to thermal dose modeling. First, the nonlinear optimization techniques makes clinical and experimental ablation data available for model training. This better aligns the derived model parameters with their intended application. Second, the addition of the logistic model provides an additional mapping from thermal dose to the observed effect. This effectively loosens the assumptions between the effect of interest and the underlying assumption of the Arrhenius kinetics which may not be appropriate for all EOIs (including continuous EOIs). This model

is not restricted to a logistic model and can be substituted for any model that's tailored to particular EOI provided that a corresponding likelihood function can be derived for optimization.

This new model fitting technique was validated in an egg-white phantom using both intra-treatment (change in T1-W signal temperature dependence) and post-treatment EOIs (change in T1). These models converged to solutions that are consistent with the range of values obtained by van de Plancken et al.[148,149] for two different EOIs (denaturation and turbidity). While the similarity in the objective function surfaces suggest that the underlying processes are closely related, the confidence intervals of these solutions do not overlap.

The areas predicted by both dose models compare favorably with the areas segmented on post-treatment imaging when measured using DSC, HD, and MDA. In both cases DSC values exceeded 0.8, which is considered good agreement in the context of radiology.[115,152] The HD measurements showed disagreement of 2-3mm (2-4 pixels) that can be primarily attributed to artifacts caused by the presence of the laser. The mean distance to agreement was under 1mm for both models which is small compared to the pixel size of 0.75mm. Each of the area comparison metrics performed slightly better for the post-treatment model compared to the intra-treatment model. This can be ascribed to the fact that the post-treatment model was trained to the same EOIs and exposures that was used for evaluation whereas the intra-treatment model was trained to a different (but related) EOI in a separate training group of exposures. However, the differences (ΔDSC=0.01/ΔHD=0.08 mm/ΔMDA=0.06 mm) are so small that the model predicted areas can be considered equivalent for practical purposes.

A third model that used changes in T2* as an intra-treatment isoeffect failed to converge to a solution. Variations within this data prevented breakpoints from being identified consistently. The temperature dependence of this data was inconsistent and a breakpoint could not be identified in all pixels. Ultimately, 29% of the pixels were rejected using the AIC to prevent overfitting. This result

suggests that changes in T2* are not a reliable indicators of Arrhenius processes in this phantom setup. In contrast, Taylor et al.[44] found opposite results regarding the utility of T1-W imaging and T2* in *ex vivo* tissue. Further research is needed to evaluate the applicability of this parameter in other samples.

While the experiments in this aim are sufficient for establishing the feasibility of the proposed technique there are several areas where improvements can be made in future experiments to enable additional characterization. One limitation of the phantom design was the effect of melting agarose on MRTI measurements. This limited the number of exposures that could be used for training the post-treatment model and effectively reduced the available lesion sizes. Melting was also problematic when investigating other imaging effects such as magnetization transfer (MT) and transverse relaxation (T2/T2*) rates since reliable changes in these parameters were only observed at higher temperatures. This could be remedied by using higher melting point agarose or switching to another MR visible gel with a higher melting point. Another alteration to the experimental procedure would be to use isolated proteins for the measurements. Egg white is a mixture of several proteins that denature with different kinetics. This would allow independent verification in variety of different proteins while removing the uncertainty associated with having mixed effects from multiple proteins.

Chapter 6: Application of Thermal Dose Models *in vivo*

6.1 Introduction

Post-treatment MRI, usually in the form of contrast-enhanced imaging, is often employed immediately following thermal ablation therapies as the primary method of assessing the extent of the thermal damage to tissue. These post-treatment images serve as a baseline for follow-up imaging and are critical for monitoring for local progression.[10,74] The availability of magnetic resonance compatible delivery devices and the ability to monitor these therapies using real-time MR temperature imaging has led to rapid adoption of these therapies in sensitive anatomic sites such as the central nervous system. [153–157] Temperature feedback coupled with appropriate thermal dose models facilitates periprocedural adjustments to maximize target coverage and reduce damage to critical structures. [8,113] Together, treatment monitoring and post-treatment verification imaging help provide a more complete assessment of the extent of therapy delivery.

Despite the outsized role radiologic appearance plays in treatment evaluation, existing thermal dose models are not designed to be predictive of the radiologic changes that are ultimately used for treatment assessment. Instead they rely on empirically derived parameters from laboratory experiments that only approximate clinical endpoints[8,97,102,113] or simplified models that may only be applicable to a small subset of treatments[158]. Rather than deriving novel model parameters, previous research in preclinical and clinical dose modelling has focused almost exclusively on correlating dose estimates using existing models with radiologic observations for a narrow set of procedures [114,118–120,159]. This can be directly attributed to the mathematics that underlie the effects of heat on tissue. However, as the frequency and types of MR-guided ablation procedures increases there is a growing need and opportunity for developing methodologies that leverage existing clinical

data to investigate novel dose models that are tailored to an expanding number of available radiologic endpoints.[160]

In this work we develop and investigate a method for fitting novel thermal dose models using intra-operative MR imaging during laser ablation of brain metastases in human subjects. The high temporal and spatial resolution of MRTI is combined with nonlinear optimization techniques and logistic modeling to overcome the challenges that have traditionally restricted these types of studies to the laboratory. To demonstrate the feasibility of developing models in this manner, two models are investigated that predict the size of the non-enhancing central region and enhancing ring that are characteristic of thermal lesion on post-treatment contrast-enhanced T1-weighted imaging. A third model is examined that seeks to interpret these regions in terms of probability of tissue viability. These parameters are compared to several other models that have been investigated for use during thermal ablation therapies. The predicted areas are then compared to the areas segmented on post-treatment imaging and the areas predicted by two clinically used dose models.

6.2 Methods

6.2.1 Lesion Selection and Image Processing

Intra operative MR temperature imaging estimates and post-treatment contrast-enhanced imaging were retrospectively analyzed for 5 intracranial metastatic lesions (2 melanoma/3 breast; 2 male/3 female; age range: 57-69) treated using a 15W 980nm laser with a single, water cooled laser applicator (Visualase, Medtronic, Minneapolis, MN, USA) on a 1.5T MRI (MAGNETOM Espree, Siemens Healthcare, Erlangen, Germany). MRTI was acquired in two orthogonal planes using a dynamic, radiofrequency spoiled gradient echo pulse sequence (TR=24 ms, TE=15 ms, α=30°, acquisition matrix=256x128 , field of view= 26 x 26 cm, slice thickness=3 mm, RBW = 80 Hz/pixel, time between phases=6s) and temperature estimates were calculated by applying the complex

phase difference technique to Wiener filtered complex data (3x3 kernel) in MATLAB (R2015a, MathWorks, Natick, MA, USA) using a temperature sensitivity coefficient of -0.01ppm/°C[27]. To account for drift in the main magnetic field, the apparent temperature increase in a 15x15 pixel ROI in a region far from heating was subtracted from the temperature maps. In cases where transient shifts in the magnetic field were observed, temperature maps were linearly interpolated in the temporal direction and a new baseline image was selected. Lesions treated with multiple fibers or containing major MRTI artefacts were excluded to ensure the accuracy of the MRTI data.

Each lesion was imaged before and after treatment using a 3D T1-weighted spoiled gradient echo sequence with and without contrast (TR=5.25 ms, TE=2.5 ms, α=15°, acquisition matrix=256x256, field of view= 28 x 28 cm, slice thickness=1.25 mm, RBW= 400 Hz/pixel). The 3D series that preceded the MRTI acquisition was identified as the target series for 3D image registration and distortion correction was kept consistent across all series.

Each 3D series was converted from DICOM file format to the Neuroimaging Informatics Technology Initiative (NIfTi) format[161] and skull stripped[162]to facilitate image registration. An affine registration[161] was used to register each series to the target series and accuracy was assessed qualitatively by verifying the position of the laser fibers.

The region of contrast enhancement was segmented manually (Amira 5.4.2, FEI, Hillsboro, OR, USA) using pre-treatment subtraction images to delineate the gross tumor volume. On post-treatment subtraction images, the non-enhancing central region and enhancing ring were segmented to define the thermal ablation lesion. The registered T1-weighted images and segmentations were then resampled[161] into the 2D geometry of the MRTI acquisition so that temperature histories could be linked to the segmentation data on a per pixel basis. After resampling, the outer edge of the enhancing ring was dilated using a 5x5 kernel (≈5mm) to define an outer non-enhancing region where there was temperature increase but no radiologic change.

6.2.2 Inner/Outer Boundary Models

For post-treatment contrast-enhanced imaging the radiologic features of interest are the boundaries between the central nonenhancing region and the enhancing ring (inner boundary) and the enhancing ring and the outer nonenhancing region (outer boundary). A model for the inner ring boundary was created by assigning all pixels in the central nonenhancing region $y = 1$ and all pixels in the enhancing ring and outer nonenhancing region $y = 0$. Similarly, a model of the outer ring boundary was created by assigning all pixels in the central nonenhancing region and enhancing ring $y = 1$ and those in the outer nonenhancing region $y = 0$. Pixels that enhanced on both pre and post-treatment subtraction images were excluded from the outer boundary model since it is ambiguous whether their enhancement is due to treatment effect or residual tumor. Data in these regions would be inappropriate for training our model as the logistic regression demands we know the fraction of damaged tissue and no assumptions can be made in these areas.

Figure 6-1: Tumor/thermal lesion segmentations and model regions for boundary models. The segmented tumor (blue) and the thermal lesion defined by the central nonenhancing region (red dotted) and enhancing ring (red solid) with skull-stripped post-treatment post-contrast image in the background (A). The regions classified as y=1 (yellow) and y=0 (cyan) for the inner boundary (B), outer boundary (C), models with skull-stripped post-treatment post-contrast image in the background. The area adjacent to the skull has been excluded due to uncertainty in the segmentation and the area of ambiguous enhancement was excluded in the outer boundary model (C).

Temperature histories for each patient were grouped together to generate a patient averaged model of the inner/outer boundaries with optimal dose thresholds chosen to minimize the sum of false positives and false negatives. The inner and outer boundary models were fit using 4,676

and 4,337 pixels, respectively. The Arrhenius parameters of both of these models were compared to 7 values from the literature.

In the special case of the CEM model, equations 3-10 and 3-13 were used to calculate the Arrhenius parameters for the CEM model parameters at high temperatures ($T_0 = 43°C; \mathrm{R}_{CEM} = 0.5$) to reflect the effective parameters used in the literature. A summary of each model and its corresponding EOIs are shown in Table 8. The inner and outer boundary Arrhenius parameters were also used to calculate the equivalent R_{CEM} and $T_c{'}$ using equations 3-13 and 3-16 respectively. Optimal dose thresholds were also calculated using the traditional CEM model (CEM_{thresh}) and the maximum temperature (T_c) for direct comparison to previous work in the literature.

The radiological feature models were compared to the segmentations using the DSC, HD, and MDA metrics described in 5.2.4. After comparing the radiologic features models to the segmented regions they were compared to the two dose models used in FDA cleared systems to get an understanding of the impact of the new models in a clinical scenario. Dose thresholds of Ω=1[113] and CEM=2, 10, 60, and 240 minutes at 43°C[8] were used for the Henriques model and CEM model, respectively.

Study	Log Frequency Factor, $\log(A)$	Activation Energy, E_A [kJ/mol]	Effect of Interest (EOI)
Henriques†[97]	227	628	Second degree burns; porcine skin (*in vivo*)
CEM*†[102]	210	578	Various (*in vivo/ex vivo*) [163]
Qin [108]	64.2	189	Protein denaturation; whole cells; DSC with $T_{max} = 60°C$
Qin [108]	145	401	Protein denaturation; whole cells; DSC with $T_{max} = 50°C$
Jacques‡ [103]	87.2	258	Optical scattering coefficient; porcine liver (*ex vivo*)
Borelli‡ [104]	185	506	Cell survival; baby hamster kidney cells
Brown‡ [105]	245	667	Microvasculature disruption; murine muscle (*in vivo*)

†Used in FDA cleared ablation system

*Calculated assuming R=0.5 and equations 3-10 and 3-13

‡Associated with inner/outer ring boundaries on T2-weighted imaging by Sherar et al. [114]

Table 8: Selected Arrhenius parameters from literature.

6.2.3 Tissue Viability Model

The primary limitation of the radiologic feature models is that they provide no direct information on the viability of the tissue. Real-time prediction of the inner and outer ring boundaries still requires interpretation of a physician when making treatment decisions. Several studies have examined the viability of tissue in each of the segmented regions and there is

considerable ambiguity in the fate of tissue in the enhancing ring.[81,81,83,84,86,87,119] However, if pixels in

the central nonenhancing region are assumed irreversibly damaged ($y = 1$) and pixels in the outer

nonenhancing region are assumed to viable ($y = 0$) the resulting model can be interpreted as a

model of tissue viability. (Figure 6-2) This a subtle but significant difference from the inner/outer

boundary models where the objective was to find a threshold that best classifies pixels as being on

either side of a boundary. Here thresholds are chosen *a priori* that represent the amount of isoeffect

of practical clinical interest.

Similar to the inner/outer ring boundary models, a patient averaged model was calculated

using data from all patients. A series of tissue viability thresholds (10%, 50%, and 90%) were

examined that represent different degrees of confidence in tissue viability. These can be interpreted

as the thresholds for onset of irreversible damage, equal likelihood of viability and nonviability, and

almost certain tissue nonviability, respectively. Since no radiologic gold standard measure of tissue

viability exists, the areas predicted by the cell viability model were compared to the two clinical

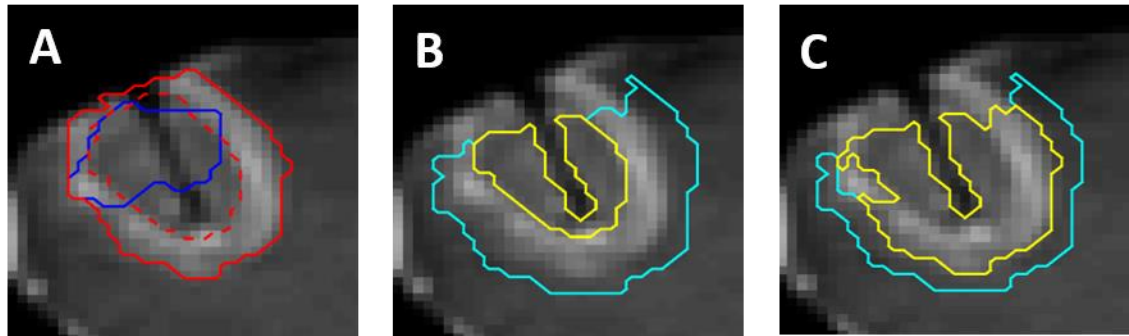utilized dose models using the DSC, MDA, and HD.
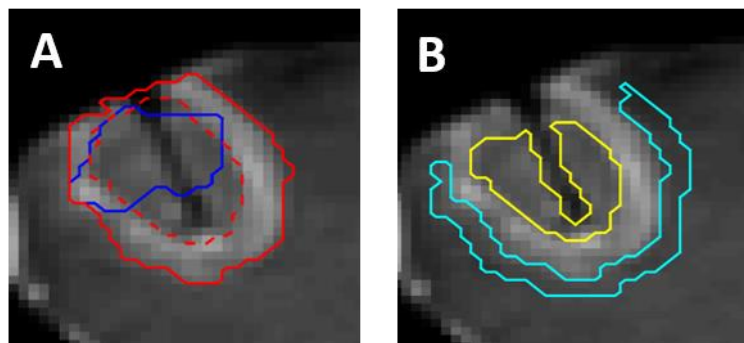
Figure 6-2: Tumor/thermal lesion segmentations and model regions for tissue viability model. The segmented tumor (blue) and the thermal lesion defined by the central nonenhancing region (red dotted) and enhancing ring (red solid) with skull-stripped post-treatment post-contrast image in the background (A). The regions classified as nonviable (y=1; yellow) and viable (y=0; cyan) for the tissue viability (B) model with skull-stripped post-treatment post-contrast image in the background. Pixels in the enhancing ring are interpreted as nonviable while

6.3 Results

6.3.1 Arrhenius Parameter Optimization

To evaluate the convergence of the optimization algorithm the negative log likelihood was calculated over the range of $log(A_{Ref})/E_A$ values commonly found in the literature. For each model there is a single local minimum where the surface is smooth and convex. These solutions and 95% confidence ellipses are plotted in the $log(A_{Ref})/E_A$ reference space along with selected literature values for comparison for the inner/outer boundary models (Figure 6-3a-b) and tissue viability model (Figure 6-4a). The axis limits in this figure were deliberately chosen to represent the upper limits of the values observed in the literature. The advantages of the reparameterization in equation 3-10 are apparent when the same data is plotted in the traditional $log(A)/E_A$ space (Figure 6-3c; Figure 6-4c). The high correlation between parameters causes the confidence ellipses to appear as lines and makes visual comparison using the confidence regions and literature values nearly impossible. The confidence ellipses do not overlap, suggesting that all three models are distinct and that the differing values are not a statistical consequence of the compensation law. The parameters that define these ellipses are given in Table 9.
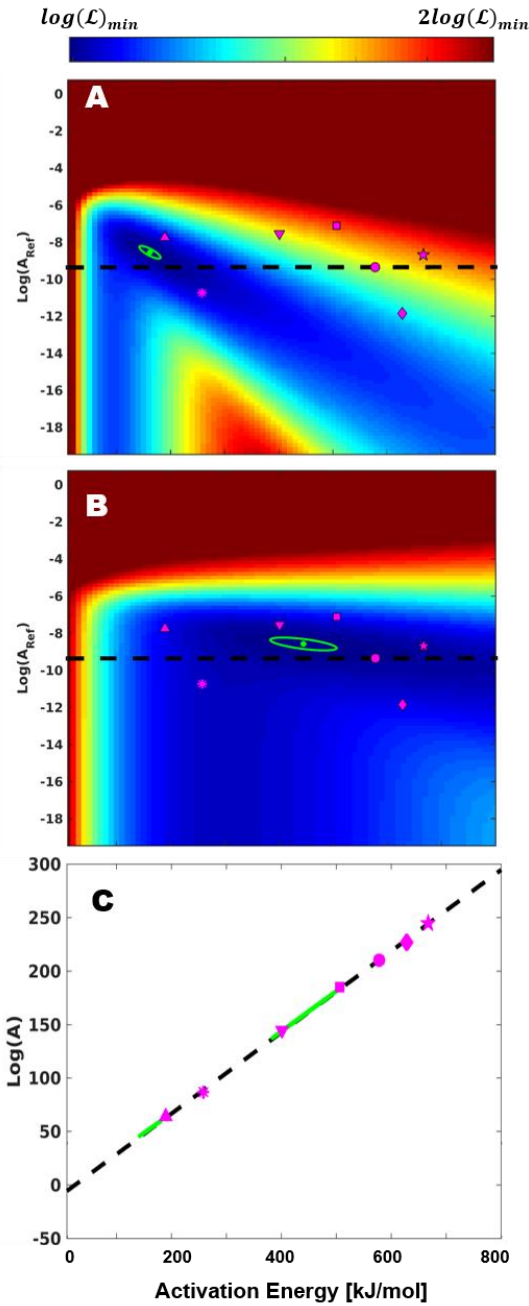
Figure 6-3: Optimal Arrhenius parameters for inner/outer boundary models. The optimal Arrhenius parameters (green circle) and 95% confidence regions (green) are shown with the negative log likelihood in the background in the $\log(A_{Ref})/E_A$ parameter space for the inner boundary (A) and outer boundary (B) models. The same data is shown in the $\log(A)/E_A$ parameter space (C). The Arrhenius parameters (magenta) from Henriques (♦), CEM (●), Qin ($T_{max} = 60°C$; ▲), Qin ($T_{max} = 50°C$; ▼), Jacques (✳), Borelli (■), and Brown (⋆). The empirical linear relationship between E_A and $\log(A)$ (black line) is also plotted for reference.
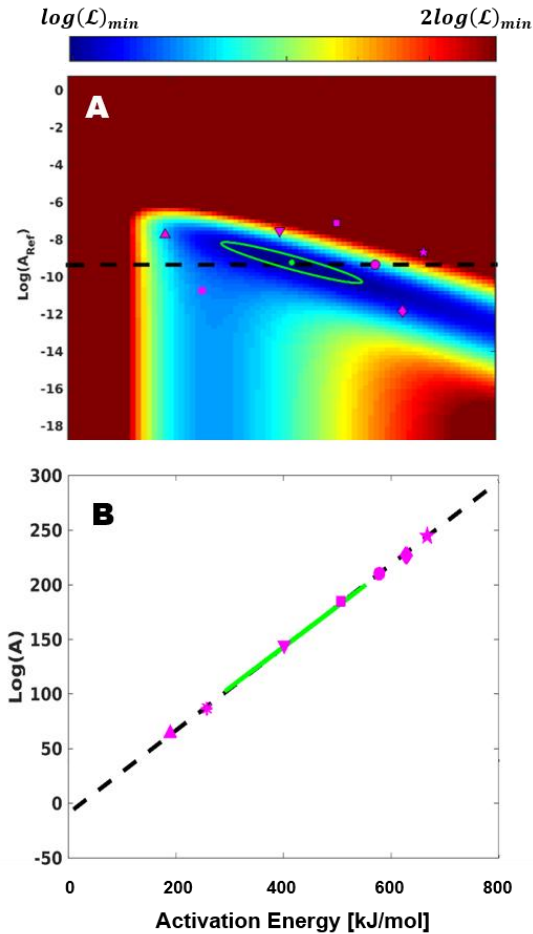
Figure 6-4: Optimal Arrhenius parameters for tissue viability boundary model The optimal Arrhenius parameters (green circle) and 95% confidence regions (green) are shown with the negative log likelihood in the background in the $log(A_{Ref})/E_A$ parameter space (A). The same data is shown in the $log(A)/E_A$ parameter space (C). The Arrhenius parameters (magenta) from Henriques (♦), CEM (●), Qin ($T_{max} = 60°C$; ▲), Qin ($T_{max} = 50°C$; ▼), Jacques (✱), Borelli (■), and Brown (⋆). The empirical linear relationship between E_A and $log(A)$ (black line) is also plotted for reference.

6.3.2 Optimal Model Parameters

The Arrhenius parameter values of the inner boundary model are lower than the outer

boundary model and span activation energies from 143kJ/mol to 182 kJ/mol. They do not overlap

with any of the models from the literature but are closest to the coefficients reported by Jacques

and Qin ($T_{Max} = 60°C$). These coefficients correspond to equivalent R_{CEM} values and $T_c{'}$ values of

0.82 and 94.5°C, respectively. The outer boundary model has higher coefficient values that span

activation energies of 384 kJ/mol to 506kJ/mol. Like the inner boundary model, these coefficients do

not overlap with any of those found in the literature but they are closest to coefficients of the CEM, Qin ($T_{Max} = 50°C$), and Borrelli models. The activation energy of the Borelli and Qin ($T_{Max} = 50°C$) model is consistent with the values of the outer boundary model but a difference in the frequency factor prevents it from overlapping with the confidence ellipse. These coefficients correspond to equivalent R_{CEM} values and T_c' values of 0.59 and 57.3°C, respectively. In both models the confidence ellipses imply a linear relationship between $log(A)$ and E_A with slopes and intercepts that are larger than used in equation 3-10.

The 95% confidence interval of the tissue viability model is centered on 445 kJ/mol and spans energies from 293 kJ/mol to 553 kJ/mol. The activation energy of the outer boundary model are within the range activation energies of the tissue viability model but they do not overlap due to a difference in the values of $log(A)$. The confidence interval is also approximately twice the size of the outer boundary model which is direct consequence of excluding pixels in the enhancing ring. This solution does not overlap with any of the literature values but the activation energies are consistent with the Borelli and Qin ($T_{Max} = 50°C$) models. The Jacques and CEM models are also just outside the lower and upper edges of the confidence interval, respectively. Similar to the inner and outer boundary models the confidence intervals imply a slope that is larger than equation 3-10. These Arrhenius parameters imply R_{CEM}=0.60 and a T_C' of 62.1°C.

	Inner Boundary Model	Outer Boundary Model	Viability Model
Activation Energy, E_A [kJ/mol]	162	445	423
Log Frequency Factor, $\log(A)$ [s^{-1}]	53.0	161	152
Minor axis length	0.187	0.251	0.350
Major axis length	20.8	65.4	139.7
Slope [kJ^{-1}]	0.366	0.376	0.3721
Intercept	-6.25	-6.99	-5.90
R_{CEM}	0.82	0.59	0.60
$T_C{'}$ [°C]	94.5	57.3	62.1

Table 9: Optimal Model Parameters and 95% Confidence Ellipses

6.3.3 Optimal Boundary Model Thresholds and Viability Thresholds

Figure 6-5 shows the probability of being within the model region as a function of FC along with the thresholds that optimize the accuracy of the boundary models model. The optimal threshold for the inner boundary model is a thermal dose of $\Omega=0.99/FC = 0.63$. This threshold is coincidentally effectively equal to the historically used threshold of $\Omega=1$. The optimal threshold for the outer boundary model is a thermal dose of $\Omega=0.22/FC = 0.20$. (Table 10) Both models performed extremely well, with areas under the curve and accuracy in excess of 0.95 and 85%, respectively. The values $CEM_{SD-thresh}$ were 1.8x10^5 min. and 32 min. for the inner and outer boundaries, respectively. T_c was found to be 61.5°C and 47.6°C for the inner and outer boundaries, respectively.

The relationship between FC and tissue viability is shown in Figure 6-6. The dose thresholds that correspond to 10, 50, and 90% probability of viability were $\Omega=0.31/FC = 0.37$, $\Omega=0.49/FC =$

0.68, and Ω=0.66/$FC = 1.07$, respectively (Table 11). Excellent classification (AUC=1.00;

accuracy=0.99) is maintained at all 3 thresholds due to the exclusion of pixels in the enhancing ring.
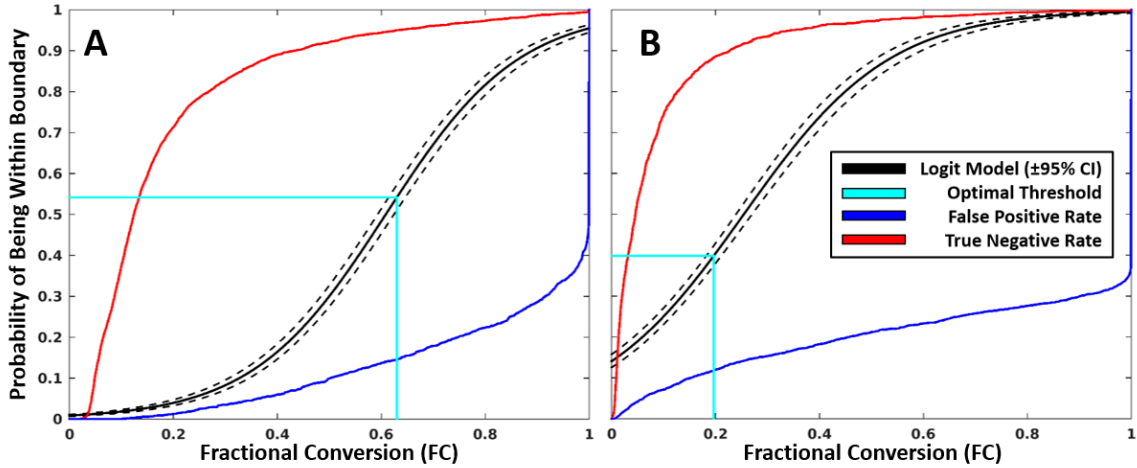
Figure 6-5: Inner and outer boundary logistic models The probability of being contained within the inner (A) and outer boundary (B) as a function of fractional conversion using the optimal Arrhenius parameters in table 1. The threshold that maximizes the accuracy is shown in cyan. The false positive (blue) and true negative rates (red) are shown for reference.

	Inner Boundary Model	Outer Boundary Model
k	7.80	7.11
FC_{50}	0.608	0.255
AR Model Thresholds ($\hat{y}/FC/\Omega$)	0.542/0.630/0.994	0.399/0.197/0.219

Table 10: Optimal Logit Parameters and Thresholds for the Inner and Outer Boundary Models
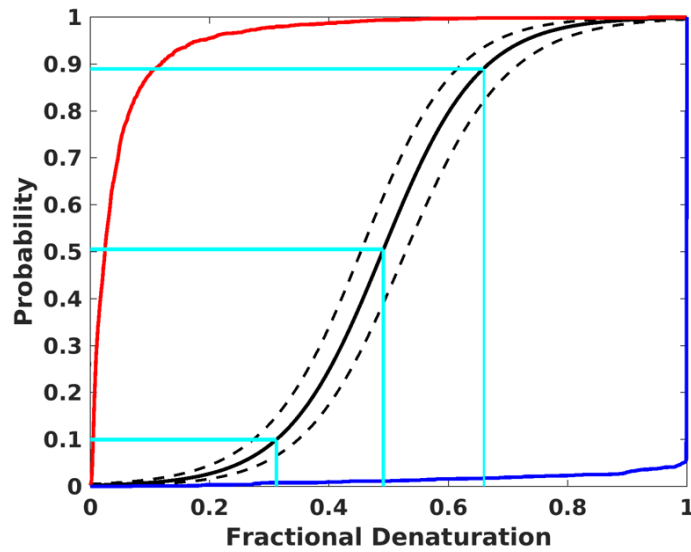
Figure 6-6: Tissue viability logistic model.The probability of tissue viability as a function of fractional conversion using the optimal Arrhenius parameters in table Table 9. The threshold that maximizes the accuracy is shown in cyan. The false positive (blue) and true negative rates (red) are shown for reference.

	$\hat{y} = 10\%$	$\hat{y} = 50\%$	$\hat{y} = 90\%$
k	12.37		
FC_{50}	0.51		
AR Model Thresholds (FC/Ω)	0.31/0.37	0.49/0.68	0.66/1.07

Table 11: Dose thresholds for tissue viability model

6.3.4 Model Predicted Region Comparison

Figure 6-7 shows a representative comparison between the areas predicted by the

inner/outer boundary models and the segmentations (a), the Henriques model (b), and CEM model

(c) for the three clinically used dose thresholds. The mean DSC/DTA/HD between the boundary

models and segmentations was 0.87/0.93 mm/2.92 mm and 0.89/ 1.1 mm/3.5 mm for the inner and

outer boundary models, respectively. In both cases the mean DTA is on the order of the pixel size (1

mm). There is consistent disagreement at the edge of the skull in Figure 6-7 that is likely caused by

partial voluming which underscores the need to remove selected areas from model fitting. On

average the Henriques dose model fell between the predicted inner and outer ring boundaries with a MDA of 1.5 mm from each boundary. The CEM model using a threshold of 60 minutes practically indistinguishable from the outer ring model with a DSC/DTA/HD of 0.98/0.24 mm/0.99 mm. The 240 and 10 minute thresholds were just inside and outside the outer boundary model and agreed within a pixel size with a DSC/DTA/HD of 0.91/2.17 mm/0.84 mm and 0.92/0.88 mm /2.93 mm, respectively. The Jacques, Borelli, and Brown models show excellent agreement with the outer and inner boundary models as previously investigated by Sherar et al. with DSC/DTA/HD = >0.96/<0.38 mm/<1.22 mm.[114]

The areas predicted by the tissue viability model are practically indistinguishable (MDA<0.75 mm (pixel size)) from one another so only the 50% viability threshold is shown in Figure 6-8 for clarity. These thresholds are closest to the areas predicted by the Henriques and CEM model using a threshold of 240 minutes. A complete comparison between all of the models for each metric is given in Appendix 2 for reference.
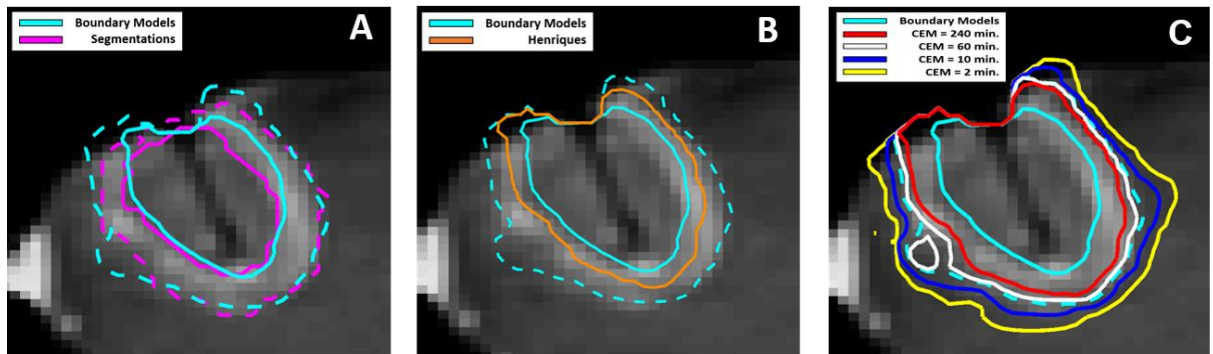
Figure 6-7 Isodose lines predicted by the inner and outer boundary models compared to the inner and outer boundary segmentations (A), Henriques model (B), and CEM model (C).
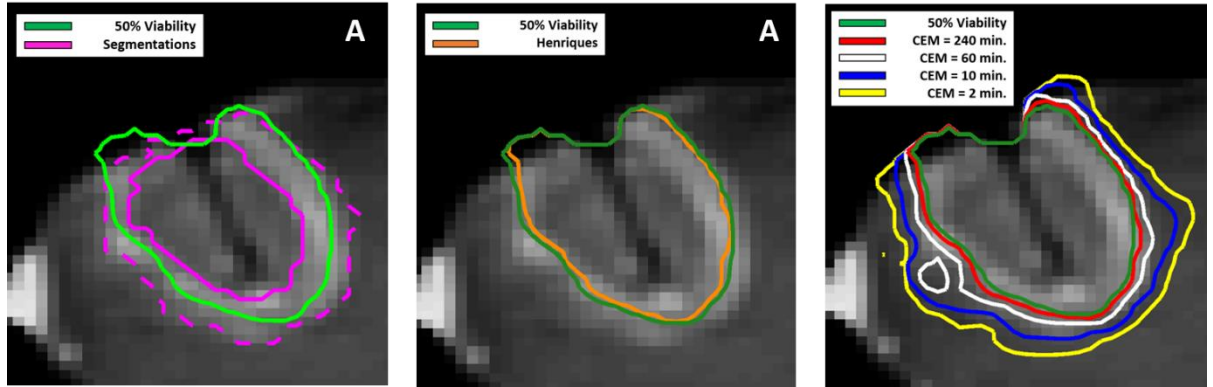
Figure 6-8: Isodose lines predicted by the tissue viability model compared to the inner and outer boundary segmentations (A), Henriques model (B), and CEM model (C).

6.4 Discussion

In this work a technique for deriving thermal dose models from intra-operative MR data acquired during thermal ablation is developed and its feasibility is demonstrated using clinical laser ablation data. To address challenges typically associated with these measurements, a coupled AR-logistic model of thermal dose and nonlinear optimization techniques were employed. This approach makes the ever expanding amount of clinical ablation data available for training thermal dose models that are predictive of clinically utilized radiologic endpoints and represents a significant shift from dose models based on non-clinical endpoints in non-human samples. However, special care must be taken to ensure that only data free of artifacts and errors should be utilized for model development.

In this work demonstrating feasibility, post-treatment contrast-enhanced images were used as a radiologic endpoint. As implemented, this technique can be generalized to any available radiologic endpoint, such as diffusion, perfusion, or magnetization transfer based techniques, provided that they can be reliably and accurately registered to the MRTI dataset. However, if the EOI cannot be reliably modeled as a first order rate process as a function of temperature, changes in the underlying approach to modeling will be required. The proposed approach is also agnostic to the modality used to deliver the thermal therapy and can be applied to any procedure where MRTI is

acquired with sufficient spatial and temporal resolution. This flexibility enables *in vivo* investigation models that are disease, tissue, and procedure specific. It is important to note that since this approach focuses on radiologic endpoints as pragmatic way of unifying treatment monitoring and assessment, the prediction of tissue viability is only as reliable as the surrogate imaging marker used. Additional research is needed to validate the procedure investigated here by correlating predicted damage to remaining viable tissue.

The inner and outer boundary models compare favorably to similar investigations found in the existing literature. The ranges of $CEM_{SD-thresh}$ and T_c are consistent with similar investigations in the literature[8,27,114,115,119,120]. Sherar et al. found that the model developed by Jacques correlated well with the inner boundary while the Brown and Borelli models correlated well with the outer boundary measured using T2-weighted imaging. For the laser heating in brain neoplasms analyzed here, our inner and outer boundary model solutions are consistent with these findings both in terms of the Arrhenius parameters and the model predicted regions. Additionally, the inner and outer boundary Arrhenius values derived from the patient data are consistent with the average effective activation energies for overall protein denaturation in 4 different cell lines measured by Qin et al if the critical temperature, T_c, is used as a surrogate for the maximum temperature (T_c=61.5°C and 47.6°C for the inner and outer boundary model, respectively). This suggests that post-treatment contrast-enhanced imaging may be an appropriate surrogate for the denaturation of major cellular proteins.

The models investigated here can provide additional insight into the utility of each thermal dose model. The AR model was optimized because it relies on only few simplifying assumptions and should be accurate over a large range of different time-temperature histories. The AR model parameters can also be conveniently converted into CEM and CT model coefficients using equations 3-10 and 3-16. The equivalent R_{CEM} values (0.82, 0.59, 0.60 for inner boundary, outer boundary,

and viability models, respectively) were substantially higher than the commonly used $R_{CEM-SD} = 0.5$. Dewhirst reported a R_{CEM} of 0.72 for $T > 47°C$ for the Henriques skin burn data but also cautioned that there is high uncertainty because the assumption of isothermal exposure was likely violated at high temperatures in the original experiment. [164] However, the technique described here does not require an isothermal exposure, suggesting that further work should be performed to see if increased R_{CEM} values are appropriate when applying the CEM model to ablation procedures.

Comparison of the model predicted regions with dose models that are currently being used clinically is of practical interest. On average, the Henriques model was halfway between the inner and outer boundaries of the thermal lesion, suggesting that it may represent a conservative estimate of the size of the thermal lesion. The 60 min. CEM threshold appears to accurately reflect the size of the outer boundary with the 240 min. and 10 min. thresholds predicting slightly smaller and larger areas, respectively. For the viability model, the transition region between viable and nonviable tissue occurred very rapidly compared to the spatial resolution of MRTI. The close agreement between the areas predicted by the viability model and the Henriques and CEM240 predicted areas suggests that these models are most consistent with the underlying assumptions of the viability model. Further study is needed to investigate if these results are consistent within a larger patient population and how they relate to clinical outcomes after extended follow up.

Chapter 7: Discussion

In this work we proposed and demonstrated the feasibility of a methodology for deriving novel thermal dose model parameters exclusively from MR data acquired during thermal ablation procedures. This approach was investigated for intra- and post-treatment effects of interest in protein coagulation phantom (SA2) using a customized multi-parametric pulse sequence (SA1) before being applied retrospectively to clinical laser ablation cases where the appearance of the thermal lesion on post-treatment contrast-enhanced imaging served as an effect of interest (SA3). The optimal Arrhenius parameters and predicted regions were consistent with expected values in both the phantom and clinical data. Using this approach, thermal dose model parameters can be tailored to clinically relevant EOIs. This represents a paradigm shift away from existing model parameters that are derived from laboratory experiments and can only be considered surrogates for clinical effects. The ability to derive thermal dose model parameters specific to clinical EOIs is increasingly important as the number of clinical ablation procedures continues to grow and additional EOIs become incorporated into clinical workflow.

While this methodology can be used to understand kinetics that govern the radiologic appearance of the thermal lesion, it does not provide any new information on the biological state of tissue. Thus, the clinical interpretation of these models can only be as useful as the underlying knowledge of how the appearance of the thermal lesion translates to a particular biological effect. A tissue viability model was investigated in specific aim 3 by integrating knowledge of the biologic state of tissue directly into the definition of the EOI. This approach allows the dose models to be interpreted in terms of a biological effect rather than simply a radiologic effect and is especially important when evidence for using multiple complementary EOIs for evaluating thermal lesions is considered. This underscores the need for continued research into the correlation of imaging with histopathologic endpoints.

Another key advantage of this methodology is the amount of data it makes available for

training dose models. Each clinical procedure has the potential to be used for continued refinement

of dose model parameters. As the amount of data increases the predictive value of the model

parameters can be rigorously assessed using training and validation cohorts. This also allows

stratification based on the tissue and procedure type that could lead to highly specific models of

thermal damage. As these models become more refined and are correlated with clinical outcomes

(e.g. local progression) there is an opportunity for thermal dose to assume a major role in these

procedures that's more akin to that used in radiation oncology. While this line of research remains

to be investigated, the methodology in this work removes significant technical barriers.

While the immediate clinical implications of this work are predominantly focused on post-

treatment EOIs, the methodology described here was also extended to intra-treatment EOIs. There

is relatively little research into these types of EOIs despite them being observed for several intrinsic

MR parameters and being associated with irreversible changes in tissue. Dynamically measuring

quantitative parameters is theoretically the ideal monitoring strategy for investigating these EOIs

but the results of this work highlights the fact that alterations to acquisition strategy to this end may

not always be necessary or optimal. Changes in T1-W signal were sufficient for training an Arrhenius

model in the protein coagulation phantom while a model using quantitative measurements of T2*

did not converge. Further research is needed to investigate these types EOIs on case by case basis to

help inform the optimal acquisition strategies and detection algorithms. If these EOIs can be

characterized with consistency they may be able to complement existing post-treatment effects.

While the hypothesis that Arrhenius models could be determined using *in vivo* MR data was

confirmed, many avenues for future research remain. T1 quantification was complicated by the

simultaneous effects slice profile and B1 inhomogeneities. Several methods for mitigating one or

both of these effects were mentioned in Chapter 4. Future experiments should focus on extending

similar modifications to 3D sequence and/or controlling the RF pulse shape in the 2D sequence.

These represent the easiest ways to achieve quantitative T1 values and would allow a rigorous

evaluation of the utility of obtaining quantitative T1 measurements for measuring intra-treatment

EOIs.

The protein phantom in Chapter 5 provided a controlled setup for measuring Arrhenius

parameters in a sample that can be easily compared to the literature. A variety of isolated proteins

(e.g. bovine serum albumin) are available and should be studied to further establish the technique.

Melting of agarose corrupted temperature data in these experiments which effectively reduced the

maximum lesions size and prevented other EOIs such as magnetization transfer, T2-W, and diffusion

from being investigated. Future experiments should implement real-time monitoring should be

integrated into the scanner so that high temperatures can be avoided entirely. Additionally, other

gels and/or heating methods should be considered to further reduce the probability of melting in

the gels. With these experimental improvements future experiments should be designed to have

both calibration and validation cohorts for both types of EOIs.

The primary focus of future work for *in vivo* data should focus on streamlining imaging

protocols to acquire additional EOIs and clinical outcomes. This includes paying close attention to

distortion correction, additional acquisitions to facilitate image registration, and avoiding MRTI

artifacts. Each of these were frequently encountered during data selection in Chapter 6. While it

may not be realistic to expect significant in clinical workflow, any attempt to reduce these errors

would expand the number of available datasets. As the number of patients is increased the

Arrhenius models should be fit independent calibration and validation sets and stratified by the

underlying pathology. This work also only used laser ablations using one vendor's laser ablation

system. This image processing should be adapted to these additional datasets to both increase the

number of patients and to assess any differences between vendors.

Bibliography

1. Goldberg, S. N., Gazelle, G. S. & Mueller, P. R. Thermal Ablation Therapy for Focal Malignancy. *Am. J. Roentgenol.* **174,** 323–331 (2000).

2. Chu, K. F. & Dupuy, D. E. Thermal ablation of tumours: biological mechanisms and advances in therapy. *Nat. Rev. Cancer* **14,** 199–208 (2014).

3. Vogl, T. J., Naguib, N. N. N., Lehnert, T. & Nour-Eldin, N.-E. A. Radiofrequency, microwave and laser ablation of pulmonary neoplasms: Clinical studies and technical considerations—Review article. *Eur. J. Radiol.* **77,** 346–357 (2011).

4. Ahmed, M., Brace, C. L., Lee, F. T. & Goldberg, S. N. Principles of and Advances in Percutaneous Ablation. *Radiology* **258,** 351–369 (2011).

5. Brace, C. L. Radiofrequency and Microwave Ablation of the Liver, Lung, Kidney, and Bone: What Are the Differences? *Curr. Probl. Diagn. Radiol.* **38,** 135–143 (2009).

6. Carrafiello, G., Laganà, D., Mangini, M., Fontana, F., Dionigi, G., Boni, L., Rovera, F., Cuffari, S. & Fugazzola, C. Microwave tumors ablation: Principles, clinical applications and review of preliminary experiences. *Int. J. Surg.* **6, Supplement 1,** S65–S69 (2008).

7. Breen, M. S., Lazebnik, R. S., Fitzmaurice, M., Nour, S. G., Lewin, J. S. & Wilson, D. L. Radiofrequency thermal ablation: Correlation of hyperacute MR lesion images with tissue response. *J. Magn. Reson. Imaging* **20,** 475–486 (2004).

8. Sloan, A. E., Ahluwalia, M. S., Valerio-Pascua, J., Manjila, S., Torchia, M. G., Jones, S. E., Sunshine, J. L., Phillips, M., Griswold, M. A., Clampitt, M., Brewer, C., Jochum, J., McGraw, M. V., Diorio, D., Ditz, G. & Barnett, G. H. Results of the NeuroBlate System first-in-humans Phase I clinical trial for recurrent glioblastoma. *J. Neurosurg.* **118,** 1202–1219 (2013).

9. Castro, D. J., Saxton, R. E., Soudant, J., Calcaterra, T., Lufkin, R., Nyerges, A., Aldinger, J., Paiva, M., Anzai, Y., Chung, P.-S., Rhee, C.-K., Ward, P. & Krespi, Y. P. Minimally Invasive Palliative

Tumor Therapy Guided by Imaging Techniques: The UCLA Experience. *J. Clin. Laser Med. Surg.* **12,** 65–73 (1994).

10. Carpentier, A., Itzcovitz, J., Payen, D., George, B., McNichols, R. J., Gowda, A., Stafford, R. J., Guichard, J.-P., Reizine, D., Delaloge, S. & Vicaut, E. Real-Time Magnetic Resonance Guided Laser Thermal Therapy for Focal Metastatic Brain Tumors. *Neurosurgery* **63,** ONS21-ONS29 (2008).

11. Gangi, A., Alizadeh, H., Wong, L., Buy, X., Dietemann, J.-L. & Roy, C. Osteoid Osteoma: Percutaneous Laser Ablation and Follow-up in 114 Patients. *Radiology* **242,** 293–301 (2007).

12. Oto, A., Sethi, I., Karczmar, G., McNichols, R., Ivancevic, M. K., Stadler, W. M., Watson, S. & Eggener, S. MR Imaging–guided Focal Laser Ablation for Prostate Cancer: Phase I Trial. *Radiology* **267,** 932–940 (2013).

13. Kennedy, J. E., ter Haar, G. R. & Cranston, D. High intensity focused ultrasound: surgery of the future? *Br. J. Radiol.* **76,** 590–599 (2003).

14. Hesley, G. K., Gorny, K. R., Henrichsen, T. L., Woodrum, D. A. & Brown, D. L. A Clinical Review of Focused Ultrasound Ablation With Magnetic Resonance Guidance: An Option for Treating Uterine Fibroids. *Ultrasound Q.* **24,** 131–139 (2008).

15. Napoli, A., Anzidei, M., Marincola, B. C., Brachetti, G., Ciolina, F., Cartocci, G., Marsecano, C., Zaccagna, F., Marchetti, L., Cortesi, E. & others. Primary pain palliation and local tumor control in bone metastases treated with magnetic resonance-guided focused ultrasound. *Invest. Radiol.* **48,** 351–358 (2013).

16. Lipsman, N., Schwartz, M. L., Huang, Y., Lee, L., Sankar, T., Chapman, M., Hynynen, K. & Lozano, A. M. MR-guided focused ultrasound thalamotomy for essential tremor: a proof-of-concept study. *Lancet Neurol.* **12,** 462–468 (2013).

17. Elias, W. J., Huss, D., Voss, T., Loomba, J., Khaled, M., Zadicario, E., Frysinger, R. C., Sperling, S. A., Wylie, S., Monteith, S. J., Druzgal, J., Shah, B. B., Harrison, M. & Wintermark, M. A pilot study of focused ultrasound thalamotomy for essential tremor. *N. Engl. J. Med.* **369,** 640–648 (2013).

18. Monteith, S., Sheehan, J., Medel, R., Wintermark, M., Eames, M., Snell, J., Kassell, N. F. & Elias, W. J. Potential intracranial applications of magnetic resonance–guided focused ultrasound surgery. *J. Neurosurg.* **118,** 215–221 (2012).

19. Datta, N. R., Ordóñez, S. G., Gaipl, U. S., Paulides, M. M., Crezee, H., Gellermann, J., Marder, D., Puric, E. & Bodis, S. Local hyperthermia combined with radiotherapy and-/or chemotherapy: Recent advances and promises for the future. *Cancer Treat. Rev.* doi:10.1016/j.ctrv.2015.05.009

20. Terraz, S., Cernicanu, A., Lepetit-Coiffé, M., Viallon, M., Salomir, R., Mentha, G. & Becker, C. D. Radiofrequency ablation of small liver malignancies under magnetic resonance guidance: progress in targeting and preliminary observations with temperature monitoring. *Eur. Radiol.* **20,** 886–897 (2009).

21. Hazle, J. D., Diederich, C. J., Kangasniemi, M., Price, R. E., Olsson, L. E. & Stafford, R. J. MRI-guided thermal therapy of transplanted tumors in the canine prostate using a directional transurethral ultrasound applicator. *J. Magn. Reson. Imaging* **15,** 409–417 (2002).

22. Köhler, M. O., Mougenot, C., Quesson, B., Enholm, J., Bail, B. L., Laurent, C., Moonen, C. T. W. & Ehnholm, G. J. Volumetric HIFU ablation under 3D guidance of rapid MRI thermometry. *Med. Phys.* **36,** 3521–3535 (2009).

23. Mahnken, A. H. & Bruners, P. CT thermometry: will it ever become ready for use? *Int. J. Clin. Pract.* **65,** 1–2 (2011).

24. Fani, F., Schena, E., Saccomandi, P. & Silvestri, S. CT-based thermometry: An overview. *Int. J. Hyperthermia* **30,** 219–227 (2014).

25. Clasen, S. & Pereira, P. L. Magnetic resonance guidance for radiofrequency ablation of liver tumors. *J. Magn. Reson. Imaging* **27,** 421–433 (2008).

26. Rieke, V. & Butts Pauly, K. MR thermometry. *J. Magn. Reson. Imaging* **27,** 376–390 (2008).

27. McDannold, N. Quantitative MRI-based temperature mapping based on the proton resonant frequency shift: Review of validation studies. *Int. J. Hyperthermia* **21,** 533–546 (2005).

28. Rieke, V., Vigen, K. K., Sommer, G., Daniel, B. L., Pauly, J. M. & Butts, K. Referenceless PRF shift thermometry. *Magn. Reson. Med.* **51,** 1223–1231 (2004).

29. Vigen, K. K., Daniel, B. L., Pauly, J. M. & Butts, K. Triggered, navigated, multi-baseline method for proton resonance frequency temperature mapping with respiratory motion. *Magn. Reson. Med.* **50,** 1003–1010 (2003).

30. Fuentes, D., Yung, J., Hazle, J. D., Weinberg, J. S. & Stafford, R. J. Kalman Filtered MR Temperature Imaging for Laser Induced Thermal Therapies. *IEEE Trans. Med. Imaging* **31,** 984–994 (2012).

31. Bley, T. A., Wieben, O., François, C. J., Brittain, J. H. & Reeder, S. B. Fat and water magnetic resonance imaging. *J. Magn. Reson. Imaging* **31,** 4–18 (2010).

32. Todd, N., Diakite, M., Payne, A. & Parker, D. L. In vivo evaluation of multi-echo hybrid PRF/T1 approach for temperature monitoring during breast MR-guided focused ultrasound surgery treatments. *Magn. Reson. Med.* **72,** 793–799 (2014).

33. Soher, B. J., Wyatt, C., Reeder, S. B. & MacFall, J. R. Noninvasive temperature mapping with MRI using chemical shift water-fat separation. *Magn. Reson. Med.* **63,** 1238–1246 (2010).

34. Taylor, B. A., Hwang, K.-P., Elliott, A. M., Shetty, A., Hazle, J. D. & Stafford, R. J. Dynamic chemical shift imaging for image-guided thermal therapy: Analysis of feasibility and potential. *Med. Phys.* **35,** 793–803 (2008).

35. Kuroda, K., Mulkern, R. v., Oshio, K., Panych, L. p., Nakai, T., Moriya, T., Okuda, S., Hynynen, K. & Joles, F. a. Temperature mapping using the water proton chemical shift: Self-referenced method with echo-planar spectroscopic imaging. *Magn. Reson. Med.* **43,** 220–225 (2000).

36. Fullerton, G. D. & Cameron, I. L. in *Biomed. Magn. Reson. Imaging* 115–151 (VCH, 1988).

37. Bottomley, P. A., Foster, T. H., Argersinger, R. E. & Pfeifer, L. M. A review of normal tissue hydrogen NMR relaxation times and relaxation mechanisms from 1–100 MHz: Dependence on tissue type, NMR frequency, temperature, species, excision, and age. *Med. Phys.* **11,** 425–448 (1984).

38. Fung, B. M. & McGaughy, T. W. The state of water in muscle as studied by pulsed NMR. *Biochim. Biophys. Acta BBA - Gen. Subj.* **343,** 663–673 (1974).

39. Fung, B. M., Durham, D. L. & Wassil, D. A. The state of water in biological systems as studied by proton and deuterium relaxation. *Biochim. Biophys. Acta BBA - Gen. Subj.* **399,** 191–202 (1975).

40. Fung, B. M. Proton and deuteron relaxation of muscle water over wide ranges of resonance frequencies. *Biophys. J.* **18,** 235–239 (1977).

41. Nelson, T. R. & Tung, S. M. Temperature dependence of proton relaxation times in vitro. *Magn. Reson. Imaging* **5,** 189–199 (1987).

42. Parker, D. L., Smith, V., Sheldon, P., Crooks, L. E. & Fussell, L. Temperature distribution measurements in two-dimensional NMR imaging. *Med. Phys.* **10,** 321–325 (1983).

43. Diakite, M., Payne, A., Todd, N. & Parker, D. L. Irreversible change in the T1 temperature dependence with thermal dose using the proton resonance frequency-T1 technique. *Magn. Reson. Med.* **69,** 1122–1130 (2013).

44. Taylor, B. A., Elliott, A. M., Hwang, K. P., Hazle, J. D. & Stafford, R. J. Correlation between the temperature dependence of intrinsic MR parameters and thermal dose measured by a rapid chemical shift imaging technique. *NMR Biomed.* **24,** 1414–1421 (2011).

45. Matsumoto, R., Oshio, K. & Jolesz, F. A. Monitoring of laser and freezing induced ablation in the liver with T1-weighted MR imaging. *J. Magn. Reson. Imaging* **2,** 555–562 (1992).

46. Peller, M., Reinl, H. M., Weigel, A., Meininger, M., Issels, R. D. & Reiser, M. T1 relaxation time at 0.2 Tesla for monitoring regional hyperthermia: feasibility study in muscle and adipose tissue. *Magn. Reson. Med.* **47,** 1194–1201 (2002).

47. Shin, W., Gu, H. & Yang, Y. Fast High-Resolution T1 Mapping using Inversion-Recovery Look-Locker Echo-Planar Imaging at Steady State: Optimization for Accuracy and Reliability. *Magn. Reson. Med. Off. J. Soc. Magn. Reson. Med. Soc. Magn. Reson. Med.* **61,** 899–906 (2009).

48. Wang, H. Z., Riederer, S. J. & Lee, J. N. Optimizing the precision in T1 relaxation estimation using limited flip angles. *Magn. Reson. Med.* **5,** 399–416 (1987).

49. Dietrich, O., Freiermuth, M., Willerding, L., Reiser, M. F. & Peller, M. Flip angle–optimized fast dynamic T1 mapping with a 3D gradient echo sequence. *Magn. Reson. Med.* **73,** 1158–1163 (2015).

50. Hey, S., de Smet, M., Stehning, C., Grüll, H., Keupp, J., Moonen, C. t. w. & Ries, M. Simultaneous T1 measurements and proton resonance frequency shift based thermometry using variable flip angles. *Magn. Reson. Med.* **67,** 457–463 (2012).

51. Han, M., Rieke, V., Scott, S. J., Ozhinsky, E., Salgaonkar, V. A., Jones, P. D., Larson, P. E. Z., Diederich, C. J. & Krug, R. Quantifying temperature-dependent T1 changes in cortical bone using ultrashort echo-time MRI. *Magn. Reson. Med.* **74,** 1548–1555 (2015).

52. Abragam, A. in *Princ. Nucl. Magn.* (Oxford University Press, 1961).

53. Knispel, R. R., Thompson, R. T. & Pintar, M. M. Dispersion of proton spin-lattice relaxation in tissues. *J. Magn. Reson. 1969* **14,** 44–51 (1974).

54. Fung, B. M. & McGaughy, T. W. The state of water in muscle as studied by pulsed NMR. *Biochim. Biophys. Acta BBA - Gen. Subj.* **343,** 663–673 (1974).

55. Fullerton, G. D., Potter, J. L. & Dornbluth, N. C. NMR relaxation of protons in tissues and other macromolecular water solutions. *Magn. Reson. Imaging* **1,** 209–226 (1982).

56. Belton, P. S., Jackson, R. R. & Packer, K. J. Pulsed NMR studies of water in striated muscle. *Biochim. Biophys. Acta BBA - Gen. Subj.* **286,** 16–25 (1972).

57. Belton, P. S., Packer, K. J. & Sellwood, T. C. Pulsed NMR studies of water in striated muscle non-freezing factor of water II. Spin-lattice relaxation times and the dynamics of the non-freezing fraction of water. *Biochim. Biophys. Acta BBA - Gen. Subj.* **304,** 56–64 (1973).

58. Bouchard, L.-S. & Bronskill, M. J. Magnetic resonance imaging of thermal coagulation effects in a phantom for calibrating thermal therapy devices. *Med. Phys.* **27,** 1141–1145 (2000).

59. Graham, S. J., Bronskill, M. J. & Henkelman, R. M. Time and temperature dependence of MR parameters during thermal coagulation of ex vivo rabbit muscle. *Magn. Reson. Med.* **39,** 198–203 (1998).

60. Gandhi, S., Daniel, B. L. & Butts, K. Temperature Dependence of Relaxation Times in Bovine Adipose Tissue. in *Proc. Int. Soc. Magn. Reson. Med.* **1998,** 701–750 (1998).

61. Henkelman, R. M., Stanisz, G. J. & Graham, S. J. Magnetization transfer in MRI: a review. *NMR Biomed.* **14,** 57–64 (2001).

62. Peng, H.-H., Huang, T.-Y., Tseng, W.-Y. I., Lin, E.-L., Chung, H.-W., Wu, C.-C., Wang, Y.-S. & Chen, W.-S. Simultaneous temperature and magnetization transfer (MT) monitoring during high-intensity focused ultrasound (HIFU) treatment: Preliminary investigation on ex vivo porcine muscle. *J. Magn. Reson. Imaging* **30,** 596–605 (2009).

63. Carasso, D., Hanannel, A. & Navon, G. A new MRI method, tested *in vitro* for the assessment of thermal coagulation and demonstrated *in vivo* on focused ultrasound ablation. *NMR Biomed.* **21,** 637–643 (2008).

64. Le Bihan, D., Delannoy, J. & Levin, R. L. Temperature mapping with MR imaging of molecular diffusion: application to hyperthermia. *Radiology* **171,** 853–857 (1989).

65. Delannoy, J., Chen, C.-N., Turner, R., Levin, R. L. & Le Bihan, D. Noninvasive temperature imaging using diffusion MRI. *Magn. Reson. Med.* **19,** 333–339 (1991).

66. Samulski, T. V., MacFall, J., Zhang, Y., Grant, W. & Charles, C. Non-invasive thermometry using magnetic resonance diffusion imaging: potential for application in hyperthermic oncology. *Int. J. Hyperth. Off. J. Eur. Soc. Hyperthermic Oncol. North Am. Hyperth. Group* **8,** 819–829 (1992).

67. MacFall, J., Prescott, D. M., Fullar, E. & Samulski, T. V. Temperature dependence of canine brain tissue diffusion coefficient measured in vivo with magnetic resonance echo-planar imaging. *Int. J. Hyperthermia* **11,** 73–86 (1995).

68. Morvan, D., Leroy-Willig, A., Malgouyres, A., Cuenod, C. A., Jehenson, P. & Syrota, A. Simultaneous temperature and regional blood volume measurements in human muscle using an MRI fast diffusion technique. *Magn. Reson. Med.* **29,** 371–377 (1993).

69. Quesson, B., de Zwart, J. A. & Moonen, C. T. W. Magnetic resonance temperature imaging for guidance of thermotherapy. *J. Magn. Reson. Imaging* **12,** 525–533 (2000).

70. Poorter, J. D., Wagter, C. D., Deene, Y. D., Thomsen, C., Ståhlberg, F. & Achten, E. Noninvasive MRI Thermometry with the Proton Resonance Frequency (PRF) Method: In Vivo Results in Human Muscle. *Magn. Reson. Med.* **33,** 74–81 (1995).

71. Tracz, R. A., Wyman, D. R., Little, P. B., Towner, R. A., Stewart, W. A., Schatz, S. W., Pennock, P. W. & Wilson, B. C. Magnetic resonance imaging of interstitial laser photocoagulation in brain. *Lasers Surg. Med.* **12,** 165–173 (1992).

72. Farahani, K., Mischel, P. S., Black, K. L., De Salles, A. A., Anzai, Y. & Lufkin, R. B. Hyperacute thermal lesions: MR imaging evaluation of development in the brain. *Radiology* **196,** 517–520 (1995).

73. Lazebnik, R. S., Weinberg, B. D., Breen, M. S., Lewin, J. S. & Wilson, D. L. Sub-acute changes in lesion conspicuity and geometry following MR-guided radiofrequency ablation. *J. Magn. Reson. Imaging* **18,** 353–359 (2003).

74. Medvid, R., Ruiz, A., Komotar, R. J., Jagid, J. R., Ivan, M. E., Quencer, R. M. & Desai, M. B. Current Applications of MRI-Guided Laser Interstitial Thermal Therapy in the Treatment of Brain Neoplasms and Epilepsy: A Radiologic and Neurosurgical Overview. *Am. J. Neuroradiol.* **36,** 1998–2006 (2015).

75. Lencioni, R., Cioni, D. & Bartolozzi, C. Percutaneous radiofrequency thermal ablation of liver malignancies: techniques, indications, imaging findings, and clinical results. *Abdom. Imaging* **26,** 345–360

76. Svatek, R. S., Sims, R., Anderson, J. K., Abdel-Aziz, K. & Cadeddu, J. A. Magnetic resonance imaging characteristics of renal tumors after radiofrequency ablation. *Urology* **67,** 508–512 (2006).

77. Wile, G. E., Leyendecker, J. R., Krehbiel, K. A., Dyer, R. B. & Zagoria, R. J. CT and MR Imaging after Imaging-guided Thermal Ablation of Renal Neoplasms. *RadioGraphics* **27,** 325–339 (2007).

78. Hectors, S. J. C. G., Jacobs, I., Strijkers, G. J. & Nicolay, K. Amide proton transfer imaging of high intensity focused ultrasound-treated tumor tissue. *Magn. Reson. Med.* **72,** 1113–1122 (2014).

79. Schwabe, B., Kahn, T., Harth, T., Ulrich, F. & Schwarzmaier, H. J. Laser-induced thermal lesions in the human brain: short- and long-term appearance on MRI. *J. Comput. Assist. Tomogr.* **21,** 818–825 (1997).

80. Rao, M. S., Hargreaves, E. L., Khan, A. J., Haffty, B. G. & Danish, S. F. Magnetic Resonance-Guided Laser Ablation Improves Local Control for Postradiosurgery Recurrence and/or Radiation Necrosis: *Neurosurgery* **74,** 658–667 (2014).

81. Merkle, E. M., Shonk, J. R., Zheng, L., Duerk, J. L. & Lewin, J. S. MR imaging-guided radiofrequency thermal ablation in the porcine brain at 0.2 T. *Eur. Radiol.* **11,** 884–892 (2001).

82. Merkle, E. M., Haaga, J. R., Duerk, J. L., Jacobs, G. H., Brambs, H.-J. & Lewin, J. S. MR Imaging-guided Radio-frequency Thermal Ablation in the Pancreas in a Porcine Model with a Modified Clinical C-Arm System. *Radiology* **213,** 461–467 (1999).

83. Boaz, T. L., Lewin, J. S., Chung, Y.-C., Duerk, J. L., Clampitt, M. E. & Haaga, J. R. MR monitoring of MR-guided radiofrequency thermal ablation of normal liver in an animal model. *J. Magn. Reson. Imaging* **8,** 64–69 (1998).

84. Merkle, E. M., Boll, D. T., Boaz, T., Duerk, J. L., Chung, Y. C., Jacobs, G. H., Varnes, M. E. & Lewin, J. S. MRI-guided radiofrequency thermal ablation of implanted VX2 liver tumors in a rabbit model: Demonstration of feasibility at 0.2 T. *Magn. Reson. Med.* **42,** 141–149 (1999).

85. Chen, L., Bouley, D. M., Harris, B. T. & Butts, K. MRI study of immediate cell viability in focused ultrasound lesions in the rabbit brain. *J. Magn. Reson. Imaging* **13,** 23–30 (2001).

86. Morrison, P. R., Jolesz, F. A., Charous, D., Mulkern, R. V., Hushek, S. G., Margolis, R. & Fried, M. P. Invited. MRI of laser-induced interstitial thermal injury in an in vivo animal liver model with histologic correlation. *J. Magn. Reson. Imaging* **8,** 57–63 (1998).

87. Breen, M. S., Breen, M., Butts, K., Chen, L., Saidel, G. M. & Wilson, D. L. MRI-guided Thermal Ablation Therapy: Model and Parameter Estimates to Predict Cell Death from MR Thermometry Images. *Ann. Biomed. Eng.* **35,** 1391–1403 (2007).

88. Wijlemans, J. W., Deckers, R., van den Bosch, M. A. A. J., Seinstra, B. A., van Stralen, M., van Diest, P. J., Moonen, C. T. W. & Bartels, L. W. Evolution of the Ablation Region After Magnetic Resonance–Guided High-Intensity Focused Ultrasound Ablation in a Vx2 Tumor Model: *Invest. Radiol.* **48,** 381–386 (2013).

89. Graham, S. j., Stanisz, G. j., Kecojevic, A., Bronskill, M. j. & Henkelman, R. m. Analysis of changes in MR properties of tissues after heat treatment. *Magn. Reson. Med.* **42,** 1061–1071 (1999).

90. Carasso, D., Eliav, U. & Navon, G. Nuclear magnetic resonance parameters for monitoring coagulation of liver tissue. *Magn. Reson. Med.* **54,** 1082–1086 (2005).

91. Hectors, S. J. C. G., Jacobs, I., Strijkers, G. J. & Nicolay, K. Multiparametric MRI Analysis for the Identification of High Intensity Focused Ultrasound-Treated Tumor Tissue. *PLOS ONE* **9,** e99936 (2014).

92. Hectors, S. J. C. G., Jacobs, I., Heijman, E., Keupp, J., Berben, M., Strijkers, G. J., Grüll, H. & Nicolay, K. Multiparametric MRI analysis for the evaluation of MR-guided high intensity focused ultrasound tumor treatment. *NMR Biomed.* **28,** 1125–1140 (2015).

93. Cheng, H.-L. M., Haider, M. A., Dill-Macky, M. J., Sweet, J. M., Trachtenberg, J. & Gertner, M. R. MRI and contrast-enhanced ultrasound monitoring of prostate microwave focal thermal therapy: An in vivo canine study. *J. Magn. Reson. Imaging* **28,** 136–143 (2008).

94. Jacobs, M. A., Herskovits, E. H. & Kim, H. S. Uterine Fibroids: Diffusion-weighted MR Imaging for Monitoring Therapy with Focused Ultrasound Surgery—Preliminary Study. *Radiology* **236,** 196–203 (2005).

95. Cheng, H.-L. M., Purcell, C. M., Bilbao, J. M. & Plewes, D. B. Prediction of subtle thermal histopathological change using a novel analysis of Gd-DTPA kinetics. *J. Magn. Reson. Imaging* **18,** 585–598 (2003).

96. Kim, Y., Kim, B.-G., Rhim, H., Bae, D.-S., Lee, J.-W., Kim, T.-J., Choi, C. H., Lee, Y.-Y. & Lim, H. K. Uterine Fibroids: Semiquantitative Perfusion MR Imaging Parameters Associated with the Intraprocedural and Immediate Postprocedural Treatment Efficiencies of MR Imaging–guided High-Intensity Focused Ultrasound Ablation. *Radiology* **273,** 462–471 (2014).

97. Henriques Jr., F. C. Studies of Thermal Injury. V. The predictability and the significance of thermally induced rate processes leading to irreversible epidermal injury. *Arch. Pathol.* **43,** 489–502 (1947).

98. He, X. & Bischof, J. C. Quantification of Temperature and Injury Response in Thermal Therapy and Cryosurgery. *Crit. Rev. Biomed. Eng.* **31,** 355–422 (2003).

99. Pearce, J. A. Comparative analysis of mathematical models of cell death and thermal damage processes. *Int. J. Hyperth. Off. J. Eur. Soc. Hyperthermic Oncol. North Am. Hyperth. Group* **29,** 262–280 (2013).

100. Diller, K. R., Valvano, J. W. & Pearce, J. A. in *CRC Handb. Therm. Eng.* 114–187

101. Moritz, A. R. & Henriques, F. C. Studies of Thermal Injury. II. The Relative Importance of Time and Surface Temperature in the Causationof Cutaneous Burns. *Am. J. Pathol.* **23,** 695–720 (1947).

102. Sapareto, S. A. & Dewey, W. C. Thermal dose determination in cancer therapy. *Int. J. Radiat. Oncol.* **10,** 787–800 (1984).

103. Jacques, S., Newman, C. & He, X. Y. Thermal coagulation of tissues. Liver studies indicate a distribution of rate parameters, not a single rate parameter, describes the coagulation process. in *Am. Soc. Mech. Eng. Heat Transf. Div. Publ. HTD* (ASME, 1991).

104. Borrelli, M. J., Thompson, L. L., Cain, C. A. & Dewey, W. C. Time-temperature analysis of cell killing of BHK cells heated at temperatures in the range of 43.5°C to 57.0°C. *Int. J. Radiat. Oncol.* **19,** 389–399 (1990).

105. Brown, S. L., Hunt, J. W. & Hill, R. P. Differential thermal sensitivity of tumour and normal tissue microvascular response during hyperthermia. *Int. J. Hyperth. Off. J. Eur. Soc. Hyperthermic Oncol. North Am. Hyperth. Group* **8,** 501–514 (1992).

106. Miles, C. A. & Bailey, A. J. Studies of the Collagen-like Peptide (Pro-Pro-Gly)10 Confirm that the Shape and Position of the Type I Collagen Denaturation Endotherm is Governed by the Rate of Helix Unfolding. *J. Mol. Biol.* **337,** 917–931 (2004).

107. Miles, C. A. Kinetics of the helix/coil transition of the collagen-like peptide (Pro-Hyp-Gly)10. *Biopolymers* **87,** 51–67 (2007).

108. Qin, Z., Balasubramanian, S. K., Wolkers, W. F., Pearce, J. A. & Bischof, J. C. Correlated Parameter Fit of Arrhenius Model for Thermal Denaturation of Proteins and Cells. *Ann. Biomed. Eng.* **42,** 2392–2404 (2014).

109. He, X., Wolkers, W. F., Crowe, J. H., Swanlund, D. J. & Bischof, J. C. In Situ Thermal Denaturation of Proteins in Dunning AT-1 Prostate Cancer Cells: Implication for Hyperthermic Cell Injury. *Ann. Biomed. Eng.* **32,** 1384–1398 (2004).

110. Weaver, J. A. & Stoll, A. M. *Mathematical Model of Skin Exposed to Thermal Radiation*. (U.S. Naval Air Development Center, 1967).

111. Rosenberg, B., Kemeny, G., Switzer, R. C. & Hamilton, T. C. Quantitative Evidence for Protein Denaturation as the Cause of Thermal Death. *Nature* **232,** 471–473 (1971).

112. Wright, N. T. On a relationship between the Arrhenius parameters from thermal damage studies. *J. Biomech. Eng.* **125,** 300–304 (2003).

113. McNichols, R. J., Gowda, A., Kangasniemi, M., Bankson, J. A., Price, R. E. & Hazle, J. D. MR thermometry-based feedback control of laser interstitial thermal therapy at 980 nm. *Lasers Surg. Med.* **34,** 48–55 (2004).

114. Sherar, M. D., Moriarty, J. A., Kolios, M. C., Chen, J. C., Peters, R. D., Ang, L. C., Hinks, R. S., Henkelman, R. M., Bronskill, M. J. & Kucharcyk, W. Comparison of thermal damage calculated using magnetic resonance thermometry, with magnetic resonance imaging post-treatment and histology, after interstitial microwave thermal therapy of rabbit brain. *Phys. Med. Biol.* **45,** 3563 (2000).

115. Yung, J. P., Shetty, A., Elliott, A., Weinberg, J. S., McNichols, R. J., Gowda, A., Hazle, J. D. & Stafford, R. J. Quantitative comparison of thermal dose models in normal canine brain. *Med. Phys.* **37,** 5313–5321 (2010).

116. McDannold, N., Hynynen, K., Wolf, D., Wolf, G. & Jolesz, F. MRI evaluation of thermal ablation of tumors with focused ultrasound. *J. Magn. Reson. Imaging* **8,** 91–100 (1998).

117. Damianou, C. A., Hynynen, K. & Fan, X. Evaluation of accuracy of a theoretical model for predicting the necrosed tissue volume during focused ultrasound surgery. *IEEE Trans. Ultrason. Ferroelectr. Freq. Control* **42,** 182–187 (1995).

118. McDannold, N. J., King, R. L., Jolesz, F. A. & Hynynen, K. H. Usefulness of MR Imaging-Derived Thermometry and Dosimetry in Determining the Threshold for Tissue Damage Induced by Thermal Surgery in Rabbits. *Radiology* **216,** 517–523 (2000).

119. Chen, L., Wansapura, J. P., Heit, G. & Butts, K. Study of laser ablation in the in vivo rabbit brain with MR thermometry. *J. Magn. Reson. Imaging* **16,** 147–152 (2002).

120. Peters, R. D., Chan, E., Trachtenberg, J., Jothy, S., Kapusta, L., Kucharczyk, W. & Henkelman, R. M. Magnetic resonance thermometry for predicting thermal damage: An application of interstitial laser coagulation in an in vivo canine prostate model. *Magn. Reson. Med.* **44,** 873–883 (2000).

121. Haacke, E. M., Brown, R. W., Thompson, M. R., Venkatesan, R. & others. *Magnetic resonance imaging: physical principles and sequence design*. **82,** (Wiley-Liss New York:, 1999).

122. Bernstein, M. A., King, K. F. & Zhou, X. J. *Handbook of MRI pulse sequences*. (Elsevier, 2004).

123. Gudbjartsson, H. & Patz, S. The Rician Distribution of Noisy MRI Data. *Magn. Reson. Med. Off. J. Soc. Magn. Reson. Med. Soc. Magn. Reson. Med.* **34,** 910–914 (1995).

124. Deoni, S. C. L., Rutt, B. K. & Peters, T. M. Rapid combined T1 and T2 mapping using gradient recalled acquisition in the steady state. *Magn. Reson. Med.* **49,** 515–526 (2003).

125. Schabel, M. C. & Morrell, G. R. Uncertainty in T 1 mapping using the variable flip angle method with two flip angles. *Phys. Med. Biol.* **54,** N1 (2009).

126. Pohmann, R. & Scheffler, K. A theoretical and experimental comparison of different techniques for B1 mapping at very high fields. *NMR Biomed.* **26,** 265–275 (2013).

127. Cunningham, C. H., Pauly, J. M. & Nayak, K. S. Saturated double-angle method for rapid B1+ mapping. *Magn. Reson. Med.* **55,** 1326–1333 (2006).

128. Hurley, S. A., Yarnykh, V. L., Johnson, K. M., Field, A. S., Alexander, A. L. & Samsonov, A. A. Simultaneous variable flip angle–actual flip angle imaging method for improved accuracy and precision of three-dimensional T1 and B1 measurements. *Magn. Reson. Med.* **68,** 54–64 (2012).

129. Yarnykh, V. L. Actual flip-angle imaging in the pulsed steady state: a method for rapid three-dimensional mapping of the transmitted radiofrequency field. *Magn. Reson. Med.* **57,** 192–200 (2007).

130. Sacolick, L. I., Wiesinger, F., Hancu, I. & Vogel, M. W. B1 mapping by Bloch-Siegert shift. *Magn. Reson. Med.* **63,** 1315–1322 (2010).

131. Insko, E. K. & Bolinger, L. Mapping of the Radiofrequency Field. *J. Magn. Reson. A* **103,** 82–85 (1993).

132. Haacke, E. M. in *Magn. Reson. Imaging Phys. Princ. Seq. Des.* 466–467 (Wilery-Liss, 1999).

133. Hsu, J.-J. Flip-angle profile of slice-selective excitation and the measurement of the MR longitudinal relaxation time with steady-state magnetization. *Phys. Med. Biol.* **60,** 5785 (2015).

134. Taylor, B. Dynamic Chemical Shift Imaging for Image-Guided Thermal Therapy. (2010).

135. Lutti, A., Hutton, C., Finsterbusch, J., Helms, G. & Weiskopf, N. Optimization and validation of methods for mapping of the radiofrequency transmit field at 3T. *Magn. Reson. Med.* **64,** 229–238 (2010).

136. Parker, G. J. M., Barker, G. J. & Tofts, P. S. Accurate multislice gradient echo T1 measurement in the presence of non-ideal RF pulse shape and RF field nonuniformity. *Magn. Reson. Med.* **45,** 838–845 (2001).

137. Treier, R., Steingoetter, A., Fried, M., Schwizer, W. & Boesiger, P. Optimized and combined T1 and B1 mapping technique for fast and accurate T1 quantification in contrast-enhanced abdominal MRI. *Magn. Reson. Med.* **57,** 568–576 (2007).

138. Todd, N., Diakite, M., Payne, A. & Parker, D. L. Hybrid proton resonance frequency/T1 technique for simultaneous temperature monitoring in adipose and aqueous tissues. *Magn. Reson. Med.* **69,** 62–70 (2013).

139. Sharp, K. Entropy—enthalpy compensation: Fact or artifact? *Protein Sci.* **10,** 661–667 (2001).

140. Liu, L. & Guo, Q.-X. Isokinetic Relationship, Isoequilibrium Relationship, and Enthalpy–Entropy Compensation. *Chem. Rev.* **101,** 673–696 (2001).

141. Krug, R. R., Hunter, W. G. & Grieger, R. A. Enthalpy-entropy compensation. 1. Some fundamental statistical problems associated with the analysis of van't Hoff and Arrhenius data. *J. Phys. Chem.* **80,** 2335–2341 (1976).

142. Barrie, P. J. The mathematical origins of the kinetic compensation effect: 1. The effect of random experimental errors. *Phys. Chem. Chem. Phys.* **14,** 318–326 (2012).

143. Barrie, P. J. The mathematical origins of the kinetic compensation effect: 2. The effect of systematic errors. *Phys. Chem. Chem. Phys.* **14,** 327–336 (2012).

144. Schwaab, M. & Pinto, J. C. Optimum reference temperature for reparameterization of the Arrhenius equation. Part 1: Problems involving one kinetic constant. *Chem. Eng. Sci.* **62,** 2750–2764 (2007).

145. Schwaab, M., Lemos, L. P. & Pinto, J. C. Optimum reference temperature for reparameterization of the Arrhenius equation. Part 2: Problems involving multiple reparameterizations. *Chem. Eng. Sci.* **63,** 2895–2906 (2008).

146. Taylor, B. A., Elliott, A. M., Hwang, K.-P., Shetty, A., Hazle, J. D. & Stafford, R. J. Measurement of temperature dependent changes in bone marrow using a rapid chemical shift imaging technique. *J. Magn. Reson. Imaging* **33,** 1128–1135 (2011).

147. Bozdogan, H. Model selection and Akaike's Information Criterion (AIC): The general theory and its analytical extensions. *Psychometrika* **52,** 345–370 (1987).

148. Van der Plancken, I., Van Loey, A. & Hendrickx, M. E. Kinetic study on the combined effect of high pressure and temperature on the physico-chemical properties of egg white proteins. *J. Food Eng.* **78,** 206–216 (2007).

149. Van der Plancken, I., Van Loey, A. & Hendrickx, M. E. Effect of heat-treatment on the physico-chemical properties of egg white proteins: A kinetic study. *J. Food Eng.* **75,** 316–326 (2006).

150. Weijers, M., Barneveld, P. A., Cohen Stuart, M. A. & Visschers, R. W. Heat-induced denaturation and aggregation of ovalbumin at neutral pH described by irreversible first-order kinetics. *Protein Sci. Publ. Protein Soc.* **12,** 2693–2703 (2003).

151. Rumbo, M., Chirdo, F. G., Fossati, C. A. & Añón, M. C. Analysis of structural properties and immunochemical reactivity of heat-treated ovalbumin. *J. Agric. Food Chem.* **44,** 3793–3798 (1996).

152. Zijdenbos, A. P., Dawant, B. M., Margolin, R. A. & Palmer, A. C. Morphometric analysis of white matter lesions in MR images: method and validation. *IEEE Trans. Med. Imaging* **13,** 716–724 (1994).

153. Jethwa, P. R., Barrese, J. C., Gowda, A., Shetty, A. & Danish, S. F. Magnetic Resonance Thermometry-Guided Laser-Induced Thermal Therapy for Intracranial Neoplasms: Initial Experience. *Oper. Neurosurg.* **71,** ons133-ons145 (2012).

154. Hawasli, A. H., Bagade, S., Shimony, J. S., Miller-Thomas, M. & Leuthardt, E. C. Magnetic Resonance Imaging-Guided Focused Laser Interstitial Thermal Therapy for Intracranial Lesions: Single-Institution Series. *Neurosurgery* **73,** 1007–1017 (2013).

155. Missios, S., Bekelis, K. & Barnett, G. H. Renaissance of laser interstitial thermal ablation. *Neurosurg. Focus* **38,** E13 (2015).

156. Mohammadi, A. M., Hawasli, A. H., Rodriguez, A., Schroeder, J. L., Laxton, A. W., Elson, P., Tatter, S. B., Barnett, G. H. & Leuthardt, E. C. The role of laser interstitial thermal therapy in enhancing progression-free survival of difficult-to-access high-grade gliomas: a multicenter study. *Cancer Med.* **3,** 971–979 (2014).

157. Tatsui, C. E., Stafford, R. J., Li, J., Sellin, J. N., Amini, B., Rao, G., Suki, D., Ghia, A. J., Brown, P., Lee, S.-H., Cowles, C. E., Weinberg, J. S. & Rhines, L. D. Utilization of laser interstitial

thermotherapy guided by real-time thermal MRI as an alternative to separation surgery in the management of spinal metastasis. *J. Neurosurg. Spine* **23,** 400–411 (2015).

158. Rempp, H., Hoffmann, R., Roland, J., Buck, A., Kickhefel, A., Claussen, C. D., Pereira, P. L., Schick, F. & Clasen, S. Threshold-based prediction of the coagulation zone in sequential temperature mapping in MR-guided radiofrequency ablation of liver tumours. *Eur. Radiol.* **22,** 1091–1100 (2011).

159. Kickhefel, A., Rosenberg, C., Weiss, C. R., Rempp, H., Roland, J., Schick, F. & Hosten, N. Clinical evaluation of MR temperature monitoring of laser-induced thermotherapy in human liver using the proton-resonance-frequency method and predictive models of cell death. *J. Magn. Reson. Imaging* **33,** 704–709 (2011).

160. Hectors, S. J. C. G., Jacobs, I., Moonen, C. T. W., Strijkers, G. J. & Nicolay, K. MRI methods for the evaluation of high intensity focused ultrasound tumor treatment: Current status and future needs. *Magn. Reson. Med.* **75,** 302–317 (2016).

161. Avants, B. B., Tustison, N. J., Song, G., Cook, P. A., Klein, A. & Gee, J. C. A reproducible evaluation of ANTs similarity metric performance in brain image registration. *NeuroImage* **54,** 2033–2044 (2011).

162. Smith, S. M. Fast robust automated brain extraction. *Hum. Brain Mapp.* **17,** 143–155 (2002).

163. Dewey, W. C., Hopwood, L. E., Sapareto, S. A. & Gerweck, L. E. Cellular Responses to Combinations of Hyperthermia and Radiation. *Radiology* **123,** 463–474 (1977).

164. Dewhirst, M. W., Viglianti, B. L., Lora-Michiels, M., Hanson, M. & Hoopes, P. J. Basic principles of thermal dosimetry and thermal thresholds for tissue damage from hyperthermia. *Int. J. Hyperthermia* **19,** 267–294 (2003).

Appendix 1: Pulse Sequence and Exposure Parameters from Chapter 5

	Group A			Group B								Group C					
Field of View (cm)	19.6	19.6	19.6	19.2	19.2	19.2	19.2	19.2	19.2	19.2	19.2	19.2	19.2	19.2	19.2	19.2	19.2
Repetition Time (ms)	35	35	35	35	35	35	35	35	35	35	35	70	70	70	100	100	100
Echo Train Length	8	8	8	8	8	8	8	8	8	8	8	8	8	8	8	8	8
Minimum Echo Time (ms)	2.1	2.1	2.1	1.8	1.8	1.8	1.8	1.8	1.8	1.8	1.8	1.8	1.8	1.8	1.8	1.8	1.8
Echo Spacing (ms)	2.5	2.5	2.5	2.1	2.1	2.1	2.1	2.1	2.1	2.1	2.1	2.1	2.1	2.1	2.1	2.1	2.1
Receive Bandwidth (Hz/pixel)	195	195	195	326	326	326	326	326	326	326	326	326	326	326	326	326	326
Flip Angle (°)	30	30	30	30	30	30	30	30	30	30	30	25	25	25	25	25	25
Number of Slices	1	1	1	1	1	1	1	1	1	1	1	3	3	3	3	3	3
mfa_mode	1	1	1	0	0	0	0	0	0	0	0	0	0	0	0	0	0
mfa_low_flip	2	2	2	2	2	2	2	2	2	2	2	2	2	2	2	2	2
Time between phases (s)	4.8	4.8	4.8	4.8	4.8	4.8	4.8	4.8	4.8	4.8	4.8	7.9	7.9	7.9	12.4	12.4	12.4

Table 12: Pulse sequence parameters for phantom experiments in Chapter 5

Group A	8 min@10W
	8 min@12W
	8 min@14W
Group B	9 min@10W
	5 min@15W; 1 min@0W; 2 min@15W
	9.5 min@11.5W
	1.5 min@15W; 7 min@11.5W
	2 min@15W;7.5min@12.5W
	2 min@15W;7.5 min@12.5W
	2 min@15W; 5 min@12.5W; 1 min@13.5W; 1.5 min@12.5W
	16 min@12.5W
Group C	10 min@10W
	12 min@7.5W
	11 min@8.75W
	14 min@7.5W
	12 min@8.25W
	17 min@7.5

Table 13: Laser exposure parameters for experiments in Chapter 5. All changes to laser powers are consecutive with minimal interruption (<1 second).

Appendix 2: DSC, HD, and MDA for Segmentations and Models in Chapter 6

	Inner Seg.	Outer Seg.	Inner Boundary	Outer Boundary	Henriques	CEM (2 min.)	CEM (10 min.)	CEM (60 min)	CEM (240 min.)	Jacques	Borelli	Brown	Viability 10%	Viability 50%	Viability 90%
Inner Seg.	1.00														
Outer Seg.	0.66	1.00													
Inner Boundary	0.87	0.64	1.00												
Outer Boundary	0.69	0.89	0.67	1.00											
Henriques	0.83	0.79	0.83	0.83	1.00										
CEM (2 min.)	0.54	0.83	0.52	0.83	0.67	1.00									
CEM (10 min.)	0.62	0.88	0.60	0.92	0.76	0.90	1.00								
CEM (60 min)	0.71	0.89	0.69	0.98	0.85	0.80	0.90	1.00							
CEM (240 min.)	0.77	0.86	0.75	0.91	0.92	0.74	0.83	0.93	1.00						
Jacques	0.87	0.61	0.96	0.63	0.79	0.49	0.57	0.65	0.71	1.00					
Borelli	0.68	0.90	0.66	0.99	0.82	0.83	0.93	0.97	0.90	0.63	1.00				
Brown	0.72	0.89	0.70	0.96	0.87	0.79	0.88	0.99	0.95	0.67	0.96	1.00			
Viability 10%	0.77	0.86	0.75	0.91	0.92	0.74	0.83	0.93	0.99	0.72	0.90	0.94	1.00		
Viability 50%	0.76	0.87	0.74	0.92	0.90	0.75	0.85	0.95	0.99	0.70	0.92	0.96	0.98	1.00	
Viability 90%	0.81	0.82	0.80	0.86	0.97	0.70	0.79	0.88	0.95	0.76	0.85	0.90	0.95	0.94	1.00

Table 14: DSC Values for the segmentations and models in Chapter 6

	Inner Seg.	Outer Seg.	Inner Boundary	Outer Boundary	Henriques	CEM (2 min.)	CEM (10 min.)	CEM (60 min)	CEM (240 min.)	Jacques	Borelli	Brown	Viability 10%	Viability 50%	Viability 90%
Inner Seg.															
Outer Seg.	5.55														
Inner Boundary	2.92	6.25													
Outer Boundary	5.65	3.47	6.07												
Henriques	3.58	4.05	3.37	3.23											
CEM (2 min.)	8.13	4.66	8.68	4.65	6.66										
CEM (10 min.)	6.86	4.00	7.43	2.93	5.23	3.04									
CEM (60 min)	5.41	3.35	5.75	0.99	2.93	5.02	3.47								
CEM (240 min.)	4.47	3.35	4.58	2.17	1.64	5.76	4.35	1.81							
Jacques	2.61	6.15	1.11	5.91	3.24	8.54	7.21	5.60	4.48						
Borelli	5.76	3.47	6.18	0.47	3.36	4.48	2.76	1.15	2.32	6.02					
Brown	5.23	3.31	5.54	1.22	2.71	5.19	3.65	0.60	1.58	5.42	1.40				
Viability 10%	4.33	3.47	4.43	2.34	1.46	5.88	4.44	2.03	0.62	4.34	2.49	1.84			
Viability 50%	4.64	3.39	4.82	1.97	1.91	5.62	4.21	1.67	0.56	4.72	2.14	1.42	0.81		
Viability 90%	3.88	3.83	3.76	2.97	0.76	6.38	5.03	2.69	1.31	3.64	3.10	2.46	1.06	1.57	

Table 15: HD Values for the segmentations and models in Chapter 6

	Inner Seg.	Outer Seg.	Inner Boundary	Outer Boundary	Henriques	CEM (2 min.)	CEM (10 min.)	CEM (60 min)	CEM (240 min.)	Jacques	Borelli	Brown	Viability 10%	Viability 50%	Viability 90%
Inner Seg.															
Outer Seg.	2.93														
Inner Boundary	0.94	3.19													
Outer Boundary	2.77	1.06	2.98												
Henriques	1.43	1.80	1.50	1.51											
CEM (2 min.)	4.57	1.88	4.84	1.87	3.34										
CEM (10 min.)	3.56	1.23	3.81	0.88	2.32	1.07									
CEM (60 min)	2.57	1.04	2.79	0.24	1.32	2.06	1.06								
CEM (240 min.)	2.02	1.30	2.18	0.84	0.75	2.65	1.64	0.66							
Jacques	0.95	3.38	0.29	3.19	1.70	5.04	4.01	3.00	2.39						
Borelli	2.85	1.05	3.07	0.12	1.59	1.79	0.79	0.33	0.93	3.27					
Brown	2.43	1.08	2.64	0.38	1.19	2.20	1.20	0.18	0.51	2.85	0.48				
Viability 10%	1.95	1.36	2.10	0.93	0.66	2.75	1.73	0.75	0.13	2.31	1.02	0.61			
Viability 50%	2.11	1.25	2.28	0.76	0.83	2.58	1.56	0.58	0.13	2.48	0.85	0.43	0.22		
Viability 90%	1.63	1.61	1.73	1.29	0.27	3.13	2.11	1.11	0.53	1.94	1.38	0.97	0.43	0.61	

Table 16: MDA Values for the segmentations and models in Chapter 6

Vita

Christopher James MacLellan was born in Boston, Massachusetts on July 15th, 1988, the son of Stephen and Barbara MacLellan. After completing his work at Medfield High School in 2006, he entered the University of Massachusetts Amherst. He received the degree of Bachelor of Science, *summa cum laude*, with a major in Physics from UMass in May, 2010. In August 2010 he entered The University of Texas Graduate School of Biomedical Sciences at Houston.

Permanent address:

7500 Kirby Drive, Apt. 1431

Houston Texas, 77030